ISSN (print) 0023-2912
ISSN (online) 3034-543X

Российская Академия Наук

Volume 87, No. 1 January - February 2025

КОЛЛОИДНЫЙ ЖУРНАЛ
COLLOID JOURNAL

NAUKA
1727

Russian Academy of Sciences

КОЛЛОИДНЫЙ ЖУРНАЛ / COLLOID JOURNAL

Journal of Physical Chemistry of Surface Phenomena and Disperse Systems

Volume 87 No. 1 2025 January - February

Founded in 1935.
Published bimonthly.
ISSN (print) 0023-2912
ISSN (online) 3034-543X

The journal publication is guided by the Department of Chemistry and Material Sciences, RAS

Editorial office: Moscow, 119071, Leninsky pr., 31,korp. 4, Office No. 145;
tel.: +7(495) 955-46-25;
e-mail: colljour@mail.ru

Moscow
«Nauka» Publishers»

CONTENTS

Vol. 87, No. 1, 2025

COLLOID JOURNAL, 2025, Vol. 87, No. 1, pp. 3–14

EFFECT OF CONDITIONS FOR OBTAINING DETONATION NANODIAMOND ON SURFACE COMPOSITION AND STABILITY OF ITS AQUEOUS SOLS[1]

© 2025 A. V. Volkova*, D. A. Savelev, N. S. Chuikov, V. A. Vodolazhskii, and L. E. Ermakova

Saint Petersburg State University, Saint Petersburg, Russia

**e-mail: anna.volkova@spbu.ru*

Received November 15, 2024
Revised December 08, 2024
Accepted December 19, 2024

Abstract. In present work, the effect of additional treatment of detonation nanodiamond (DND) powder of basic purification on the surface composition of DND particles, their electrokinetic properties, as well as aggregate stability in solutions of indifferent electrolyte (NaCl) in a wide pH range was studied. It has been found that a higher degree of purification of the samples and an increase in the number of protonated carboxyl groups on the surface of the DND particles due to additional acid and thermoammonia treatment leads to a shift in the position of the isoelectric point (IEP) from pH 7.0 for the initial sample to pH 6.3 and pH 6.0, respectively. It is shown that the coagulation thresholds of hydrosols at natural pH and the position of stability zones in 10^{-3} M sodium chloride solution are in full compliance with the IEP values. The highest thresholds are observed at pH 5.8 for the initial DND, while for the dispersion of DND particles after thermoammonia treatment, fast coagulation occurs already at a concentration of 10^{-4} M. It is also shown that the aggregate stability zones for additionally treated DND samples almost coincide. In the case of DND of basic purification, the stability zone expands in the area of positive zeta-potential, and in the area of negative values stability is not observed, probably due to the partial dissolution of surface impurities at high pH and their transition in ionic form to the solution, which causes coagulation of DND particles.

Keywords: *detonation nanodiamond, surface modification, surface functional groups, aggregate stability, coagulation threshold, zeta-potential, isoelectric point*

DOI: 10.31857/S00232912250101e6

INTRODUCTION

Detonation nanodiamonds, due to such classical properties of diamond as hardness and chemical inertness, are widely used as materials for finishing polishing, in electroplating, and in oil compositions [1, 2]. It is possible to use DND as sorbents with ion exchange properties [3–5]. In recent years, DND nanoparticles have attracted increasing interest due to the prospect of their use in biomedical applications [6–9]. The possibility of effective practical application of both dilute and concentrated dispersions of DND is largely determined by their electrosurface properties, as well as sedimentation and aggregation stability, which depend on the surface composition and, consequently, on the conditions of detonation nanodiamond production. In this case, sedimentation stability in concentrated dispersions (for example, when obtaining polishing compositions) can be achieved due to the formation of periodic colloidal structures, i.e., due to the loss of aggregative stability by the system [10]. The position of the zero charge point and isoelectric point, and, consequently, the sorption properties and values of the electrokinetic potential of DND particles, other things being equal, can be influenced by refining DND base powders from both surface impurities, including water-soluble metal-containing impurities [11, 12], and non-diamond forms of carbon. Unification of the detonation nanodiamond surface, often leading to disaggregation of powders due to the removal of at least most of the sp^2-carbon, is performed by chemical and/or thermal treatment of DND both basic and deep purification: most often by

---

[1] Supplementary materials can be found at the DOI page of the article: https://doi.org/10.31857/S00232912250101e6

oxidation or reduction in the liquid or gas phase (air, ozone, argon, hydrogen) [13–20]

In addition, aqueous DND sols can serve as a model system for studying the electrokinetic characteristics and the structure of the boundary layer depending on the functional composition of the surface in contact with the electrolyte solution, as well as the regularities of aggregation in nanodisperse systems [21] containing both nanoparticles and primary aggregates. Such fundamental studies are important both for the improvement of theoretical ideas about the structure of the electrical double layer at the solid-solution interface and for the development of existing theories of the stability of real dispersions. It should be noted that most of the works devoted to the study of electrokinetic properties and stability of DND sols consider systems in which the sign of the surface charge of DND particles does not change practically in the whole pH region [22–28]. In turn, the IEP position in the neutral pH region (as in the case of DND powders studied in the present work) makes it possible to study the coagulation behavior of sols depending on their colloidal-chemical properties, both in the positive and negative surface charge region. From the point of view of applied problems such DND powders depending on pH can be used, for example, as sorbents for the extraction of both cationic and anionic impurities from the liquid phase, to form various kinds of coagulation structures in concentrated dispersions.

In connection with the above, the aim of the present work was to investigate the aggregative stability of aqueous sols of industrial DND powders (basic and additional acid and thermoammonia purification) in a wide range of concentrations and pH of sodium chloride solutions, as well as to establish the relationship between the conditions of their production, composition of the surface, electrokinetic properties and the position of stability and coagulation zones of detonation nanodiamond hydrosols.

EXPERIMENTAL PART

As an object of study we used industrial detonation nanodiamond powder produced by FSUE SCTB “Technolog” (St. Petersburg, Russia), obtained by detonation of TNT–hexogen mixture in the ratio 60/40 and separated from the diamond-containing charge by thermoxidation with aqueous ammonium nitrate solution with nitric acid additives according to the method presented in the patent RU2599665C2. The sample is labeled in the article as DND. To establish the relationship between the conditions of purification and unification of the surface of DND powders and the aggregative stability of dispersions obtained from them, SCTB “Technolog” also provided samples of detonation diamond obtained from the initial DND of basic purification (“raw material”) by additional thermoammonia treatment (DND-TA) and treatment with a mixture of nitric (56%) and hydrofluoric (40%) acids (DND-A) at room temperature.

To remove possible ionic impurities remaining after chemical treatment of DND powders, all provided samples were purified three times by electrodialysis. The purification cycle is described in detail in [29].

The specific surface area values S_{sp} of the powders were determined by BET method by thermal desorption of nitrogen with chromatographic registration. The average size of primary nanoparticles d_o was calculated by the formula:

$$d_o = 6/\rho S_{sp}, \tag{1}$$

where $\rho = 3.52$ g/cm^3 is the density of DND.

The phase composition of the powders was determined at the Resource Center (RC) for X-ray Diffraction Studies using a Bruker “D2 Phaser” desktop automatic powder diffractometer (Bruker AXS, Germany). Phase identification was carried out with the help of the PDXL 2.0 software package using the Powder Diffraction File database (PDF-2 Release 2020 RDB, PDF-2/Release 2011 RDB).

Elemental analysis of DND powders was performed by X-ray photoelectron spectroscopy (XPS) using a Thermo Fisher Scientific Escalab 250Xi integrated photoelectron and scanning Auger-electron spectrometer (Thermo Fisher Scientific, UK) in the Resource Center for Physical Methods of Surface Investigation of the SPSU Science Park and energy dispersive X-ray fluorescence spectroscopy on a Shimadzu EDX-800P spectrometer (Shimadzu, Japan) in the RC for Innovative Technologies of Composite Materials of the SPSU Science Park.

The surface composition of DND particles was also studied by Raman methods on a Senterra instrument (Bruker, Germany) in backscattering geometry and disturbed total internal reflection (DTIR) on a Nicolet 8700 FT-IR spectrometer (Thermo Scientific, USA) with a DTIR attachment (Smart iTR) with a diamond crystal at the Resource Center for Optical and Laser Materials Research of the SPSU Science Park. Raman excitation was performed using an external solid-state laser with a wavelength of 532 nm. Spectra were recorded in the range of 100–2,200 cm^{-1}. The IR absorption spectra after subtraction of the base line caused by scattering were given by the maximum value in the region of valence vibrations of OH-groups.

To study the electrokinetic properties and aggregative stability of aqueous dispersions of detonation nanodiamond as a function of the concentration of sodium chloride solutions (10^{-4}–10^{-1} M) at natural pH (5.8–6.0) and pH (4–11.5) in 10^{-3} M NaCl solution, dilute hydrosols of DND were prepared according to the method [29], which retained their dispersibility throughout the experiment. The particle sizes of the initial aqueous DND hydrosols are given in Table 1.

It should be noted that the obtained initial sols diluted twice with deionized water had similar values of optical density (0.19 ± 0.01 at a light wavelength of 380 nm) and partial concentration $(2–4)\times10^{10}$ particles/cm^3, determined by particle trajectory analysis on a NanoSight NS300 device (Malvern, UK).

Particle sizes of DND hydrosols were determined by scanning electron microscopy (SEM) using a Carl Zeiss Merlin scanning electron microscope (Carl Zeiss Merlin, Germany) in the Interdisciplinary Resource Center for Nanotechnology at the SPSU Science Park and by dynamic light scattering (DLS) on a Zetasizer Nano ZS analyzer (Malvern Instruments, UK) in a universal capillary U-shaped cuvette (DTS1070) with integrated gold-plated electrodes with pre-tempering for 2 min at 20°C.

To study the coagulation process of DND sols, turbidimetry methods were used (the detailed experimental procedure is described in [29]) using a photoelectrocalorimeter KFK-3-01 (optical path 50 mm, light wavelength 380 nm) and dynamic light scattering. Measurements of optical density were carried out within 15 minutes from the moment of electrolyte addition to the ash, particle size after 20 minutes after system creation.

The electrophoretic mobility (U_e) of DND particles was determined by laser Doppler electrophoresis on a Zetasizer Nano ZS analyzer (Malvern Instruments, UK) in parallel with the measurement of particle size distributions under similar conditions. The values of electrokinetic potential (ζ^S) in the first approximation were calculated by the Smoluchowski equation:

$$\zeta^S = \frac{\eta}{\varepsilon\varepsilon_0} U_e \, . \qquad (2)$$

Deionized water with specific conductivity not exceeding 1.5×10^{-6} Ohm^{-1}cm^{-1} (Aqualab AL Plus water purification system) was used to prepare solutions and dispersions. The required pH values were set using 3×10^{-2} M and 10^{-1} M solutions of hydrochloric acid and sodium hydroxide. pH of the medium was measured using a SevenMulti pH meter (Mettler Toledo).

RESULTS AND DISCUSSION

Phase composition and surface composition of DND particles.

Fig. 1 shows the results of X-ray phase analysis (XRD) of the investigated DND powders. It can be seen that in addition to the main phase of diamond on the XRD there are also weak peaks of impurity phases, which most likely belong to the phases of zinc sulfide and titanium dioxide in the modification of rutile. It can also be seen that according to the intensity of these peaks, the content of impurity phases is maximum in the initial sample of DND, while phase ZnS and phase TiO_2 are practically undetectable in the DND-TA sample and in the powder DND-A, respectively. In this connection, it should be noted that each method of additional processing is somewhat selective with respect to surface impurities.

The results of energy-dispersive X-ray fluorescence analysis showed (Fig. 2) that additional treatment of the initial powder of detonation nanodiamond leads to an increase in the relative content of such elements as iron (especially in the case of DND-TA) and titanium due to the partial removal from the surface of DND particles, apparently, more acid- and alkali-soluble components: calcium, silicon, aluminum, etc. The higher total content of iron and titanium elements in the DND-TA sample compared to DND-A may indicate a more effective purification in the general case of thermoammonia treatment. At the same time, the observed lowest content of zinc and sulfur for the DND-TA sample is in good agreement with the XRD results.

Fig. 3 shows the FT-IR spectra of the investigated DND powders. It can be seen that for all three samples at 1,325 cm^{-1} nanodiamond peak corresponding to the valence vibration of the C–C bond in the DND crystal lattice is observed [30, 31]. It can also be seen that the main differences in the spectra of the samples are observed in the range 1,330–1,800 см$^{-1}$. Thus, the noticeable absorption at 1,350 cm^{-1} for the original sample, which is most likely due to symmetric vibrations of the deprotonated carboxyl group (COO$^-$) [17], is much less pronounced for DND-TA and is practically absent in the spectrum of the DND-A sample. The change in the ratio of intensities of the peak at 1,735 cm^{-1}, which characterizes the valence vibrations of the carbonyl group C=O as part of the protonated carboxyl group, and the peak at 1,555 cm^{-1}, which can be attributed to asymmetric valence C=O vibrations as part of the deprotonated COO$^-$ group, attracts attention.

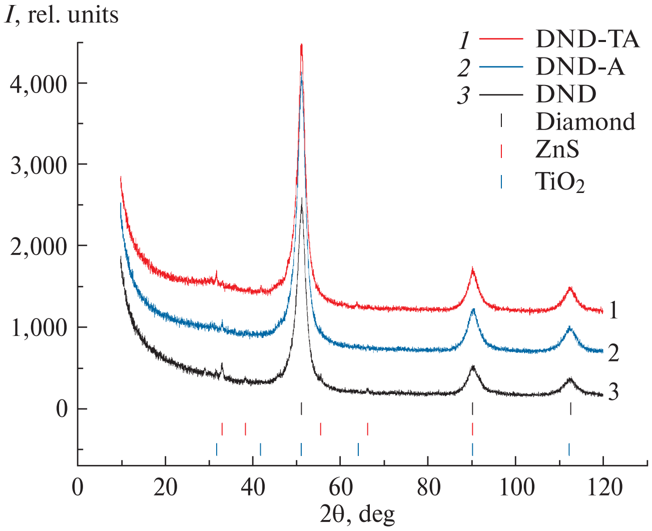

Fig. 1. X-ray radiographs of detonation nanodiamond powders.

Table 1. Structural characteristics of initial diluted aqueous DND sols.

Sample	DND	DND-A	DND-TA
SEM images	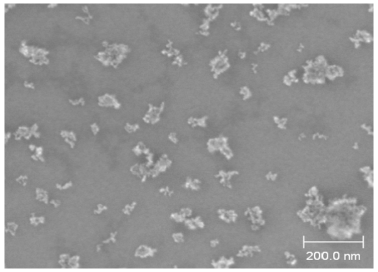	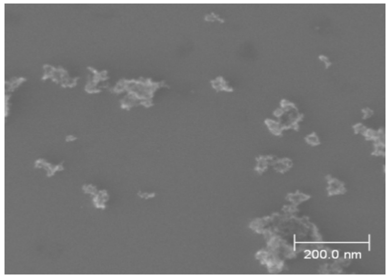	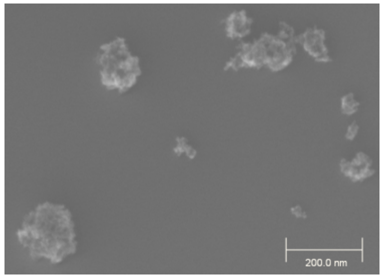
Specific surface area S_{sp}, m^2/g	305	295	290
Average size of primary nanoparticle d_o, nm (equation 1)	5.6	5.8	5.9
Average size (range of particle sizes) determined by DLS method $d_I / d_V / d_N$[1], nm	135 (45–400)/ 85 (40–340)/ 65 (40–190)	140 (45–340)/ 110 (40–400)/ 70 (40–255)	180 (80–400)/ 135 (70–400)/ 110 (70–300)

---

[1] d_I is the average particle size (diameter) from the size distribution of scattered light intensity
d_V and d_N are the average particle size (diameter) from the volume and particle number size distributions, respectively.

Probably due to the binding of some of the carboxyl groups to impurities, the number of deprotonated carboxyl groups on the surface of the base purification DND particles is greater than the protonated ones. Additional chemical treatment leading to the removal of part of these impurities from the surface leads to an increase in the number of protonated and a decrease in the number of deprotonated carboxylic groups, with the maximum COOH/COO$^-$ ratio observed for the DND-TA sample.

Another possible reason for the increase in the number of COOH groups for additionally treated samples is probably a decrease in the amount of sp^2-carbon on the surface of DND particles due to the oxidation of C=C bonds. Thus the absorption band 1,555 cm^{-1} may also correspond to a possible, but less intense than C=O valence vibrations in C=C bonds, the presence of which is also confirmed by the Raman spectroscopy results.

As can be seen from Fig. 4, in addition to the nanodiamond peak at 1,328 cm^{-1} [32] in the Raman spectra, there is a broad asymmetric peak with a maximum at 1,620 cm^{-1}, corresponding to carbon in sp^2-hybridization. Upon decomposition of this peak (on the example of DND-A, Fig. P1 of the Appendix), D- and G-lines of graphite are observed for all samples. It should be noted that the appearance of the graphite D-line in the Raman spectrum of DHA is associated in the literature with the formation of onion-like carbon shells around the diamond nucleus, on which the inclusions of graphite-like phase are located [33, 34]. The greater intensity of the graphite D-line in the spectrum of DND-TA compared to the original DND and DND-A (Fig. 4), apparently, characterizes the lower ordering and greater defectivity of the graphite-like phase in DND-TA. This probably indicates a more efficient removal of impurities contained in this phase from the surface of DND-TA particles, which confirms the results described above. It should also be noted that in the Raman spectra of all DND powders a peak at 1,735 cm^{-1} characterizing vibrations in the C=O bond is observed.

The X-ray photoelectron spectra of the C1s of DND powders are shown in Fig. 5. It can be seen that the C1s spectrum for the basic-cleaned DND powder is shifted to the region of higher binding energies compared to the additionally treated samples. The results of deconvolution of C1s peaks for DND and DND-A powders (similarly for DND-TA) (Fig. 6) showed that all samples are characterized by the presence of a peak with energy 287.7 ± 0.1 eV, corresponding to the C=O bond in the carbonyl [35, 36] or carboxyl group [14], and a peak 286.7 ± 0.1 eV corresponding to the C–O bond in hydroxyl and ether groups [14, 35–37] and probably to the C–N and C=N bonds according to [32, 38] and N1s spectra data (peak 399.3 eV, Fig. P2 of the Appendix). The peak at a binding energy of 403.1 eV probably characterizes the bonding of a nitrogen atom with three neighboring carbon atoms [32]. The least intense peak at a binding energy of 288.8 eV, appearing only in the spectrum of the initial DND (Fig. 6a), is often attributed to the carbon-oxygen bond in the COOH-group [39]. It can also be seen that, while the peak at 286.7 eV is the most intense for the original sample, for the DND-TA and DND-A samples (Fig. 6b) the main peak corresponds to a binding energy of 285.5 eV, corresponding to sp^3-hybridized carbon in the diamond crystal lattice, which is absent in the spectrum of the original sample. The observed changes in the C1s spectrum of the original sample after additional acid or thermoammonia treatment indicate a deeper purification of the samples from the non-diamond phase and, first of all, summarizing

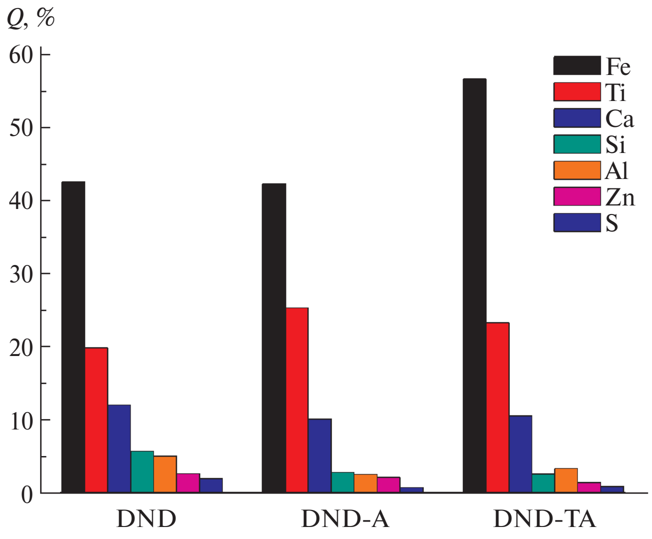

Fig. 2. Relative content of some elements on the surface of DND particles.

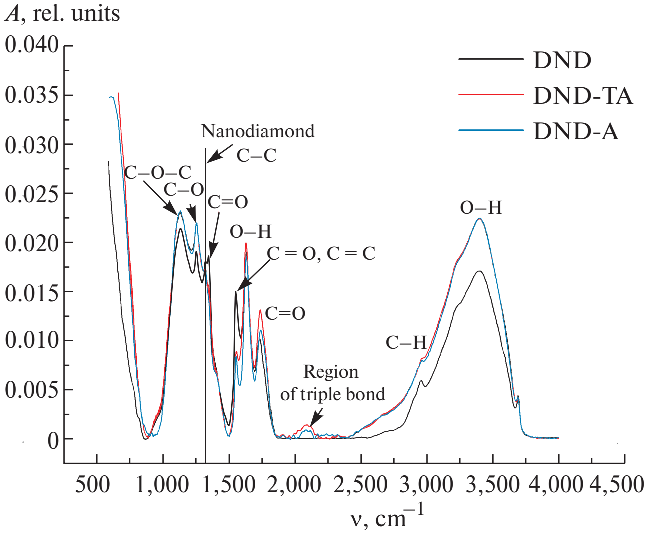

Fig. 3. Infrared absorption spectrum of DND powders with base line subtraction and fitting to the maximum in the valence vibration region of OH-groups.

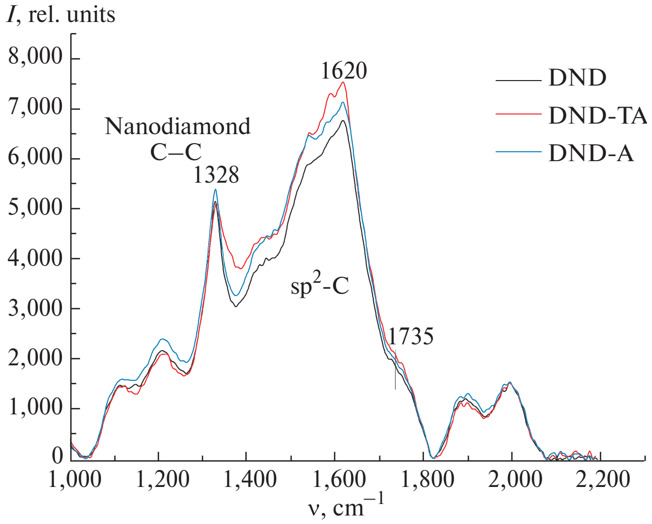

Fig. 4. Raman spectra of DND powders.

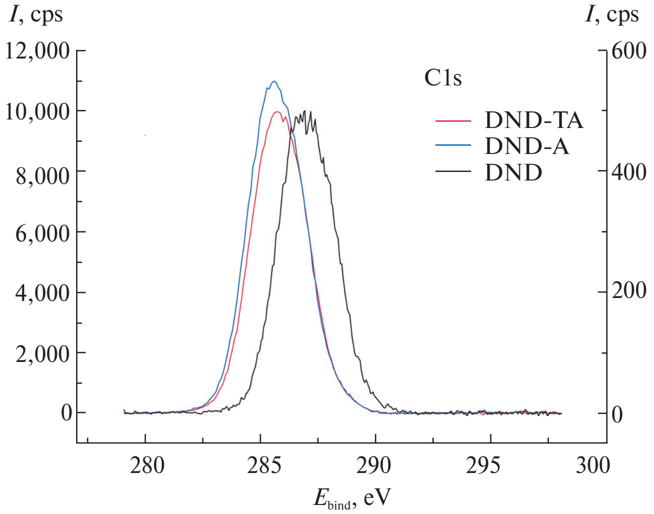

Fig. 5. X-ray photoelectron spectra of C1s of DND powders.

all the obtained results on the study of the surface composition, apparently from the bulk graphite-like phase.

From Fig. 7 shows that the O1s spectra for all the studied samples are quite close. When deconvolving the peaks of the O1s spectra (shown on the example of DND-A, Fig. P3 of the Appendix), at a binding energy of 533.1 ± 0.1 eV, the main peak corresponding to bonding between carbon and oxygen atoms in C–O–C and C–O–H groups is observed, as well as a peak of low intensity with a maximum of 530.8 ± 0.1 eV corresponding to the C=O bonding energy in the carbonyl or carboxyl group [35–37, 40].

It is known that surface charging of nanodiamond particles in liquid dispersion medium in the presence of ionogenic carboxyl and hydroxyl functional groups on their surface is described by the following surface reactions [23, 41]:

$$-\mathrm{COH_2}^+ \rightleftarrows -\mathrm{COH} + \mathrm{H_s}^+,$$

$$-\mathrm{COOH} \rightleftarrows -\mathrm{COO}^- + \mathrm{H_s}^+,$$

$$-\mathrm{COH} \rightleftarrows -\mathrm{CO}^- + \mathrm{H_s}^+.$$

Analysis of all obtained results showed that there is an obvious increasing contribution of carboxyl groups to the formation of surface charge of samples with additional acid or thermoammonia treatment in comparison with the initial sample of detonation nanodiamond.

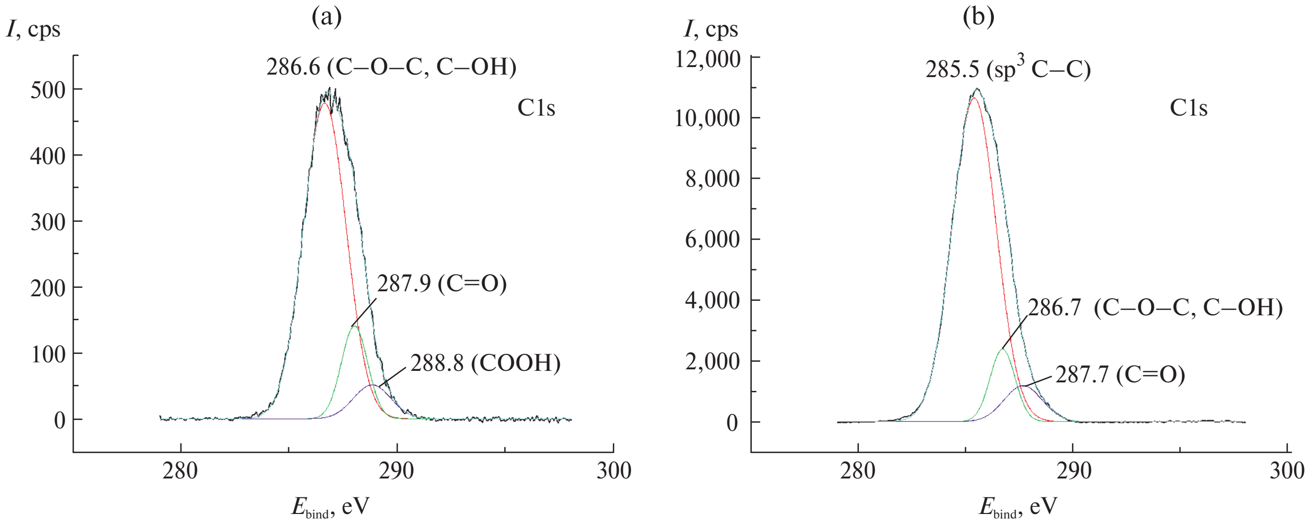

Fig. 6. X-ray photoelectron spectra of C1s of DND (a) and DND-A (b) powders.

Stability and electrokinetic properties of aqueous DND sols in NaCl solutions.

The study of electrokinetic properties and aggregative stability of aqueous sols of the provided DND powders was initiated in 10^{-3} M sodium chloride solution at different pH values. The results of the electrokinetic properties are summarized in Fig. 8 and Table 2. It can be seen that acid treatment of the initial DND powder leads to a shift of the IEP position from pH 7.0 to pH 6.3, and thermoammonia treatment – to pH 6.0, which is in good agreement with the results of the study of the surface composition of these samples: both with an increase in the number of surface carboxyl groups and a decrease in the content of impurities as a result of additional treatment. It can also be seen that the slope of the linear part of the dependences U_e (ζ^S) – log$C$ for DND and DND-TA samples coincides and is equal to about 16 mV/pH unit, and for DND-A is 34 mV/pH unit. It should be noted that at the same offset from IEP ($\Delta pH = pH - pH_{IEP}$) (Fig. P4 of the Appendix) in the region of positive values the values of electrokinetic potentials coincide within the error limits for all investigated DND samples, which is apparently due to the contribution of only hydroxyl functional groups to charge formation (Eq. 3). In the region of negative values, small differences are observed: so the minimum absolute values of zeta-potential correspond to the initial sample, while the maximum values correspond to DND-A. This is probably due to the different degree of influence of surface impurities on the electrokinetic properties of DND particles at pH change, which is mainly manifested in the alkaline pH region, and the different contribution of carboxyl groups to the formation of negative charge.

The results of studying the coagulation kinetics and determining the average particle size of DND sols on the background of 10^{-3} M NaCl solution as a function of pH are shown in Fig. 9, P5–P7 of the Appendix and Fig. 10, respectively. It can be seen that rapid coagulation of sols occurs in the region of the isoelectric point, as the distance from it towards higher and lower pH, a transition to the zones of slow coagulation accompanied by a decrease in optical density and average particle size is observed, and then to the regions of aggregative stability. It should be noted that in the region of slow coagulation at some pH a bimodal particle size distribution was observed (the value of average peak sizes in Fig. 10 are connected by a dashed line). As can be seen from Figs. 9 and 10, for aqueous DND-TA and DND-A sols, the zones of aggregative stability practically coincide (hydrosols are stable at pH $\leqslant$ 4.9 and at pH $\geqslant$ 8.4 – regions of positive and negative values of electrokinetic potential, respectively), which is apparently due to the close position of isoelectric points. The shift of the IEP to pH 7.0 for the baseline purification DND causes an extension of the stability zone in the region of positive zeta potential values up to pH 5.8. It should be noted that for the initial DND, in contrast to the samples subjected to additional treatment, no stability in the region of negative values of ζ-potential is observed. Apparently, at high pH values, partial dissolution of surface impurities, which are removed in the case of DND-A and DND-TA during additional treatment, may occur, accompanied by the appearance of multi-charged cations in dispersion medium, which cause coagulation of DND particles. It can also be seen that in the region of negative values of zeta potential in the stability zone for DND-TA and DND-A, in some cases, optical density values are observed even lower

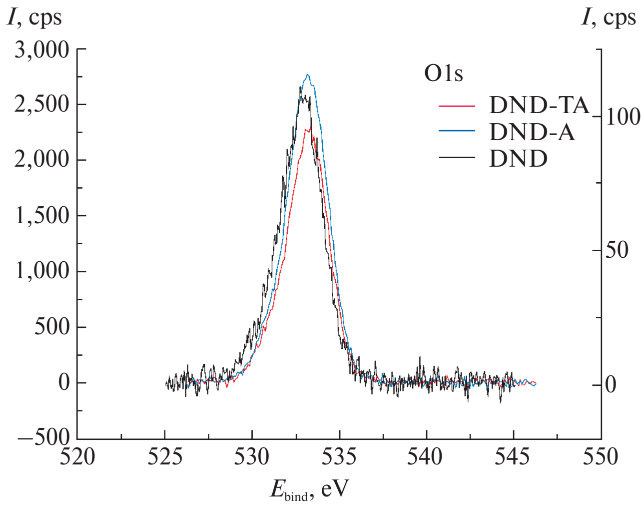

Fig. 7. X-ray photoelectron spectra of O1s of DND powders.

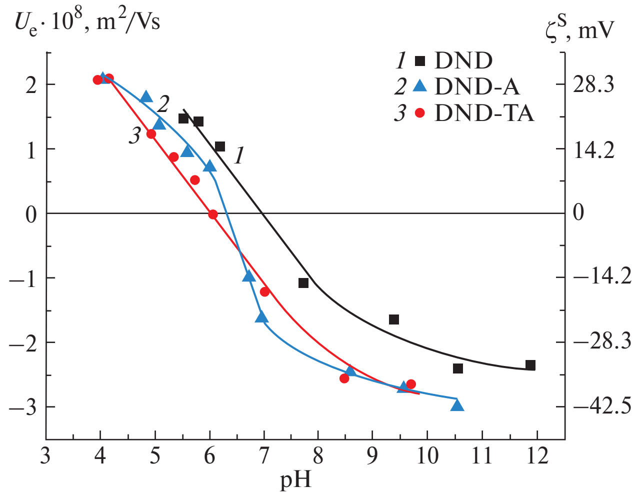

Fig. 8. Dependence of electrophoretic mobility (Ue) and electrokinetic potential (ζS) of hydrosol particles of different DND samples on the pH of 10^{-3} M sodium chloride solution.

Table 2. IEP pH values of DND samples and thresholds of fast and slow coagulation of their hydrosols in NaCl solutions at natural pH value

Sample	pH_{IEP} (10^{-3} M NaCl)	Threshold of slow coagulation C_{SC}, M	Fast coagulation threshold C_{FC}, M
DND	7.0	2.5×10^{-3}	7.5×10^{-3}
DND-A	6.3	2.8×10^{-4}	1.5×10^{-3}
DND-TA	6.0	–	$\leqslant 10^{-4}$ M

than for the initial aqueous sol. This, apparently, can be related to the partial disintegration of primary aggregates and the increase in the fraction of smaller particles with increasing absolute values of surface charge and electrokinetic potential.

Due to the fact that most often manufacturers of DND are primarily interested in their stability in aqueous medium at natural pH, coagulation thresholds in sodium chloride solutions were determined for the sols of the studied DND. For this purpose, the coagulation kinetics of DND sols was studied (the results are shown in Figs. 11–13) and the average particle sizes of dispersions were determined (Fig. 14) at different concentrations of NaCl solutions and natural pH 5.8 ± 0.2. On the basis of the obtained kinetic data, concentration dependences of the optical density of sols at 0.5 and 15 minutes of observation were plotted, from which the values of the slow C_{SC} and fast C_{FC} thresholds were found graphically (according to the method described in [29]). An example of the determination of coagulation thresholds is shown in Fig. P8 of the Appendix. The values of threshold electrolyte concentrations thus found are summarized in Table 2. It can be seen that the values of the coagulation thresholds of the studied samples agree well with the results of particle size determination (Fig. 14) and are in good agreement with the provisions of their IEP. Thus, the highest values of zeta potential (Fig. 15) and, accordingly, the thresholds of both slow and fast coagulation are observed for the basic purification DND (Table 2), whereas for the dispersion of DND-TA particles, which are practically in isoelectric state at natural pH, the threshold of slow coagulation could not be determined, and fast coagulation occurs already at a concentration of 10^{-4} M. As can be seen, detonation diamond sols are characterized by a rather narrow zone of slow coagulation, possibly due to the relatively high Hamaker constant of DND particles; however, it is noteworthy that additional acid treatment leads to the expansion of the slow coagulation zone of the DND-A sample compared to the initial DND.

Thus, we would like to note that the approach often used to assess the prospects of using DND powders by their stability and zeta potential value in water with

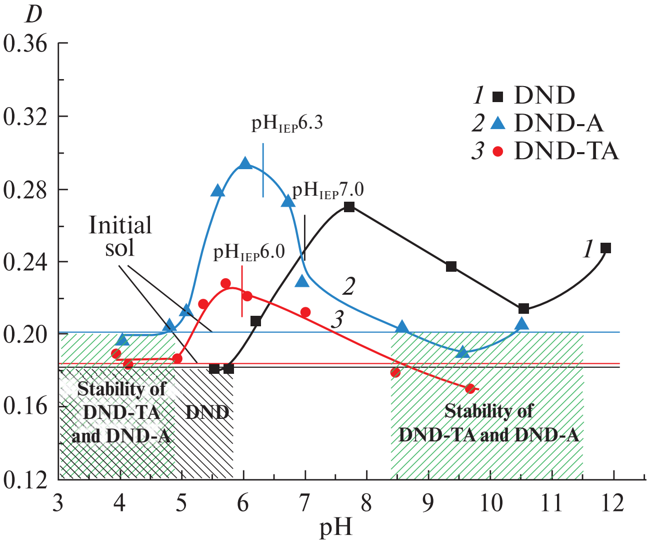

Fig. 9. Dependence of the optical density of aqueous detonation diamond sols on the pH of 10^{-3} M sodium chloride solution for 15 minutes of observation.

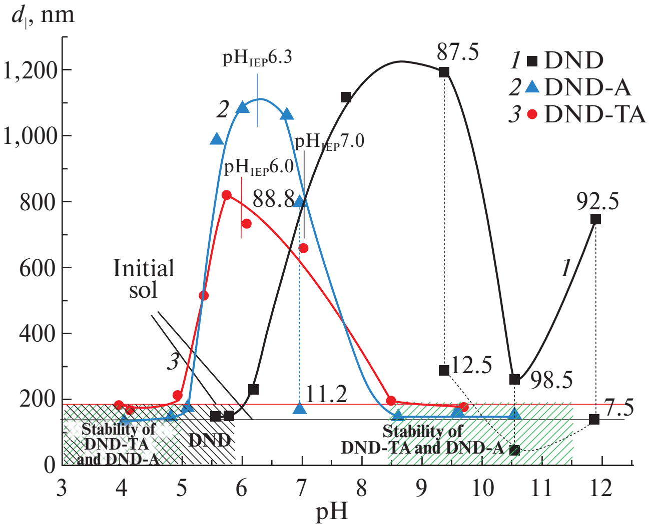

Fig. 10. Dependence of the mean DND particle size, determined from the scattered light intensity size distributions, on the pH of 10^{-3} M sodium chloride solution for 20 min of observation.

differences in the position of their IEP is incorrect, since, despite the lowest coagulation thresholds, the most promising for further use (e.g., obtaining carboxylated or hydrogenated DND on its basis) seems to be the DND-TA sample.

CONCLUSION

Analysis of the results of the study of the phase composition and surface composition of detonation diamond particles with different prehistory of production showed that additional acid and especially thermoammonia treatment of initial DND leads to a more complete purification of the surface of DND particles from the non-diamond phase. This leads to an increase in the number of surface protonated carboxyl groups due to both the removal of some impurities remaining in the graphite-like phase after primary treatment and the oxidation of C=C bonds of the sp^2-hybridized shell around the diamond core.

It was found that the main contribution to the formation of surface charge for all samples is made by surface dissociation-association reactions of hydroxyl groups, while the increase in the number of carboxyl groups for DND powders with additional treatment and different efficiency of acid and thermoammonia treatment to dissolve different types of surface

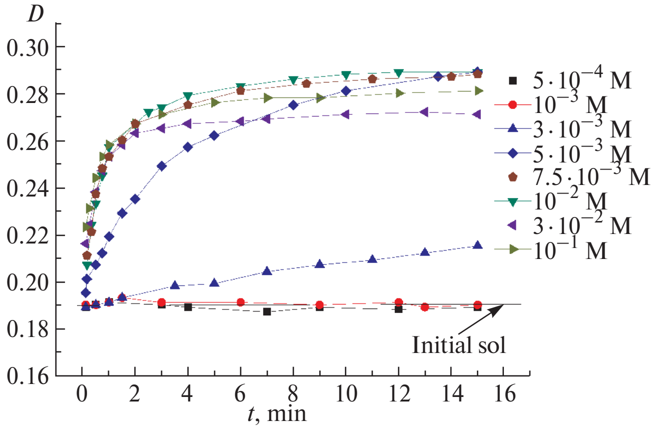

Fig. 11. Dependence of the optical density of DND hydrosol on the observation time at different concentrations of sodium chloride solutions and natural pH value.

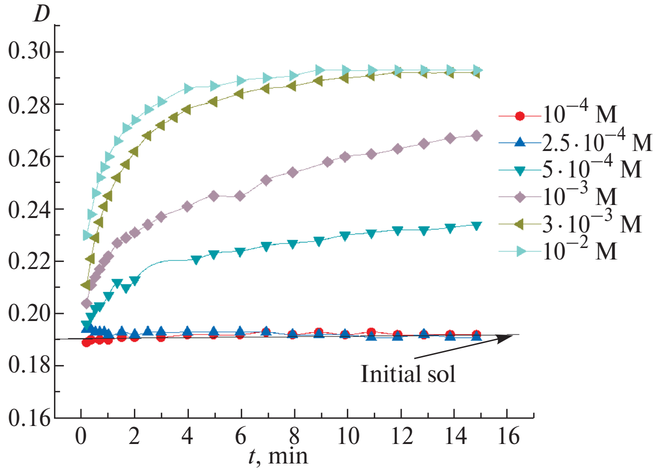

Fig. 12. Dependence of optical density of DND-A hydrosol on observation time at different concentrations of sodium chloride solutions and natural pH value.

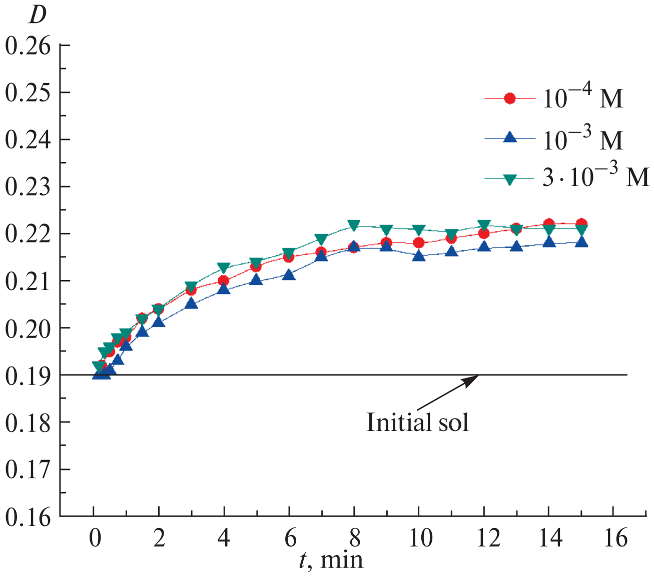

Fig. 13. Dependence of optical density of DND-TA hydrosol on observation time at different concentrations of sodium chloride solutions and natural pH value.

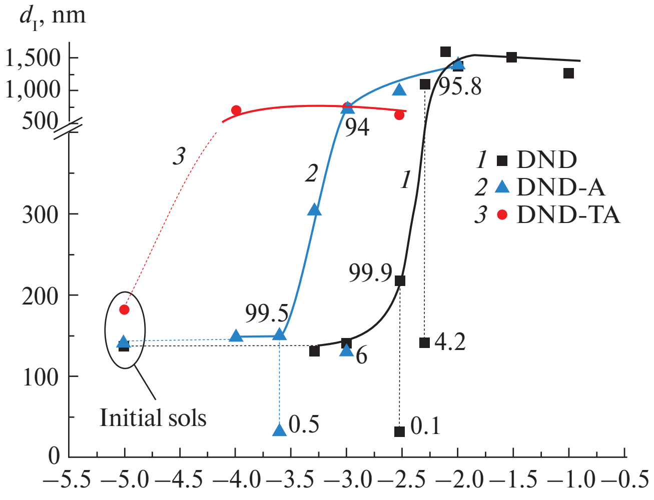

Fig. 14. Dependence of the average particle size d_1 on the concentration of NaCl solutions at natural pH value. Numerical values at dots are the fraction (%) of light intensity scattered by particles of a given size (given for the case of bimodal distribution).

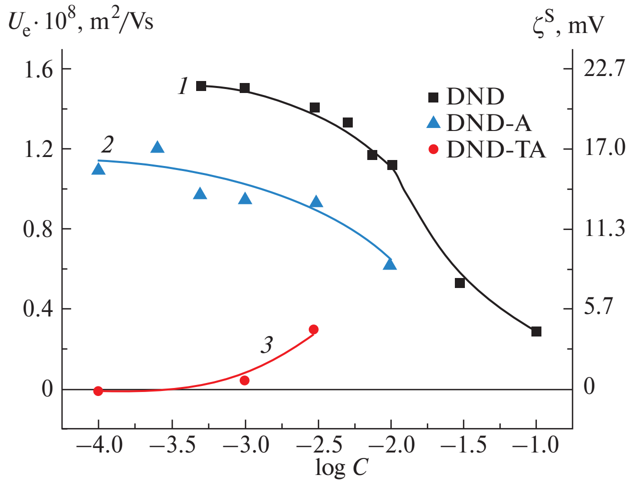

Fig. 15. Dependence of electrophoretic mobility (U_e) and electrokinetic potential (ζ^S) of hydrosol particles of different DND samples on the concentration of sodium chloride solutions at natural pH value.

impurities leads to differences in the electrokinetic properties and aggregative stability of the studied samples especially in the region of negative values of zeta potential.

It was found that acid treatment of basic purification of DND powder leads to a shift in the position of the isoelectric point from pH 7.0 to pH 6.3, and thermoammonia treatment – to pH 6.0 on the background of 10^{-3} sodium chloride solution. The zones of aggregative stability of DND sols were determined: hydrosols of detonation nanodiamond with additional treatment are stable in the region of positive values of electrokinetic potential at pH $\leqslant$ 4.9 and at pH $\geqslant$ 8.4 – in the region of negative ones according to the change of their electrokinetic properties. Aqueous sol of positively charged DND is stable at pH $\leqslant$ 5.8, in the whole investigated region of negative values of ζ-potential the sol coagulates, probably, due to dissolution of part of surface impurities at high pH values and their transfer in ionic form into solution.

The thresholds of slow and fast coagulation in NaCl solutions at natural pH were determined and compared for the studied DND hydrosols. It is shown that the values of coagulation thresholds of the studied samples are in full compliance with the provisions of their IEP.

FUNDING

The work was financially supported by the RSF grant No. 23-23-00333.

ETHICS DECLARATION

There are no human or animal studies in this paper.

CONFLICT OF INTERESTS

The authors declare that they have no conflict of interests.

ACKNOWLEDGEMENTS

The authors would like to thank D.A. Alexandrov for specific surface measurements. The research was carried out using the equipment of the Interdisciplinary Resource Centre for Nanotechnology, the Centre for Optical and Laser Materials Research, the Centre for Physical Methods of Surface Investigation, the Centre for X-ray Diffraction Studies, and the Centre for Innovative Technologies of Composite Materials at the Research Park of St. Petersburg State University.

REFERENCES

1. *Dolmatov V.Yu.* Ultrafine detonation synthesis diamonds: properties and applications // Uspekhi himii. 2001. Vol. 70. No. 7. Pp. 686–708. https://doi.org/10.1070/RC2001v070n07ABEH000665
2. *Dolmatov V.Yu.* Detonation nanodiamonds in oils and lubricants // Sverkhtverdye materialy. 2010. Vol. 32. No. 1. Pp. 19–28.
3. *Volkov D.S., Krivoshein P.K., Mikheev I.V., Proskurnin M.A.* Pristine detonation nanodiamonds as regenerable adsorbents for metal cations // Diamond and Related Materials. 2020. Vol. 110. P. 108121. https://doi.org/10.1016/j.diamond.2020.108121
4. *Peristyy A., Paull B., Nesterenko P.N.* Ion-exchange properties of microdispersed sintered detonation nanodiamond // Adsorption. 2016. Vol. 22. Pp. 371–383. https://doi.org/10.1007/s10450-016-9786-9
5. *Aleksenskii A.A., Chizhikova A.S., Kuular V.I. et al.* Basic properties of hydrogenated detonation nanodiamonds // Diamond and Related Materials. 2024. Vol. 142. P. 110733. https://doi.org/10.1016/j.diamond.2023.110733
6. *Turcheniuk K., Mochalin V.N.* Biomedical applications of nanodiamond // Nanotechnology. 2017. Vol. 28. Pp. 252001–252027. https://doi.org/10.1088/1361-6528/aa6ae4
7. *Schrand A.M., Ciftan Hens S.A., Shenderova O.A.* Nanodiamond particles: Properties and perspectives for bioapplications // Critical Reviews in Solid State and Materials Sciences. 2009. Vol. 34. Nos. 1–2. Pp. 18–74. https://doi.org/10.1080/10408430902831987
8. *Rosenholm J.M., Vlasov I.I., Burikov S.A. et al.* Nanodiamond-based composite structures for biomedical imaging and drug delivery // Journal of Nanoscience and Nanotechnology. 2015. Vol. 15. No. 2. Pp. 959–971. https://doi.org/10.1166/jnn.2015.9742
9. *Xu J., Chow E.* Biomedical applications of nanodiamonds: From drug-delivery to diagnostics // SLAS Technology. 2023. Vol. 28. No. 4. Pp. 214–222. https://doi.org/10.1016/j.slast.2023.03.007

10. *Chiganova G.A., Gosudareva E.Yu.* Structure formation in aqueous dispersions of detonation nanodiamonds // Rossiiskie nanotekhnologii. 2016. Vol. 11. Nos. 7–8. Pp. 25–29.
11. *Solovieva K.N., Belyaev V.N., Petrov E.A.* Investigation of the properties of detonation nanodiamonds depending on the technology of deep purification // Yuzhno-Sibirskii nauchnyi vestnik. 2020. Vol. 21. No. 3. Pp. 62–67. https://doi.org/10.25699/SSSB.2020.21.3.010
12. *Solovieva K.N., Belyaev V.N., Petrov E.A.* Fundamentals of the technology of finishing purification of detonation nanodiamonds // Vestnik tekhnologicheskogo universiteta. 2019. Vol. 22. No. 12. Pp. 85–87.
13. *Shenderova O., Petrov I., Walsh J. et al.* Modification of detonation nanodiamonds by heat treatment in air // Diamond & Related Materials. 2006. Vol. 15. Pp. 1799–1803. https://doi.org/10.1016/j.diamond.2006.08.032
14. *Sharin P.P., Sivtseva A.V., Popov V.I.* Thermal oxidation in air of diamond nanopowders obtained by mechanical grinding and detonation synthesis // Izvestija vuzov. Poroshkovaya metallurgiya i funkcional'nye pokrytiya. 2022. No. 4. Pp. 67–83. https://doi.org/10.17073/1997-308X-2022-4-67-83
15. *Osswald S., Yushin G., Mochalin V. et al.* Control of sp^2/sp^3 carbon ratio and surface chemistry of nanodiamond powders by selective oxidation in air // Journal of the American Chemical Society. 2006. Vol. 128. Pp. 11635–11642.
16. *Kulakova I.I.* Modification of detonation nanodiamond: effect on its physico-chemical properties // Rossiyskiy khimicheskiy zhurnal. 2004. Vol. 48. No. 5. Pp. 97–106.
17. *Arnault J.C., Girard H.A.* Hydrogenated nanodiamonds: Synthesis and surface properties //Current Opinion in Solid State and Materials Science. 2017. Vol. 21. Pp. 10–16. https://doi.org/10.1016/j.cossms.2016.06.007
18. *Williams O.A., Hees J., Dieker C. et al.* Size-dependent reactivity of diamond nanoparticles // ACS Nano. 2010. Vol. 4. No. 8. Pp. 4824–4830. https://doi.org/10.1021/nn100748k
19. *Gines L., Sow M., Mandal S. et al.* Positive zeta potential of nanodiamonds // Nanoscale. 2017. Vol. 9. Pp. 12549–12555. https://doi.org/10.1039/C7NR03200E
20. *Terada D., Osawa E., So F. et al.* A simple and soft chemical deaggregation method producing single-digit detonation nanodiamonds // Nanoscale Adv. 2022. Vol. 4. Pp. 2268–2277. https://doi.org/10.1039/D1NA00556A
21. *Batsanov S.S., Dan'kin D.A., Gavrilkin S.M. et al.* Structural changes in colloid solutions of nanodiamond // New J. Chem. 2020. Vol. 44. Pp. 1640–1647. https://doi.org/10.1039/C9NJ05191K
22. *Petrova N., Zhukov A., Gareeva F. et al.* Interpretation of electrokinetic measurements of nanodiamond particles // Diamond and Related Materials. 2012. Vol. 30. Pp. 62–69. https://doi.org/10.1016/j.diamond.2012.10.004
23. *Gareeva F., Petrova N., Shenderova O., Zhukov A.* Electrokinetic properties of detonation nanodiamond aggregates inaqueous KCl solutions // Colloids and Surfaces A: Physicochem. Eng. Aspects. 2014. Vol. 440. Pp. 202–207. https://doi.org/10.1016/j.colsurfa.2012.08.055
24. *Zhukov A.N., Shvidchenko A.V., Yudina E.B.* Electrical surface properties of detonation nanodiamond hydrosols depending on the size of dispersed particles // Colloid Journal. 2020. Vol. 82. No. 4. Pp. 416–422. https://doi.org/10.31857/S0023291220040175
25. *Sychev D.Yu., Zhukov A.N., Golikova E.V., Sukhodolov N.G.* The effect of simple electrolytes on the coagulation of monodisperse negatively charged detonation nanodiamond hydrosols // Colloid Journal. 2017. Vol. 79. No. 6. Pp. 785–791. https://doi.org/10.7868/S0023291217060118
26. *Mchedlov-Petrossyan N.O., Kamneva N.N., Marynin A.I. et al.* Colloidal properties and behaviors of 3 nm primary particles of detonation nanodiamonds in aqueous media // Phys. Chem. Chem. Phys. 2015. Vol. 17. Pp. 16186–16203. https://doi.org/10.1039/C5CP01405K
27. *Mchedlov-Petrossyan N.O., Kamneva N.N., Kryshtal A.P. et al.* The properties of 3 nm-sized detonation diamond from the point of view of colloid science // Ukr. J. Phys. 2015. Vol. 60. Pp. 932–937. https://doi.org/10.15407/ujpe60.09.0932
28. *Mchedlov-Petrossyan N.O., Kriklya N.N., Kryshtal A.P. et al.* The interaction of the colloidal species in hydrosols of nanodiamond with inorganic and organic electrolytes // Journal of Molecular Liquids. 2019. Vol. 283. Pp. 849–859. https://doi.org/10.1016/j.molliq.2019.03.095
29. *Volkova A.V., Beloborodov A.A., Vodolazhskii V.A. et al.* Effect of pH and concentration of an indifferent electrolyte on the aggregative stability of an aqueous detonation diamond sol // Colloid Journal. 2024. Vol. 86. No. 2. Pp. 169–192. https://doi.org/10.31857/S0023291224020031
30. *Petit T., Puskar L.* FTIR spectroscopy of nanodiamonds: Methods and interpretation // Diamond & Related Materials. 2018. Vol. 89. Pp. 52–66. https://doi.org/10.1016/j.diamond.2018.08.005
31. *Shenderova O., Panich A.M., Moseenkov S. et al.* Hydroxylated detonation nanodiamond: FTIR, XPS, and NMR studies // Phys. Chem. C. 2011. Vol. 115. No. 39. Pp. 19005–19011. https://doi.org/10.1021/jp205389m
32. *Stehlik S., Mermoux M., Schummer B. et al.* Size effects on surface chemistry and Raman spectra of sub-5 nm oxidized high-pressure high-temperature and detonation nanodiamonds // J. Phys. Chem. C. 2021. Vol. 125. Pp. 5647–5669. https://doi.org/10.1021/acs.jpcc.0c09190

33. *Aleksenskiy A.E., Baidakova M.V., Vul` A.Ya., Siklitskiy V.* The structure of the diamond nanocluster // Fizika tverdogo tela. 1999. Vol. 41. No. 4. Pp. 740—743.

34. *Sharin P.P., Sivtseva A.V., Yakovleva S.P. et al.* Comparison of morphological and structural characteristics of nanopowder particles obtained by grinding natural diamond and detonation synthesis method // Izvestiya vuzov. Poroshkovaya metallurgiya i funktsional'nye pokrytiya. 2019. Vol. 4. Pp. 55–67. https://doi.org/10.17073/1997-308X-2019-4-55-67

35. *Frese N., Mitchell S.T., Bowers A. et al.* Diamond-like carbon nanofoam from low-temperature hydrothermal carbonization of a sucrose/naphthalene precursor solution // C Journal of Carbon Research. 2017. Vol. 3. No. 3. P. 23. https://doi.org/10.3390/c3030023

36. *Lim D.G., Kim K.H., Kang E. et al.* Comprehensive evaluation of carboxylated nanodiamond as a topical drug delivery system // International Journal of Nanomedicine. 2016. Vol. 11. Pp. 2381–2395. https://doi.org/10.2147/IJN.S104859

37. *Thomas A., Parvathy M.S., Jinesh K.B.* Synthesis of nanodiamonds using liquid-phase laser ablation of graphene and its application in resistive random access memory // Carbon Trends. 2021. Vol. 3. P. 100023. https://doi.org/10.1016/j.cartre.2020.100023

38. *Petit T., Arnault J.C., Girard H.A. et al.* Early stages of surface graphitization on nanodiamond probed by x-ray photoelectron spectroscopy // Physical Review B – Condensed Matter and Materials Physics. 2011. Vol. 84. No. 23. P. 233407. https://doi.org/10.1103/PhysRevB.84.233407

39. *Lan G., Qiu Y., Fan J. et al.* Defective graphene@ diamond hybrid nanocarbon material as an effective and stable metal-free catalyst for acetylene hydrochlorination // Chemical Communications. 2019. Vol. 55. Pp. 1430–1433. https://doi.org/10.1039/C8CC09361J

40. *Testolin A., Cattaneo S., Wang W. et al.* Cyclic voltammetry characterization of Au, Pd, and AuPd nanoparticles supported on different carbon nanofibers // Surfaces. 2019. Vol. 2. No. 1. Pp. 205–215. https://doi.org/10.3390/surfaces2010016

41. *Zhukov A.N., Gareeva F.R., Aleksenskiy A.E.* A comprehensive study of the electrical surface properties of detonation nanodiamond agglomerates in aqueous solutions of KSd // Colloid Journal. 2012. Vol. 74. No. 4. Pp. 483–491.

COLLOID JOURNAL, 2025, Vol. 87, No. 1, pp. 15–21

ELECTROCONVECTION NEAR TWO-LAYER COMPOSITE MICROPARTICLES

© 2025 G. S. Ganchenko[a], V. S. Shelistov[a, *], and E. A. Demekhin[a, b]

[a]Laboratory of Micro- and Nanoscale Electro- and Hydrodynamics,
Financial University under the Government of the Russian Federation, Moscow, Russia

[b]Laboratory of General Aerodynamics, Institute of Mechanics,
Lomonosov Moscow State University, Moscow, Russia

*e-mail: shelistov_v@mail.ru

Received August 06, 2024
Revised September 16, 2024
Accepted September 18, 2024

Abstract. This paper presents the results of a numerical simulation of an electrolyte solution behavior near a spherical dielectric microparticle covered with a homogeneous ion-selective shell under the influence of an external electric field. The particle is assumed to be stationary, and the electrolyte either stays still or is pumped externally with a constant velocity in absence of the electric field. The field, in turn, generates electroosmotic flow near the particle's surface. It is shown that concentration polarization can occur near the particle, whereas electrokinetic instability only occurs near particles with a sufficiently thick shell. When the particle's surface charge is opposite to the one of its shell, non-stationary regimes may be observed when the shell is thin enough.

Keywords: *electrophoresis, electroosmosis, composite particle, concentration polarization, instability, numerical simulation*

DOI: 10.31857/S00232912250102e9

INTRODUCTION

The study of electroosmosis near solid particles is inextricably linked to the study of electrophoresis [1]. The forces generated by electroosmotic motion act on the particle immersed in the electrolyte. By the beginning of the 21st century, the study of the motion of microparticles and fluids in microscales – microfluidics – has gained special interest. In particular, electrophoresis finds application in labs-on-chip for solving problems of medical diagnostics and chemical analysis [2].

One of the main characteristics of electrophoresis is the dependence of the velocity developed by a microparticle on the properties of the electric field: this dependence turns out to be different for different types of particles. Smoluchowski [1] studied the motion of dielectric particles and established the linear character of the dependence of their velocity on the field strength. Later Dukhin showed [3] that the considered dependence is more complicated, and in theoretical works of Yariv's group [4–6] a deviation from the linear dependence was predicted for strong fields and strongly charged particles. Experimental confirmation of this prediction was obtained by Tottori [7]. A review of modern concepts of dielectric particle electrophoresis can be found in Khair [8].

Electrophoresis of ion-selective particles in liquid electrolyte shows a much more complex behavior due to the presence of concentration polarization and electrokinetic processes of the second kind [9–14]. The electrophoresis rate maintains the linear dependence on the field strength as long as it is small [11], but as the strength increases, the dependence becomes more complicated [12], and in strong fields unsteady flow regimes with various types of instabilities arise [13, 14].

When studying the behavior of more complex particles, like biological ones, the assumption of particle homogeneity turns out to be inapplicable [15, 16]. One of the simplest ways to overcome this obstacle is to consider composite particles with a fixed internal structure. The model of "soft" particles [17, 18], having a homogeneous core impermeable to the electrolyte and a homogeneous shell permeable to salt ions, has been quite successful. At the same time, there is a noticeable lack of theoretical research in this direction, and the existing works usually use significant simplifications (in particular, linearization of motion equations). A semi-analytical approach based on the splicing of asymptotic expansions, actively used by Yariv's group for both electrophoresis [6] and related electrokinetics problems [19], should be separately

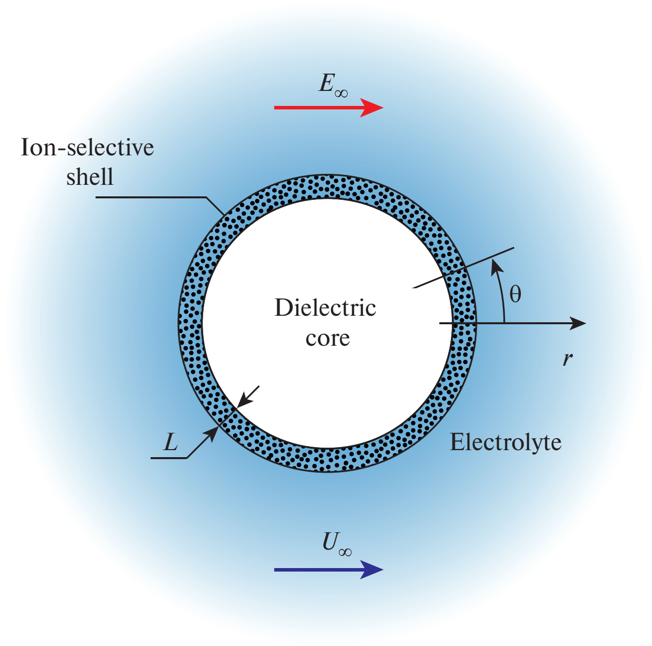

Fig. 1. Schematic representation of a composite microparticle.

emphasized. Nevertheless, the possibilities of analytical study of electrokinetics are approaching the limit, and further development requires the use of direct numerical simulation.

In the present work, we attempt to fill this gap and model the motion of a “soft” particle in a nonlinear statement with minimal simplifications. The results of numerical modeling can be used to predict the modes of motion arising in experiments and create a foundation for the development of labs-on-chip for manipulating complex biological particles.

PROBLEM STATEMENT AND SOLUTION METHODOLOGY

We consider a spherical microparticle consisting of a spherical electroneutral dielectric core of radius $\tilde{r}_0$ and a homogeneous uniformly charged shell made of an ion-selective layer of thickness $\tilde{L}$ (Fig. 1). The core’s surface is assumed to carry a uniform surface charge density $\tilde{\sigma}$, and the volumetric charge density of the shell is $\tilde{N}$. The particle is stationary and is bathed by a solution of electroneutral symmetric binary electrolyte with ion concentrations $\tilde{C}_\infty$, which is pumped at an external velocity $\tilde{U}_\infty$. To simplify the mathematical formulation, the value of $\tilde{C}_\infty$ is assumed to be sufficiently small, the charge numbers of the salt ions are assumed to be ±1, and their diffusion coefficients are assumed to be equal. These simplifications are valid, for example, for KCl solutions with concentration up to hundreds of mol/m^3, and allow us reducing the number of parameters of the problem. An external electric field of strength $\tilde{E}_\infty$ acts on the system. This formulation is similar to the one for electrophoresis [20], but $\tilde{U}_\infty$ acts as an additional parameter.

If we neglect chemical reactions and dissociation of the solvent liquid, the behavior of dilute electrolyte ions can be described by the system of Nernst–Planck equations, which should be complemented by the Poisson equation describing the electric potential distribution and the Navier–Stokes equations for the velocity field. Due to the smallness of characteristic Reynolds numbers, the Navier–Stokes equations are taken in the Stokes approximation:

$$\frac{\partial \tilde{C}^{\pm}}{\partial \tilde{t}} + \tilde{\mathbf{U}} \cdot \tilde{\nabla} \tilde{C}^{\pm} = \pm \frac{\tilde{D}\tilde{F}}{\tilde{R}\tilde{T}} \tilde{\nabla} \cdot \left(\tilde{C}^{\pm} \tilde{\nabla} \tilde{\Phi} \right) + \tilde{D} \tilde{\nabla}^2 \tilde{C}^{\pm}; \qquad (1)$$

$$\tilde{\varepsilon} \tilde{\nabla}^2 \tilde{\Phi} = -\tilde{F} \left(\tilde{C}^{+} - \tilde{C}^{-} \right); \qquad (2)$$

$$\tilde{\nabla} \tilde{\Pi} - \tilde{\mu} \tilde{\nabla}^2 \tilde{\mathbf{U}} = -\tilde{F} \left(\tilde{C}^{+} - \tilde{C}^{-} \right) \tilde{\nabla} \tilde{\Phi}; \qquad (3)$$

$$\tilde{\nabla} \cdot \tilde{\mathbf{U}} = 0. \qquad (4)$$

It is convenient to solve equations (1)–(4) in a spherical coordinate system with the origin at the center of the particle. Since the system has axial symmetry along the electric field direction, it is solved in axisymmetric formulation, so the spatial variables are the radius $\tilde{r}$ and azimuthal angle $0 \le \theta \le \pi$. The unknowns are the molar ion concentrations $\tilde{C}^{\pm}$, the electric potential $\tilde{\Phi}$, the pressure $\tilde{\Pi}$ and the velocity vector $\tilde{\mathbf{U}}$. The symbol $\tilde{F}$ denotes the Faraday constant, $\tilde{R}$ is the universal gas constant, and $\tilde{T}$ is the absolute temperature, which is assumed to be constant. The diffusion coefficient of electrolyte ions is denoted by $\tilde{D}$, the dynamic viscosity of the electrolyte is denoted by $\tilde{\mu}$, its absolute dielectric constant is denoted by $\tilde{\varepsilon}$. The last two quantities are assumed to be constant, independent of the local ion concentration. The dielectric constant of the core is denoted by $\tilde{\varepsilon}_{\mathrm{p}}$, and the dielectric constant of the shell, which is filled with electrolyte, is assumed to be $\tilde{\varepsilon}$. The ion diffusion coefficients in the shell are for simplicity assumed to be $\tilde{D}$ as well. The tilde in notations denotes dimensional quantities.

The following characteristic quantities have been chosen for making the system dimensionless: core radius $\tilde{r}_0$, diffusion coefficient $\tilde{D}$ (included in the characteristic time $\tilde{r}_0^2 / \tilde{D}$ and characteristic velocity $\tilde{D}/\tilde{r}_0$), thermal potential $\tilde{\Phi}_0 = \tilde{R}\tilde{T}/\tilde{F}$, concentration $\tilde{C}_\infty$, and viscosity $\tilde{\mu}$. Note that the choice of the diffusion velocity as the characteristic velocity simultaneously allows taking zero pumping velocity and does not introduce constraints into the hydrodynamics. Two dimensionless parameters appear in dimensionless equations (1)–(4): the Debye number $\nu = \tilde{\lambda}_{\mathrm{D}}/\tilde{r}_0$, where $\tilde{\lambda}_{\mathrm{D}}^2 = \tilde{\varepsilon}\tilde{R}\tilde{T}/\tilde{F}^2\tilde{C}_\infty$ is the square of the electric double layer thickness, and the coupling coefficient between the hydrodynamic and electrostatic parts of the problem $\kappa = \tilde{\varepsilon}\tilde{\Phi}_0^2/\tilde{\mu}\tilde{D}$. The equations eventually take the form

$$\frac{\partial C^{\pm}}{\partial t} + \mathbf{U} \cdot \nabla C^{\pm} = \pm\nabla \cdot \left(C^{\pm}\nabla\Phi\right) + \nabla^2 C^{\pm}; \tag{5}$$

$$\nu^2\nabla^2\Phi = C^- - C^+; \tag{6}$$

$$-\nabla\Pi + \nabla^2\mathbf{U} = \frac{\kappa}{\nu^2}\left(C^+ - C^-\right)\nabla\Phi; \tag{7}$$

$$\nabla \cdot \mathbf{U} = 0. \tag{8}$$

Equations (5)–(8) in this form are not applicable in all spatial areas. For example, no electrolyte penetrates into the core, so at $r < 1\, C^{\pm} = \mathbf{U} = 0$ and only equation (6) reduced to the Laplace equation remains of the whole system. For convenience in setting the boundary conditions, we denote the electric potential inside the core by ϕ:

$$\nabla^2\phi = 0. \tag{9}$$

Inside the shell, $1 < r < 1 + L,$ there is no electrolyte motion, $\mathbf{U} = 0$, and equations (5)–(6) take the form

$$\frac{\partial C^{\pm}}{\partial t} = \pm\nabla \cdot \left(C^{\pm}\nabla\Phi\right) + \nabla^2 C^{\pm}; \tag{10}$$

$$\nu^2\nabla^2\Phi = C^- - C^+ - N, \tag{11}$$

where $N = \tilde{N}/\tilde{C}_{\infty}$ is dimensionless volumetric charge density. This parameter determines the ability of the shell to attract ions of the same sign and repel ions of the opposite sign: at $N = -\infty$ the shell is perfectly cation-selective, at $N = +\infty$ – perfectly anion-selective. More details about its influence are given in [21] on the example of a flat membrane.

The considered formulation contains several boundaries, on each of which different conditions are imposed. All

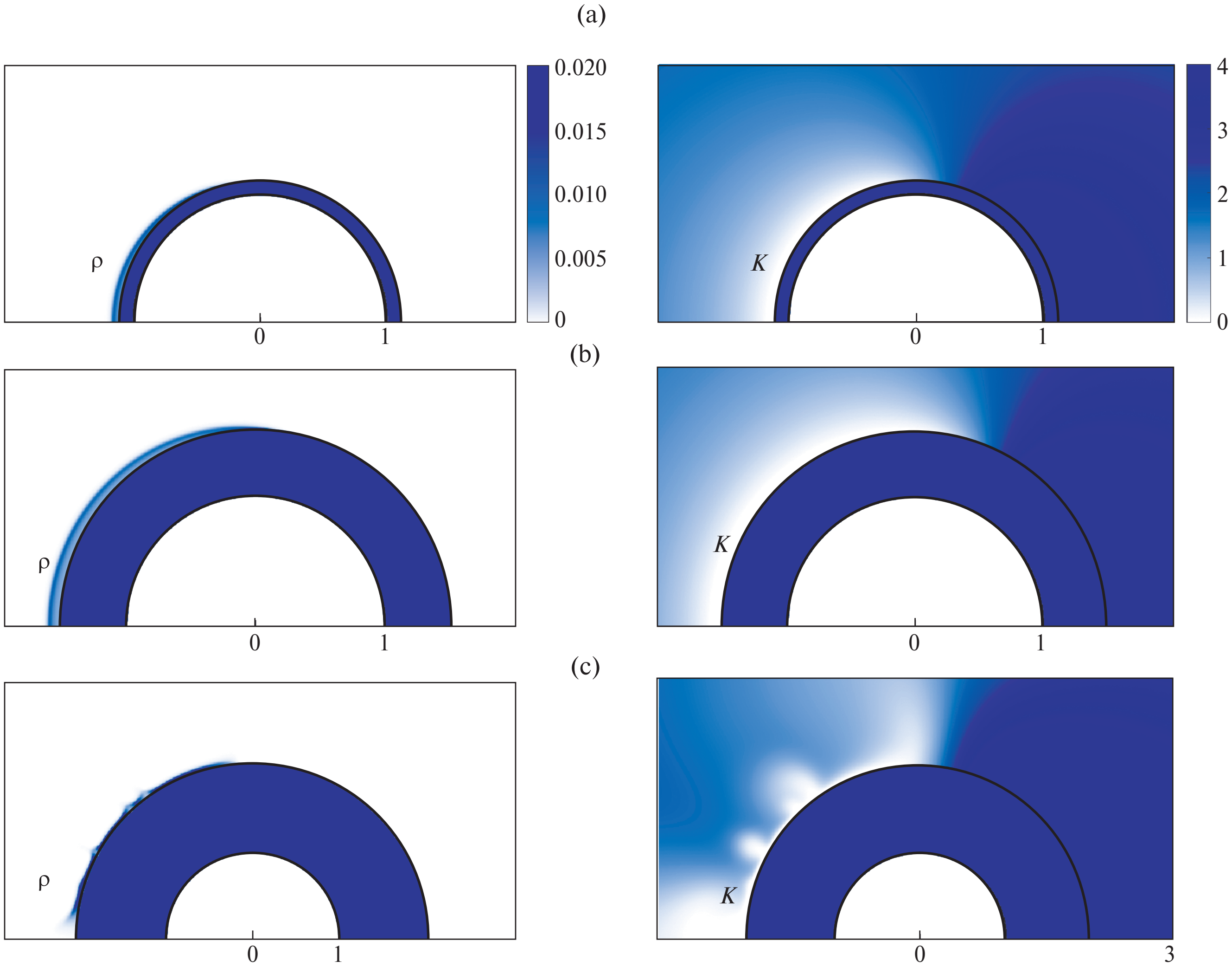

Fig. 2. Distributions of charge density $\rho = C^+ - C^-$ and salt concentration $K = C^+ + C^-$ outside the particle at $E_{\infty} = 10$, $U_{\infty} = 0$ and $\sigma = 0$. (a) $L = 0.1$, (b) $L = 0.5$, (c) $L = 1.0$. The distributions inside the shell are not shown.

unknown functions are assumed to be continuous in the whole domain. At the boundaries $\theta = 0$ and $\theta = \pi$, symmetry conditions are set for $C^{\pm}$, Φ and normal velocity components U_r, and antisymmetry condition for the tangential component $U_\theta = 0$. At $r = 0$, the zero level of potential, $\phi = 0$, is assumed and the condition of absence of singularity is imposed. At the boundary of the core, $r = 1$, one should expect a jump of the field strength by the value $\delta = \tilde{\varepsilon}_p/\tilde{\varepsilon}$ and the absence of ion flux:

$$r = 1: \ \Phi = \phi; \ \nu\frac{\partial \Phi}{\partial r} = \delta\nu\frac{\partial \phi}{\partial r} - \sigma; \qquad \pm C^{\pm}\frac{\partial \Phi}{\partial r} + \frac{\partial C^{\pm}}{\partial r} = 0. \tag{12}$$

On the boundary of the shell, $r = 1 + L$, simple no-slip and no-flux conditions, $\mathbf{U} = 0$, which ensure the continuity of the velocity field, are assumed. They can be considered as a special case of liquid slip conditions near a hydrophobic surface [22]. At a distance from the particle, the ion concentrations tend to the equilibrium value, the field strength tends to the one of the external field, and the velocity tends to the one of the incoming flow:

$$r \to \infty: C^{\pm} \to 1; \Phi \to -E_\infty r\cos\theta; \qquad U_r \to U_\infty \cos\theta; U_\theta \to U_\infty \sin\theta. \tag{13}$$

Finally, the electrolyte is assumed to be undisturbed at the initial time instant:

$$t = 0: C^{\pm} = 1. \tag{14}$$

This condition does not take into account the redistribution of ions due to the charge present in the particle, but calculations show that such redistribution occurs very quickly (within a few time steps) and does not affect the further behavior of the system.

To solve the system (5)–(14), we use a modification of the finite-difference method of the second-order approximation in space and the third-order approximation in time, previously used to solve the electrophoresis problem [20]. At each time step, the stationary equations (6)–(9) are transformed into systems of ordinary differential equations using the eigenfunction expansion of the differential operators with respect to the angle. The system for (9) is solved analytically and substituted into boundary conditions (12), the other equations are written in difference form and reduced to systems of linear algebraic equations with 3- and 5-diagonal matrices, which are solved by the tridiagonal matrix algorithm and its extension to 5-diagonal matrices. The found potential and velocity distributions are substituted into equations (5), which are integrated by the semi-implicit Runge–Kutta method [23].

In the calculations presented below, the following parameter values have been fixed: $\nu = 10^{-3}$, $\kappa = 0.2$, $N = -10$ (cation-selective shell with good selectivity), $\delta = 0.05$. The external electric field strength E_∞, the surface charge density of the core σ and the velocity of the incoming electrolyte U_∞ were varied, remaining constant within each of the calculations, with the direction of E_∞ and U_∞ following the scheme in Fig. 1.

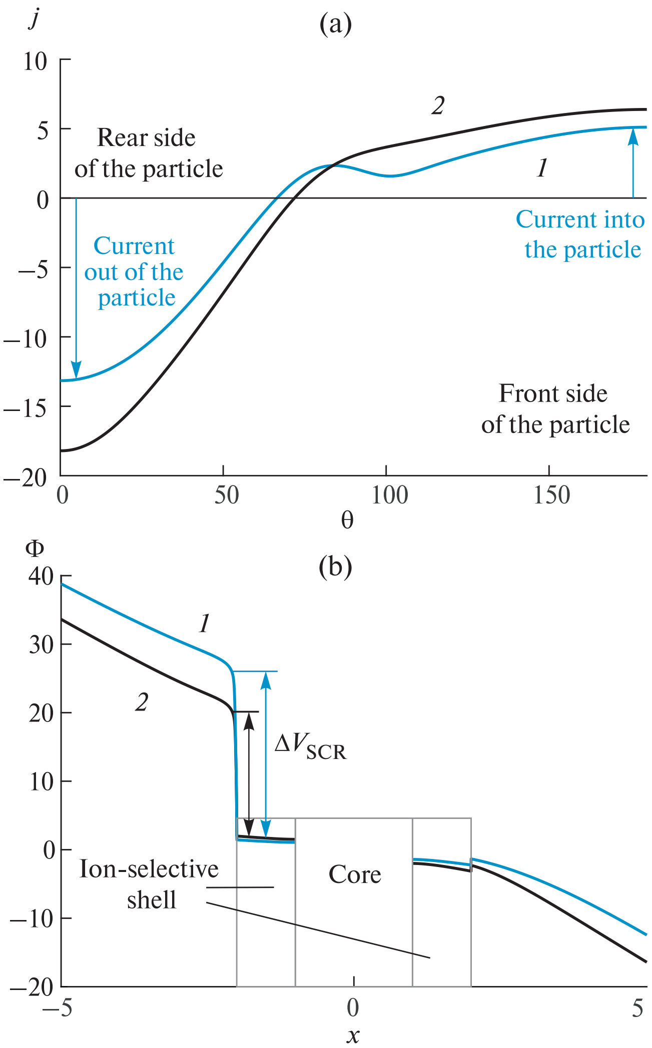

Fig. 3. Distributions of (a) current through the surface $j^{+}(\theta)$ and (b) electric potential Φ along the symmetry axis $x = r\cos\theta$ at $E_\infty = 5$, $\sigma = 0$ and $L = 1.0$. Curves *1*–$U_\infty = 0$, curves *2*–$U_\infty = 50$.

RESULTS AND DISCUSSION

When comparing electrophoresis of dielectric and ion-selective particles, the main difference is the presence of electric current through the particle surface. For the problem under consideration, it also seems logical to estimate the current through the shell boundary:

$$j^{+}(\theta) = \left(C^{+}\frac{\partial \Phi}{\partial r} + \frac{\partial C^{+}}{\partial r}\right)\bigg|_{r=1+L}.$$

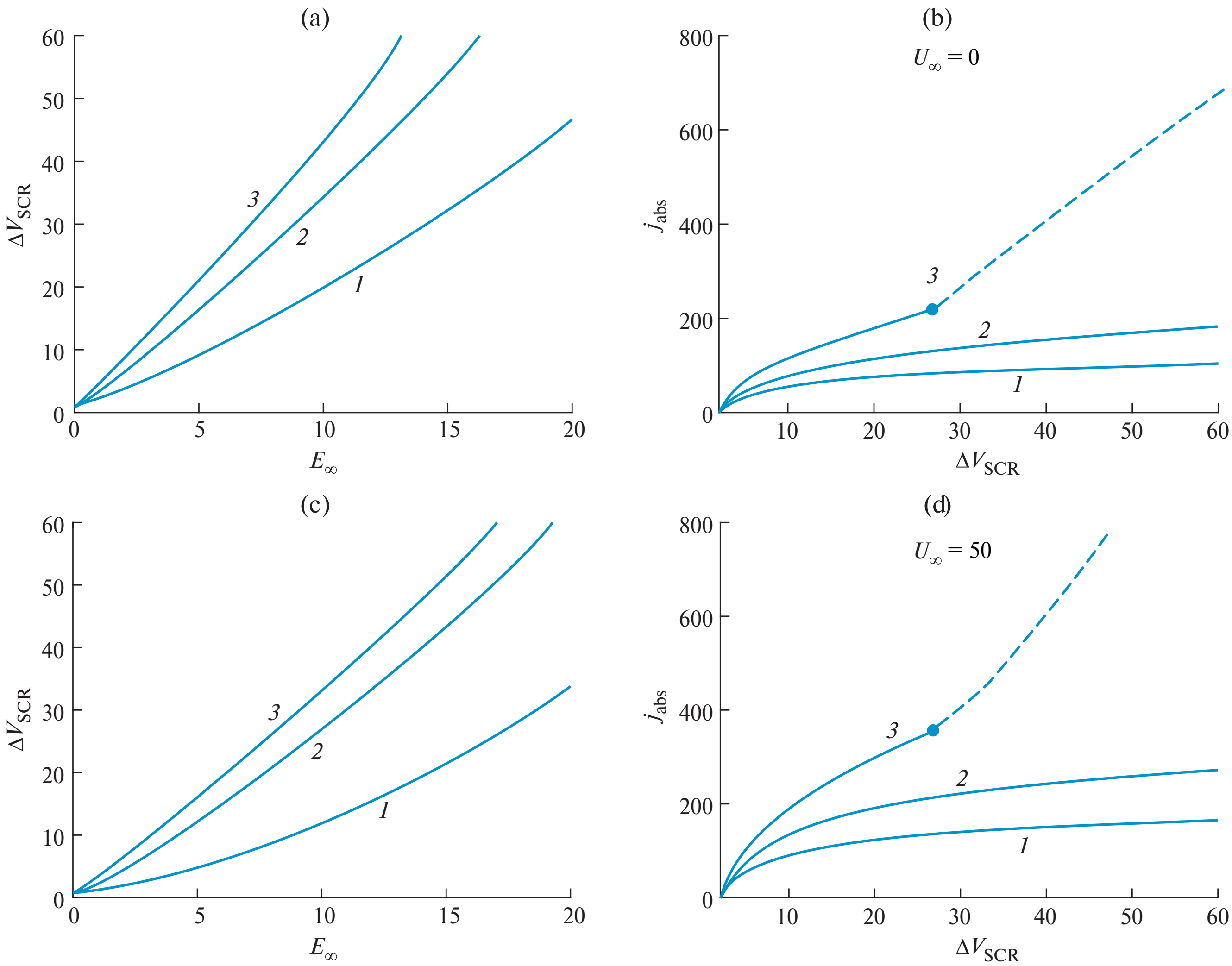

Fig. 4. (a), (c) – dependence of voltage drop in the space charge region ΔV_{SCR} on the external field strength E_∞; (b), (d) – dependence of integral current j_{abs} on ΔV_{SCR}. Graphs (a) and (b) are plotted without advection, $U_\infty = 0$, graphs (c) and (d) – with advection, $U_\infty = 50$. Curves *1* are $L = 0.1$, curves *2* are $L = 0.5$, curves *3* are $L = 1.0$. In all cases $\sigma = 0$. The dotted line corresponds to non-stationary modes (with electroconvection), for which the current values are averaged over time.

According to the scheme in Fig. 1, cations enter the shell from the left, $\theta > \pi/2$, and exit from the right, $\theta < \pi/2$. In stationary modes, the total charge of the shell remains unchanged, so the condition $\int_0^\pi j^+(\theta)\sin\theta d\theta = 0$ is satisfied. In the general case this condition can be violated (in particular, at $t = 0$).

Ion-selective surfaces are characterized by concentration polarization – redistribution of electrolyte ions near such a surface due to the influence of an external field with desalination and formation of a space charge area on the anode side, as well as with salt accumulation on the cathode side [11]. In sufficiently strong fields, the salt concentration can significantly exceed the equilibrium one [13]. Fig. 2 shows the charge and total ion concentration distributions in a still electrolyte near particles with different shell thicknesses. As it can be seen, concentration polarization takes place even near a thin shell.

Fig. 3 shows characteristic distributions of the current through the shell boundary and the electric potential along the symmetry axis. In the graph (b) one can note a significant voltage drop in the space charge region, denoted by ΔV_{SCR}, which in combination with the current through the particle generates electrokinetic instability. The electroconvection caused by the instability is clearly visible in plot (c) in Fig. 2c.

While the velocity value U_∞ is usually used to estimate the electrophoresis intensity, it is convenient to estimate the electroosmosis intensity near a stationary particle by the integral current. In the present work, the value

$$j_{\text{abs}} = 2\pi\left(1 + L^2\right)\int_0^{\pi}\left|j(\theta)\sin\theta d\theta\right|$$

is introduced for this purpose.

By plotting the values ΔV_{SCR} and j_{abs}, realized in different modes, it is possible to construct the current-voltage characteristics of the microparticle. Examples of such characteristics are shown in Fig. 4. The dependence of ΔV_{SCR} on E_∞, as shown in graphs (a) and (c), is almost linear. Graphs (b) and (d) demonstrate behavior similar to electromembrane systems: at low voltage drops, the underlimiting regime is realized (proportionally in proportion to voltage), at moderate voltage drops, the limiting mode is realized (current growth slows down sharply). When the shell thickness is large enough, even the overlimiting regime is realized: when the critical value of ΔV^*_{SCR} is exceeded, electroconvection occurs, intensifying the current. The observed value ΔV^*_{SCR} corresponds to the theoretical predictions of [24].

In Fig. 4, there is a noticeable increase in the current through the particle with increasing thickness of its shell. This is largely due to the increase in the surface area of the particle. At the same time, with increasing shell thickness, the voltage drop in the space charge region also increases, so a stronger field is required for electroconvection to occur near particles with thin shells. Advection does not qualitatively affect the behavior of the system: the voltage drop slightly decreases, the current increases. The current increase is due to the convective inflow of charge carriers into the desalination zone. The flow structure did not undergo qualitative changes even at $U_\infty = 1{,}000$. The slip of the liquid near the shell was not considered in the present work, but its contribution can be expected to be quantitative as well, expressing itself mainly in the shift of the threshold of instability onset to the left [25].

The influence of the charge of the core surface on the effects described above was so insignificant that it is not shown in the diagrams. Any significant effect is observed only in the case when the shell thickness is small and its charge is opposite in sign to the charge of the core surface. This case is studied by the authors in a separate paper, the preprint of which is available on request [26].

Finally, we note that when the absolute value of the shell charge decreases, its selectivity decreases and conductivity increases, which leads to a decrease in ΔV_{SCR}. As a consequence, a stronger field must be applied for a noticeable concentration polarization to occur, and the critical value of ΔV^*_{SCR} shifts to the right. Nevertheless, the shell thickness even in this case determines whether electroconvection will occur at all. Here it is necessary to emphasize the difference of the considered formulation from the electromembrane system with a non-ideal membrane [21]: if in the latter the membrane conductivity plays a determining role in the conductivity of the whole system, in the considered formulation the ion flux can bypass the particle, so the conductivity of the system is determined by the conductivity of the electrolyte.

CONCLUSION

The paper presents the results of numerical simulation of electrokinetics in electrolyte near a spherical dielectric microparticle covered with an ion-selective shell. It is shown that concentration polarization occurs near the shell, regardless of its thickness, but electroconvection can occur only at a sufficiently large thickness of the shell. The electrolyte pumping and the charge on the dielectric surface have no qualitative effect on the dynamics of the system. The results of this work can be used to develop methods for controlling composite microparticles, including biological ones, and to develop methods for investigating the structure of such particles in microdevices.

FUNDING

The work was financially supported by RSF (grant 22-79-10085).

ETHICS DECLARATION

There are no human or animal studies in this paper.

CONFLICT OF INTERESTS

The authors of this paper declare that they have no conflict of interests.

REFERENCES

1. *Paillot R.* M. Smoluchowski – Contribution à la théorie de l'endosmose électrique et de quelques phénomènes corrélatifs (Bulletin de l'Académie des Sciences de Cracovie, mars 1903) // J. Phys.: Theor. Appl. 1904. Vol. 3. No. 1. P. 912. https://doi.org/10.1051/jphystap:019040030091201
2. *Mohammadi R., Afsaneh H., Rezaei B., Zand M.M.* On-chip dielectrophoretic device for cancer cell manipulation: A numerical and artificial neural network study // Biomicrofluidics. 2023. Vol. 17. P. 024102. https://doi.org/10.1063/5.0131806
3. *Dukhin S.S., Deryagin B.V.* Electrophoresis. M.: Nauka. 1976.
4. *Schnitzer O., Yariv E.* Strong-field electrophoresis // J. Fluid Mech. 2012. Vol. 701. Pp. 333–351. https://doi.org/10.1017/jfm.2012.161
5. *Schnitzer O., Zeyde R., Yavneh I., Yariv E.* Weakly nonlinear electrophoresis of a highly charged colloidal particle // Phys. Fluids. 2013. Vol. 25. No. 5. P. 052004. https://doi.org/10.1063/1.4804672
6. *Schnitzer O., Yariv E.* Nonlinear electrophoresis at arbitrary field strengths: small-Dukhin-number analysis // Phys. Fluids. 2014. Vol. 26. No. 12. P. 122002. https://doi.org/10.1063/1.4902331

7. *Tottori S., Misiunas K., Keyser U.F., Bonthuis D.J.* Nonlinear electrophoresis of highly charged nonpolarizable particles // Phys. Rev. Lett. 2019. Vol. 123. No 1. P. 014502. https://doi.org/10.1103/physrevlett.123.014502
8. *Khair A.S.* Nonlinear electrophoresis of colloidal particles // Curr. Opin. Colloid Interface Sci. 2022. Vol. 59. P. 101587. https://doi.org/10.1016/j.cocis.2022.101587
9. *Dukhin S.S.* Electrokinetic phenomena of the second kind and their applications // Adv. Colloid Interface Sci. 1991. Vol. 35. P. 173–196. https://doi.org/10.1016/0001-8686(91)80022-c
10. *Yariv E.* Migration of ion-exchange particles driven by a uniform electric field // J. Fluid Mech. 2010. Vol. 655. Pp. 105–121. https://doi.org/10.1017/s0022112010000716
11. *Frants E.A., Ganchenko G.S., Shelistov V.S., Amiroudine S., Demekhin E.A.* Nonequilibrium electrophoresis of an ion-selective microgranule for weak and moderate external electric fields // Phys. Fluids. 2018. Vol. 30. No. 2. P. 022001. https://doi.org/10.1063/1.5010084
12. *Mishchuk N.A., Takhistov P.V.* Electroosmosis of the second kind // Colloids Surf. A Physicochem. Eng. Asp. 1995. Vol. 95. No. 2–3. Pp. 119–131. https://doi.org/10.1016/0927-7757(94)02988-5
13. *Ganchenko G.S., Frants E.A., Shelistov V.S., Nikitin N.V., Amiroudine S., Demekhin E.A.* Extreme nonequilibrium electrophoresis of an ion-selective microgranule // Phys. Rev. Fluid. 2019. Vol. 4. No. 4. P. 043703. https://doi.org/10.1103/physrevfluids.4.043703
14. *Ganchenko G.S., Frants E.A., Amiroudine S., Demekhin E.A.* Instabilities, bifurcations, and transition to chaos in electrophoresis of charge-selective microparticle // Phys. Fluids. 2020. Vol. 32. No. 5. P. 054103. https://doi.org/10.1063/1.5143312
15. *Kłodzińska E., Szumski M., Dziubakiewicz E., Hrynkiewicz K., Skwarek E., Janusz W., Buszewski B.* Effect of zeta potential value on bacterial behavior during electrophoretic separation // Electrophoresis. 2010. Vol. 31. No. 9. Pp. 1590–1596. https://doi.org/10.1002/elps.200900559
16. *Polaczyk A.L., Amburgey J.E., Alansari A., Poler J.C., Propato M., Hill V.R.* Calculation and uncertainty of zeta potentials of microorganisms in a 1:1 electrolyte with a conductivity similar to surface water // Colloids Surf. A Physicochem. Eng. Asp. 2020. Vol. 586. P. 124097. https://doi.org/10.1016/j.colsurfa.2019.124097
17. *Maurya S.K., Gopmandal P.P., Ohshima H., Duval J.F.L.* Electrophoresis of composite soft particles with differentiated core and shell permeabilities to ions and fluid flow // J. Colloid Interface Sci. 2020. Vol. 558. Pp. 280–290. https://doi.org/10.1016/j.jcis.2019.09.118
18. *Ohshima H.* Approximate analytic expressions for the electrophoretic mobility of spherical soft particles // Electrophoresis. 2021. Vol. 42. No. 21–22. Pp. 2182–2188. https://doi.org/10.1002/elps.202000339
19. *Schnitzer O., Yariv E.* Streaming-potential phenomena in the thin-Debye-layer limit. Part 3. Shear-induced electroviscous repulsion // J. Fluid Mech. 2016. Vol. 786. Pp. 84–109. https://doi.org/10.1017/jfm.2015.647
20. *Frants E.A., Shelistov B.S., Ganchenko G.S., Gorbachev E.V., Alekseev M.S., Demekhin E.A.* Electrophoresis of a dielectric particle in a strong electric field // Ekologicheskiy vestnik nauchnykh tsentrov Chernomorskogo ekonomicheskogo sotrudnichestva. 2021. Vol. 18. No. 4. Pp. 33–40. https://doi.org/10.31429/vestnik-18-4-33-40
21. *Gamchenko G.S., Kalaidin E.N., Chakraborti S., Demekhin E.A.* Hydrodynamic instability under ohmic conditions in imperfect electrical membranes // Doklady Akademii nauk. 2017. Vol. 474. No. 3. Pp. 296–300. https://doi.org/10.7868/s0869565217150063
22. *Maduar S.R., Belyaev A.V., Lobaskin V., Vinogradova O.I.* Electrohydrodynamics near hydrophobic surfaces // Phys. Rev. Lett. 2015. Vol. 114. No. 11. P. 118301. https://doi.org/10.1103/PhysRevLett.114.118301
23. *Nikitin N.V.* Third-order-accurate semi-implicit Runge–Kutta scheme for incompressible Navier-stokes equations // Int. J. Numer. Methods Fluids. 2006. Vol. 51. No. 2. Pp. 221–233. https://doi.org/10.1002/fld.1122
24. *Demekhin E.A., Nikitin N.V., Shelistov V.S.* Direct numerical simulation of electrokinetic instability and transition to chaotic motion // Phys. Fluids. 2013. Vol. 25. No. 12. P. 122001. https://doi.org/10.1063/1.4843095
25. *Shelistov V.S., Demekhin E.A., Ganchenko G.S.* Electrokinetic instability near charge-selective hydrophobic surfaces // Phys. Rev. E. 2014. Vol. 90. No. 1. P. 013001. https://doi.org/10.1103/PhysRevE.90.013001
26. *Ganchenko G.S., Shelistov V.S., Demekhin E.A.* Features of electrophoresis of a composite microparticle with a thin ion-selective shell // Technical Physics Letters (preparing for submission).

COLLOID JOURNAL, 2025, Vol. 87, No. 1, pp. 22–31

SPHERICAL POLYMER GELS CONTAINING SULFONATE GROUPS: SYNTHESIS AND ADSORPTION PROPERTIES

S. G. Laishevkina, L. M. Druian, O. D. Iakobson, E. M. Ivankova, B. M. Shabsels, and N. N. Shevchenko*

Branch of Petersburg Nuclear Physics Institute named by B.P. Konstantinov of National Research Centre "Kurchatov Institute" – Institute of Macromolecular Compounds, Saint Petersburg, Russia

**e-mail: natali.shevchenko29@gmail.com*

Received September 02, 2024
Revised September 19, 2024
Accepted September 22, 2024

Abstract. Porous cross-linked polyelectrolyte microspheres with diameter from 1 to 5 μm based on para-styrene sulfonate or copolymer of para-styrene sulfonate with vinyl acetate were synthesized. The content of sulfonate groups in the obtained polyelectrolyte microspheres is more than 2 mmol/g. It was shown that introduction of hydrophobic comonomer significantly increased the degree of swelling of polyelectrolyte microspheres. It was found that the value of adsorption of model compounds (fuchsin, methylene blue) significantly exceed the concentration of sulfonate groups. Morphology, structure of the surface layer of polyelectrolyte matrices were studied by optical and scanning electron microscopy, FTIR spectroscopy, specific surface by the BET method.

Keywords: *polyelectrolyte microspheres, hydrogels, adsorption of drugs*

DOI: 10.31857/S00232912250103e3

INTRODUCTION

Modern medicine and pharmacology are dynamically developing fields aimed at introducing innovative technologies and improving diagnostic and treatment methods. One of the key challenges in these areas is targeted/targeted delivery of drug substances (DS) preferentially to areas of inflammation, resulting in a significant reduction of adverse reactions of the body to the used drugs and their dosage. In addition, such delivery systems can gradually release the active substance, which reduces the frequency of drug administration and increases the effectiveness of treatment [1]. The most promising materials for the development of drug delivery systems are polymers, which can be presented in the form of particles [2–4], capsules [5], hydrogels [6], dendrimers [7] and others. At the same time, it is hydrogels that are of particular interest to researchers involved in the development of drug delivery systems. They are characterized by high water content, biocompatibility and required mechanical properties. In addition, current knowledge allows the synthesis of hydrogels at macro-, micro- and nano-scale. According to the literature, it is micro- and nanogels that have the greatest potential for the development of drug delivery systems [8–10].

Polymeric drug delivery systems can be divided into two broad groups: bio- and non-biodegradable compositions, the choice between which depends on the specific clinical requirements and the type of drug. Non-biodegradable systems are often used in the field of radiosurgery as embolizates [6], in dentistry as dental restorative materials [4] or universal implantable DS delivery systems [11]. Common polymers for non-biodegradable drug delivery systems are polymethyl methacrylate [12, 13], polyethylene vinyl acetate [14], polyvinyl alcohol [15], and copolymers based on them. Recently, in addition to the previously mentioned polymers, polyelectrolytes have also become the object of active research in the field of targeted DS delivery [5, 16]. This is due to their unique properties: high adsorption capacity and ion exchange ability [17]. This is particularly interesting for extended-release formulations, where DS diffusion is limited by ion exchange between drugs with ionic groups and polyelectrolytes.

Polyanions contain negatively charged ionogenic groups, SO_3^- (COO^-). They demonstrate their effectiveness in the delivery of cationic DS, which is confirmed by a number of examples: polystyrene sulfonate for the delivery of ligustrazine phosphate for the treatment of various eye diseases [3] or $CaCO_3$ particles coated with polyvinyl sulfonate or dextransulfonate for the delivery of doxorubicin hydrochloride for cancer therapy [18]. It appeared that modification of $CaCO_3$ particles with dextransulfonate was the most optimal for subsequent in-vivo studies of such particles. In addition, polyanions can be used for the delivery of hormones such as insulin [2].

Nevertheless, the synthesis of polyelectrolyte-based microspheres is not a simple task. Most published articles use sulfation of polystyrene particles [19, 20] to form sulfonate groups in their structure, but the morphology, electrical surface properties, or swelling of such microspheres in solvents differ significantly compared to microspheres obtained using para-styrene sulfonate as a functional monomer. Another common method for the preparation of microspheres with sulfonate groups is multistep synthesis, which includes protection of sulfonate groups, synthesis of hydrophobic microspheres, and removal of protection [21, 22]. Despite the high content of sulfonate groups in the final microspheres, this method is rather complicated, and some steps are characterized by low yields or the formation of unstable compounds. Therefore, the most promising method is the synthesis of microspheres based on commercially available monomers with sulfonate groups in the reverse emulsion polymerization process.

Thus, cross-linked systems based on polyanions may be promising as non-biodegradable DS delivery systems. In this regard, it is necessary to study the mechanisms of sorption and desorption of drugs on polyelectrolyte microspheres. In the present work we synthesized cross-linked hydrogel microspheres based on polystyrene sulfonate and its copolymer with vinyl acetate in order to study their ability to sorb cationic forms of drugs on the example of fuchsin and methylene blue. The optimal conditions for the preparation of polymeric microspheres by reverse emulsion polymerization were determined and the effect of vinyl acetate co-monomer on the sorption ability of the synthesized particles was studied. The structural characteristics of all polymeric microspheres were investigated using IR spectroscopy, optical and scanning electron microscopy, and BET method. The results showed that the synthesized microspheres have a developed specific surface area and a high content of sulfonate groups (more than 2 mmol/g), most of which are localized in the volume of microspheres. These values are an order of magnitude higher than the concentration of surface sulfonate groups for polystyrene microspheres (obtained after their sulfation). At the same time, the introduction of vinyl acetate as co-monomer reduces the content of sulfonate groups, which, in turn, worsens their sorption properties with respect to fuchsin and methylene blue.

EXPERIMENTAL PART

Materials

Particles were synthesized using the following reagents: sodium styrene sulfonate (SSS) (Sigma Aldrich, Germany), *N,N'*-methylene-bis-acrylamide (MBA) (Vecton LLC, Russia), vinyl acetate (Vecton LLC, Russia), potassium persulfate ($K_2S_2O_8$) (Vecton LLC, Russia), Span 80 (Sigma Aldrich, Germany), Tween 80 (Sigma Aldrich, Germany). Vinyl acetate was purified by vacuum distillation according to standard methods, potassium persulfate was purified by recrystallization from water. Other monomers and emulsifiers were used without prior purification. NaCl, HCl, NaOH, ethanol (Vekton LLC, Russia), cyclohexane (LenReactiv JSC, Russia) without preliminary purification were used for particle studies. Fuchsin (Vekton LLC, Russia) and methylene blue (Vekton LLC, Russia) were used without preliminary purification.

Synthesis of polystyrene sulfonate particles

Synthesis of polymer particles was carried out in a three-neck flask equipped with a top-driven stirrer and a reflux condenser. First, the emulsifier Span 80 was dissolved in 12 ml of cyclohexane at 50° C in the flask. In parallel, a solution of the reagents in water was prepared by successively dissolving Tween 80, SSS (1.98 g), vinyl acetate (0–10 wt% of SSS-Na), MBA (50 wt% of total monomer content) and $K_2S_2O_8$ (3 wt% of total monomer content) on an ultrasonic bath at 50°C. The amount of emulsifiers was 5 wt% of the total emulsion content (monomers and solvents), and the Tween 80/Span 80 ratio was 16/84. Immediately after dissolution of $K_2S_2O_8$, the prepared solution was introduced into a three-neck flask. The resulting emulsion was stirred for 30 minutes at 600 rpm at 50°C for 30 minutes to reach equilibrium. The temperature was then raised to 70°C and the reaction was continued for 4 hours with constant stirring. The unreacted monomers, emulsifier and cyclohexane were removed by centrifugation for 30 minutes at 10,000 rpm (Centrifuge 5804, Eppendorf, Germany), redispersing the precipitated particles in the water-alcohol mixture.

Determination of particle size and shape

The size and shape of particles were determined by optical and scanning electron microscopy (SEM). Optical microscopy was performed using an optical microscope (MIKMED-5, Russia) equipped with lenses with magnification ×100 and ×40. For the study, a dispersion of particles in water was prepared, after which it was applied to a slide and the particles were photographed in the swollen state. SEM was performed on a SUPRA 55 VP scanning electron microscope (Germany). For SEM, dried samples were applied on glass substrates and then coated with Au/Pd. The diameter of microspheres was calculated using the Image J software.

Determination of the content of sulfonate groups

The content of sulfonate groups was determined by conductometric titration and by measuring the ion exchange capacity. Measurement of ion exchange capacity was carried out according to the standard method, for this purpose 0.3 g of particles were dispersed in 10 ml of HCl (0.5 n.) and incubated for 24 hours, after which the particles were washed (excess acid was removed by centrifugation) and dried by lyophilic drying. The particles were then dispersed in a 20% aqueous solution of NaCl and incubated for 24 hours. The acid released as a result of ion exchange under argon current was titrated with aqueous NaOH solution (0.01 n.) in the presence of phenolphthalein indicator.

Conductometric titration was carried out in argon current using 0.1% wt. dispersion of particles. For this purpose, a known excess of HCl (0.01 n.) was introduced into the dispersion, after which the introduced HCl and sulfonate groups were titrated with an aqueous solution of NaOH (0.01 n.), taking values of the electrical conductivity of the dispersion using a SevenMulti conductometer (MetlerToledo, Switzerland).

Determination of specific surface area of particles

The specific surface area of particles was measured using a NOVA 1200e surface analyzer (Quantachrome, USA). Prior to measurements, the sample was degassed in a nitrogen current at reduced pressure.

FTIR spectroscopy

The spectral characteristics of the synthesized samples were studied by FTIR spectroscopy of disturbed total internal reflection. FTIR spectra were taken on an FTIR spectrometer FTIR-Affinity-1S (Shimadzu, Japan) with a diamond prism. All spectra represent the average of 32 scans taken in the wave number range of 20,000–600 cm^{-1}.

Determination of sorption of fuchsin and methylene blue

Determination of sorption ability of synthesized microspheres with respect to fuchsin and methylene blue (MB) was carried out by spectrophotometric method. For this purpose, 1.1–4.3 mg of synthesized particles were incubated in an aqueous solution of fuchsin or methylene blue with a concentration of $4.8 \cdot 10^{-5}$ to $1.45 \cdot 10^{-3}$ mol/L for 1.5 hours. The particles were then precipitated by centrifugation and the supernatant solutions with unsorbed fuchsin/MB were studied by optical spectroscopy in the visible region ($\lambda = 542$ nm and $\lambda = 662$ nm for fuchsin and MB). The concentration of fuchsin and MB was determined using a previously constructed calibration line.

The experimental data on the sorption capacity with respect to hydrocarbons were analyzed using the Langmuir and Freundlich models. For this purpose, linear isotherms were constructed and parameters were calculated according to formulas (1) and (2) for the Langmuir and Freundlich models, respectively.

$$\frac{1}{q} = \frac{1}{C_e \cdot K_L} \cdot \frac{1}{q_{max}} + \frac{1}{q_{max}}, \tag{1}$$

where q is the adsorption value, mol/g; q_{max} is the maximum adsorption value, mol/g; K_L is the Langmuir constant, g/mmol; C_e is the equilibrium concentration, mol/g.

$$\ln q = \ln K_F + \frac{1}{n} \ln C_e, \tag{2}$$

where q – adsorption value, mol/g; K_F – Freundlich constant (at $C = 1$ mol/L K_F is equal to q_{max}); $1/n$ – constant (adsorption index depending on temperature and nature of adsorbent).

In addition, the parameter R_L, the partition coefficient (equilibrium parameter), was calculated for the Langmuir model using formula (3).

$$R_L = \frac{1}{1 + K_L \cdot C_0}, \tag{3}$$

where C_0 – initial concentration of absorbate, mol/g.

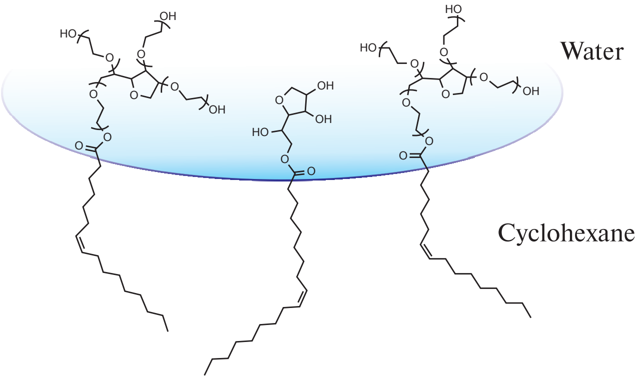

Fig. 1. Schematic arrangement of emulsifiers at the water–cyclohexane interface.

Table 1. Composition of the monomer mixture

N	Concent. mon, mol/L	SSS-Na: MBA, mol. %	Vinyl acetate, wt%	Emulsifier		
				Tween 80/ Span 80	Content, wt%	HLB
PSS	2	60:40	–	16/84	5	6
P(SSS-VA)	2	60:40	10	16/84	5	6

The applicability of the theoretical model of adsorption isotherms to the obtained experimental data was evaluated based on the coefficient of determination (R^2) calculated in Origin 2019 software.

RESULTS AND DISCUSSION

Synthesis of microspheres

Polyelectrolyte particles promising for drug sorption were synthesized in this work. The aim of this work was to investigate the sorption properties of microspheres based on cross-linked polystyrene sulfonate with respect to cationic drugs. Polyelectrolyte particles were synthesized by reverse emulsion copolymerization of SSS-Na and MBA, and copolymerization of SSS-Na, MBA and vinyl acetate P(SSS-VA) (Table 1). Polystyrene sulfonate (PSS) is a biocompatible polymer that is used for the treatment of hyperkalemia. The introduction of the crosslinking agent MBA into the reaction system was necessary to form crosslinked polymer chains to prevent their solubility in the aqueous phase. Vinyl acetate was used in order to form hydrophobic sites in the polymer chain structure, which can improve the interaction of microspheres with water-insoluble DS. In addition, vinyl acetate will allow the formation of polyvinyl alcohol links in the polymer structure (due to further hydrolysis of polyvinyl acetate links). Polyvinyl alcohol links contribute to the improvement of mucoadhesive properties of polymer microspheres, which is important when microspheres are used as embolizers or universal implantable DS delivery systems. Cyclohexane was chosen as

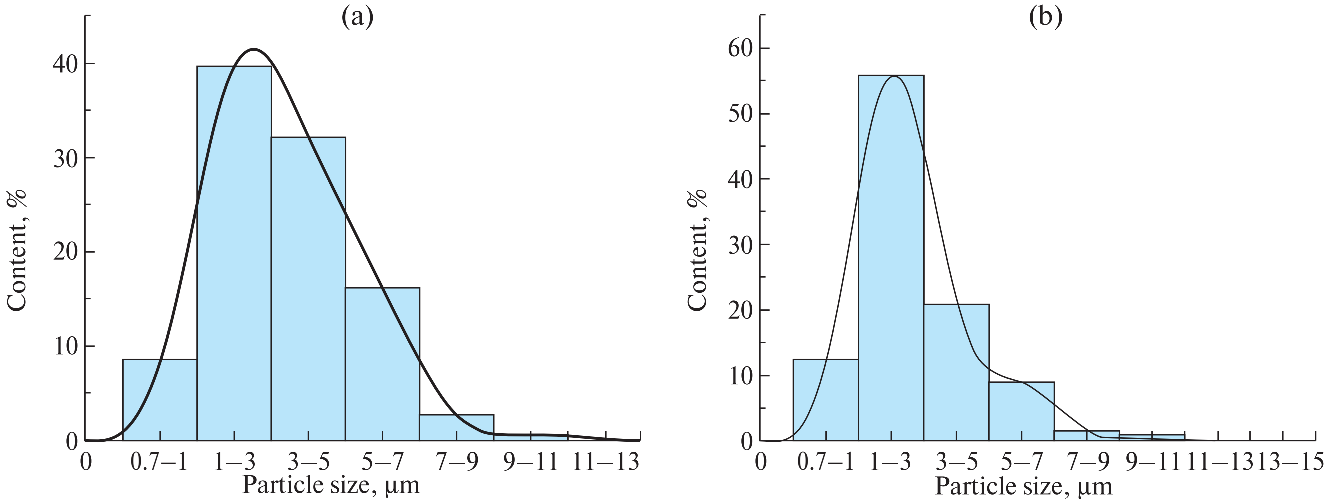

Fig. 2. Particle size distribution for PSS particles (a) and P(SSS-VA) copolymer (b).

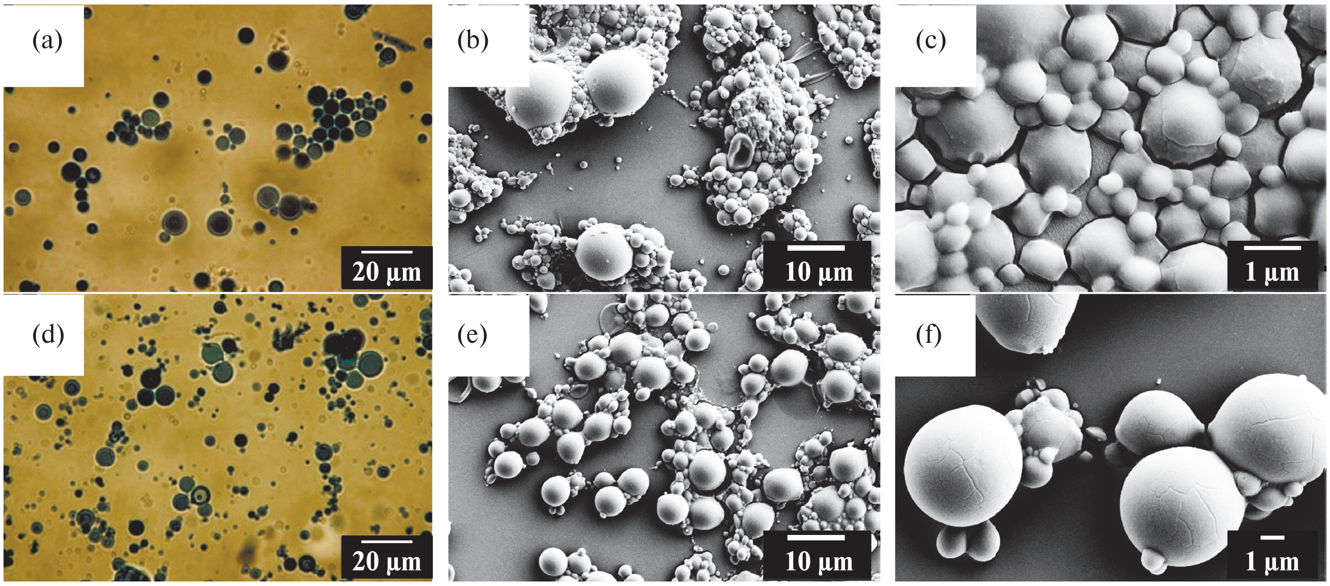

Fig. 3. Optical microscopy micrographs of PSS (a) and P(SSS-VA) particles (d); SEM micrographs of PSS particles (b, c) and P(SSS-VA) copolymer particles (e, f).

the dispersion medium. The stability of the resulting emulsion is important in the reaction. Therefore, Span 80 and Tween 80 emulsifiers were chosen as the emulsifying system. Span 80 has a low hydrophilic-lipophilic balance (HLB) value (4.3), which effectively stabilizes the monomer droplets in the oil phase. The auxiliary emulsifier Tween 80 with a HLB value of 15 provided uniform distribution of polar substances in the aqueous phase and improved the stability of emulsions by reducing droplet coalescence. In addition, the hydrophobic tails of these emulsifiers are identical and the hydrophilic head differs greatly in size (Fig. 1), resulting in maximum synergistic effect [23]. In addition, according to the study [24], the most effective stabilization of emulsions is observed when emulsifiers are introduced into different phases (lipophilic – into oil phase, hydrophilic – into water phase). In this case, after mixing the phases, there is no diffusion of surfactant (surfactant) into the aqueous phase, on the contrary, surfactant molecules are immediately oriented at the interface in the desired direction, which provides the formation of a denser layer at the interface. Therefore, in this work, surfactants were introduced into different phases and after mixing were kept for 30 min to establish equilibrium.

The emulsions formed were white colored colloidal systems. After equilibrium was established, the temperature was increased to 70°C to start the reaction polymerization. After two hours of the reaction, a sharp increase in the viscosity of the system was observed, which is probably due to the high content of the polymer swollen in water relative to the volume of the aqueous phase. The synthesis resulted in the formation of hydrogel spherical microspheres with a diameter of 1–5 μm in the swollen state (Fig. 2), as evidenced by optical microscopy photographs (Fig. 3a, d). The introduction of vinyl acetate promoted the formation of particles with a narrower particle size distribution, which may be due to a slight increase in the amount of emulsifiers in the system, dependent on the mass of the introduced co-monomers. In addition, the synthesized microspheres had a large specific surface area, the value of specific surface area for PSS and P(SSS-VA) microspheres was 2.09 and 2.23 m^2/g, respectively. However, it is worth noting that this size of microspheres is not suitable for all drug delivery routes. It is known that when polystyrene sulfonate particles are used orally, particles smaller than 5 μm can be absorbed through the mucosa and deposited in the tissues of the mononuclear phagocyte system.

The size and shape of polymer particles based on PSS and copolymer P(SSS-VA) were also investigated by scanning electron microscopy. It can be seen from the photographs that all particles have a spherical shape. At the same time, the size of particles in SEM (dry form) and optical microscopy (swollen form) photographs are different, which confirms their gel-like structure. In addition, the swelling degree of the particles based on cross-linked PSS and P(SSS-VA) copolymer, were ~20% and 95%, respectively. The swelling degree of P(SSS-VA) is higher compared to that of PSS despite the fact that the MBA content in the conditions for synthesizing P(SSS-VA) microspheres is higher by 10 wt%. The introduction of VA may have affected the phase homogeneity at the water–cyclohexane interface, which affected how the MBA was arranged in the polymer mesh structure. The IR spectroscopy results (Fig. 4) showed that the vinyl groups of MBA were present in the polymer structure and were not involved in the polymerization reaction. Taking this into account, it can be assumed that the crosslinking agent is incorporated into the polymer chain by only one vinyl group.

FTIR spectroscopy

The chemical composition of the obtained particles was analyzed by FTIR spectroscopy of disturbed total internal reflection. The obtained FTIR spectra for the samples of PSS and copolymer P(SSS-VA) are presented in Fig. 4. The polystyrene sulfonate structure in the particles is indicated by the transmission bands at 673 cm^{-1}, which corresponds to C–S and C–H bonds in the sulfonate group

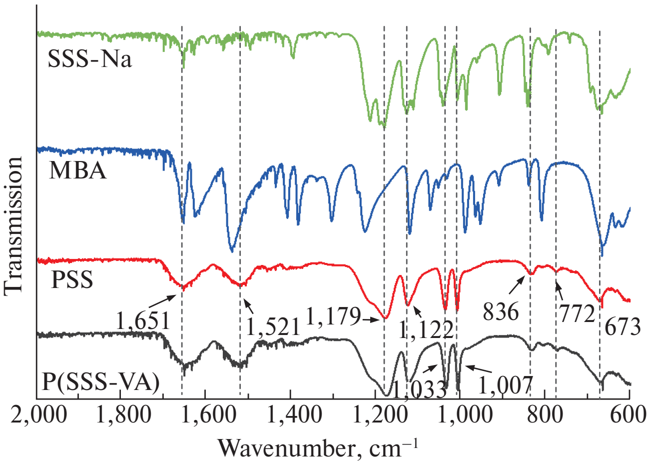

Fig. 4. FTIR spectra of SSS-Na (green), MBA (blue) and synthesized particles PSS (red) and P(SSS-VA) (black).

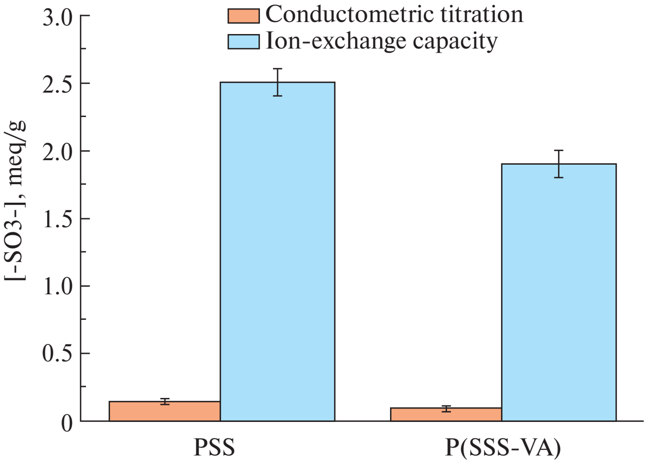

Fig. 5. Content of sulfonate groups in the synthesized particles determined by conductometric titration (orange) and ion exchange capacity measurement (blue).

attached to the aromatic ring. The valence asymmetric vibrations at 1,179 cm^{-1} and valence symmetric vibrations at 1,033 cm^{-1} also indicate the presence of the group SO_3^-, substituted in the para-position in the structure, which is confirmed by the planar vibrations at 1,122 cm^{-1} and 1,007 cm^{-1}. The transmission bands at 836 cm^{-1} and 772 cm^{-1} correspond to δ(C–H) deformation vibrations of the aromatic ring. The bandwidth at 1,651 cm^{-1} is much broader relative to the starting monomers. This may be due to the simultaneous overlap of the ν(C=C) valence vibrations of the aromatic ring of PSS and the ν(C–O) valence vibrations belonging to the MBA structure with the ν(C=C) valence vibrations of the vinyl group of MBA (bandwidth at 1,620 cm^{-1}). The content of MBA particles is also indicated by a band at 1,521 cm^{-1} corresponding to δ(N–H) strain vibrations [25]. However, the IR spectra of P(SSS-VA) particles lack the characteristic transmission bands at 1,018 cm^{-1}, 1,206 cm^{-1} and 1,755 cm^{-1} corresponding to C–O, O–C=O and C=O vibrations in the VA structure. This may indicate that the vinyl acetate content in the copolymer structure is below the sensitivity threshold of the method.

Sulfonate group content

The content of sulfonate groups in the synthesized microspheres was studied by 2 methods: conductometric titration and measurement of ion exchange capacity. As can be seen from Fig. 5, the results for the two methods are very different. The hydrogel/solvent-permeable structure of the microspheres contributed to the fact that sulfonate groups located both on the surface and in the entire volume of the particles participated in ion exchange. Probably due to diffusion limitations, only sulfonate groups localized in the surface layer of the microspheres could be titrated by conductometric titration. Whereas the measurement of ion exchange capacity implied a prolonged incubation of particles in aqueous solutions of HCl and NaOH, which made it possible to exclude diffusion limitations and measure the total content of sulfonate groups available for ion exchange. The introduction of VA into the composition of microspheres led to a decrease in the content of sulfonate groups by 33 and 24% for conductometric titration and measurement of ion exchange capacity, respectively, which can serve as an indirect confirmation of the presence of VA in the copolymer structure.

Adsorption of fuchsin and methylene blue

Two drugs were chosen to study the sorption properties of the synthesized microspheres: methylene blue (MB) and fuchsin. Methylene blue is a multifunctional drug with antimicrobial properties and is used for the treatment of

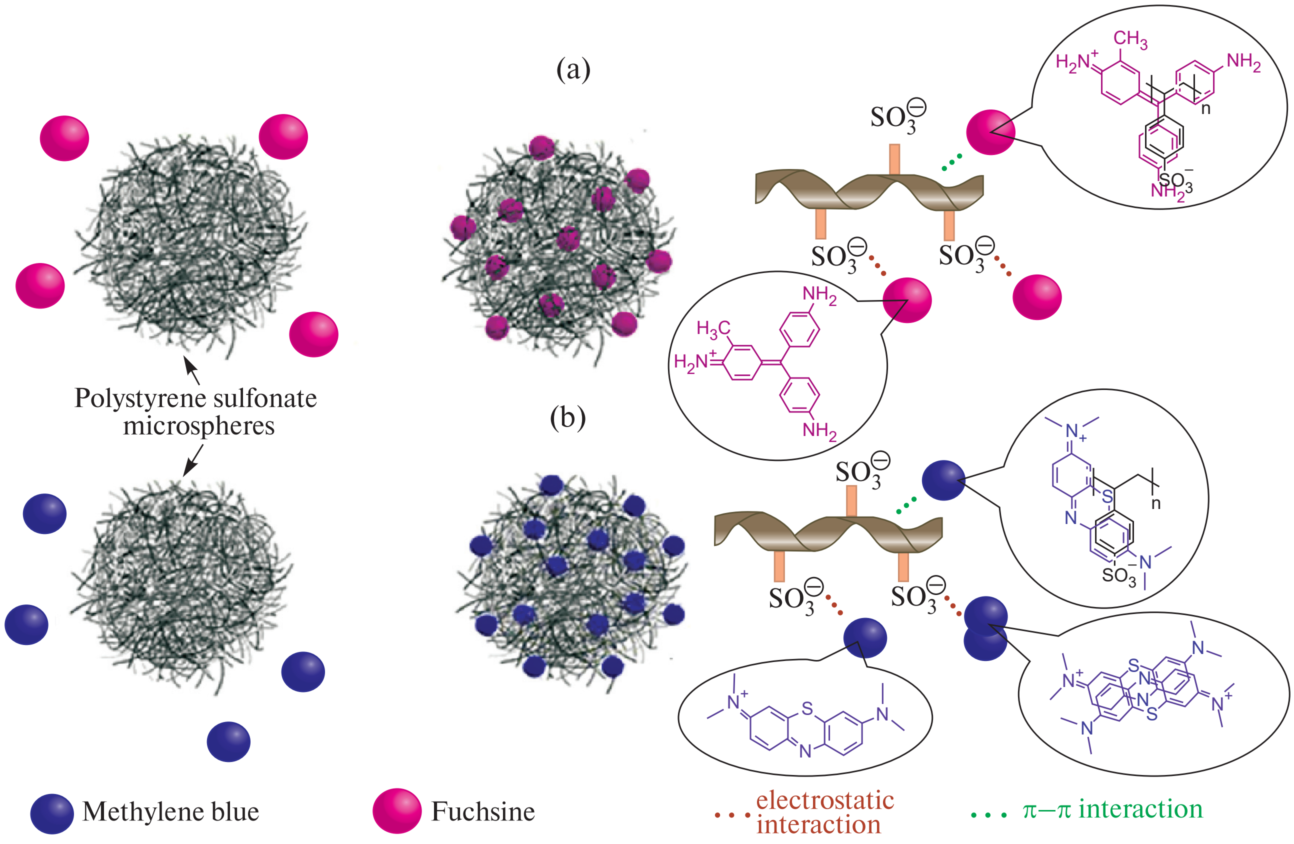

Fig. 6. Scheme of interaction of microspheres with fuchsin (a) and methylene blue (b).

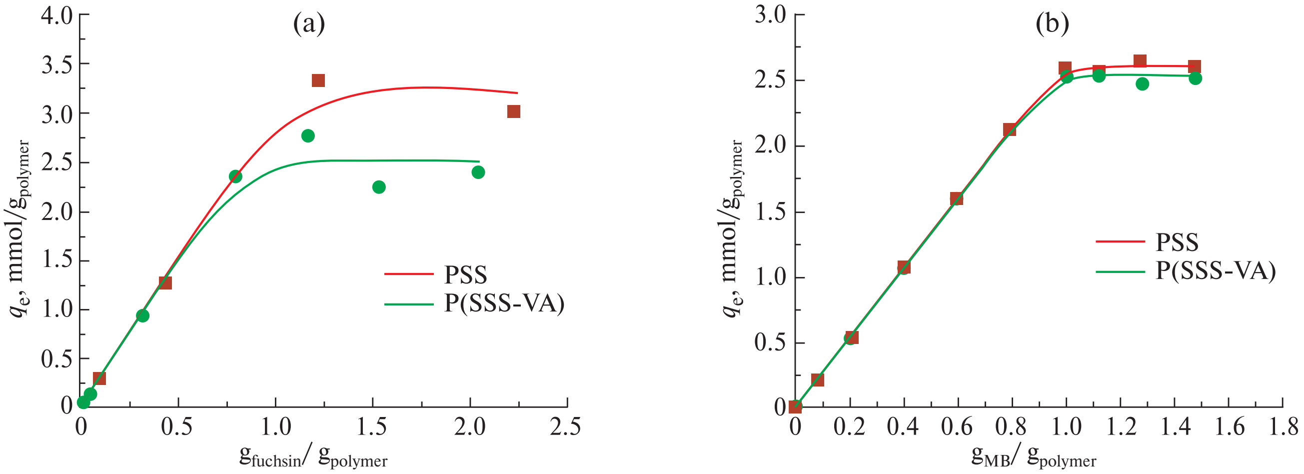

Fig. 7. Adsorption isotherms of fuchsin (a) and methylene blue (b) on the synthesized microspheres.

Table 2. Main parameters of models of fuchsin and MB adsorption isotherms on PSS and P(SSS-VA) microspheres

Model	Model parameters	Fuchsin		Methylene blue	
		PSS	P(SSS-VA)	PSS	P(SSS-VA)
Langmuir	q_{exp}, mmol/g	3.3	2.3	2.7	2.5
	$q_{max\ theor}$, mmol/g	5.2	4.6	10.1	7.6
	$K_L \cdot 10^{-3}$	0.83	0.78	0.29	0.41
	R_L (at 0.25)	0.83	0.84	0.93	0.91
	R^2	0.83	0.86	0.64	0.63
Freundlich	$1/n$	0.86	0.81	0.91	0.88
	K_F, mmol/g	2.48	2.02	2.33	1.09
	R^2	0.97	0.95	0.98	0.97

urinary tract diseases, methemoglobinemia, and as a dye in various medical manipulations. Fuchsin also exhibits antimicrobial properties and can be used as an antiseptic for the treatment of wounds and other surfaces. These compounds were chosen as model samples because of their positively charged cationic structure, which is able to interact with the sulfonate groups in the structure of the synthesized microspheres. The interaction of MB and fuchsin with the particles was carried out due to ion–ion interaction (Fig. 6), as well as due to other types of bonding (hydrogen, π–π interaction, etc.).

The sorption properties of the synthesized particles with respect to MB and fuchsin were studied by spectrophotometry. Fig. 7 shows the adsorption isotherms of fuchsin and MB from aqueous solutions onto the synthesized PSS microspheres and copolymer P(SSS-VA). The figure shows that all isotherms belong to class L according to the Charles Giles classification. They are characterized by an increase in adsorption with rising equilibrium concentration of adsorbate and its gradual approach to the maximum value of sorption capacity. According to the data obtained, the maximum values of fuchsin sorption after 2 hours are 3.3 and 2.3 mmol/g for PSS and P(SSS-VA), respectively. For MB, the maximum sorption capacity after 2 hours was 2.7 and 2.5 mmol/g for PSS and P(SSS-VA), respectively. It is worth noting that the obtained values exceed the content of sulfonate groups available for ion–ion interaction. In this connection, it can be assumed that multilayer adsorption of fuchsin and MB onto the synthesized particles occurs.

The adsorbent-adsorbate interactions were investigated by analyzing the linear adsorption isotherms using the Langmuir (equation (1)) and Freundlich (equation (2)) models. The linear correlations of the Langmuir and Freundlich isotherms are shown in Fig. 8. The calculated constants corresponding to each model, as well as the coefficient of determination, showing the convergence of theoretical and experimental data, are presented in Table 2.

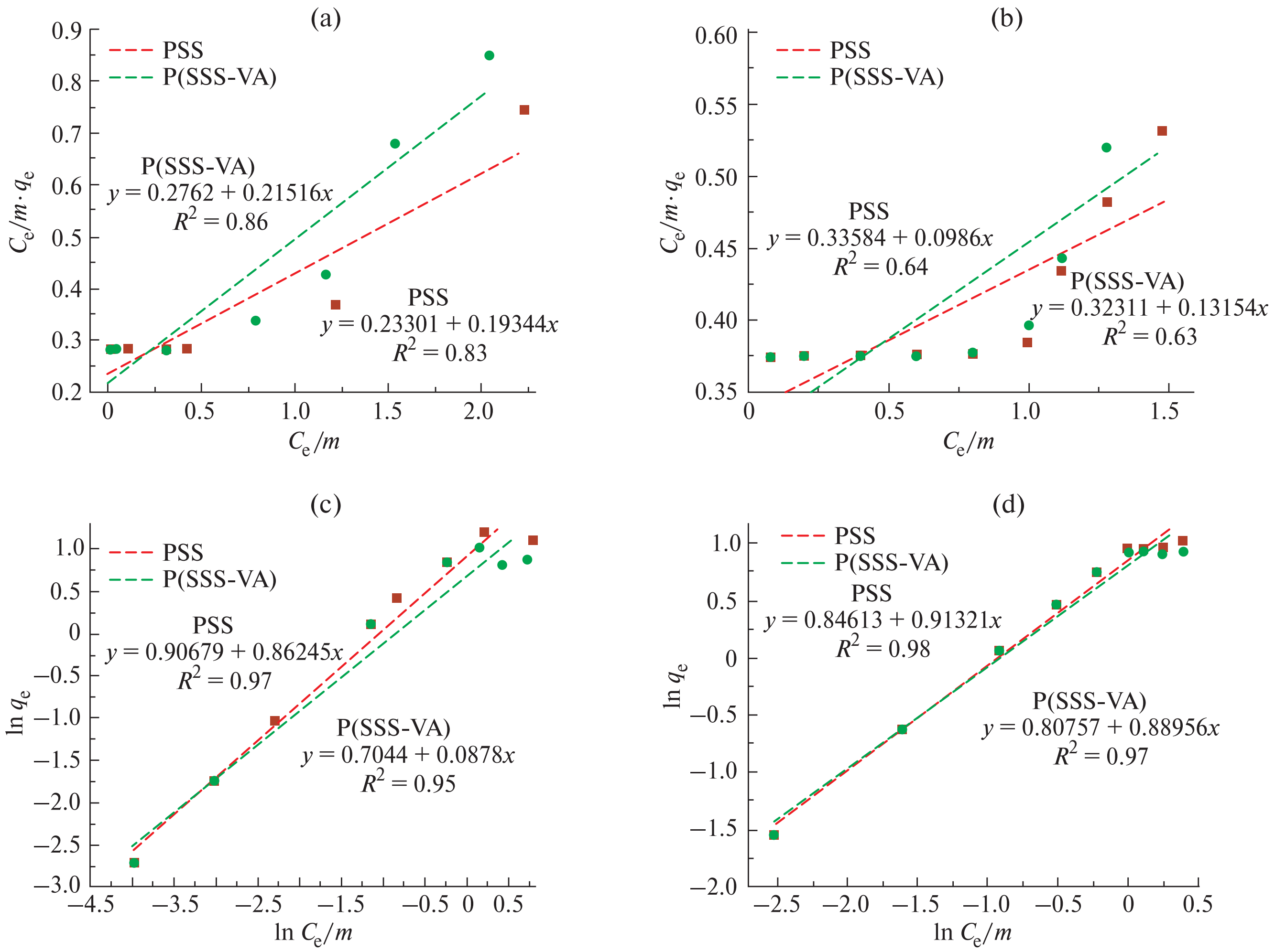

Fig. 8. Linear correlations of Langmuir isotherms for fuchsin (a) and methylene blue (b); linear correlations of Freundlich isotherms for fuchsin (c) and methylene blue (d).

The Langmuir model implies the formation of a monolayer of adsorbate molecules due to their adsorption on a homogeneous solid surface containing a finite number of active centers with equal energy. The Freundlich model describes multilayer adsorption of adsorbate on a homogeneous solid surface with active centers having different adsorption energies. The obtained coefficients of determination for the Langmuir model showed low values (0.63–0.86) for all investigated microspheres for both adsorption towards fuchsin and MB. This indicates the low applicability of this theory to the processes occurring during adsorption. The Freundlich model ($R^2 = 0.95–0.98$) was found to be the best fitting model for all microspheres. This indicates the formation of several layers of fuchsin and MB molecules both on the surface and in the volume of the polymer microspheres. In addition, in the Freundlich model, the parameter $1/n$ is a power-law parameter and shows the nature of adsorption proceeding. At $1/n = 1$, the distribution of adsorbed molecules between the two phases is independent of concentration; at $1/n$ equal to 0, adsorption is irreversible; at $1/n < 1$ adsorption is favorable, and at $1/n > 1$ adsorption is unfavorable. For this work, the $1/n$ was in the range of 0.81–0.91 in all cases, indicating favorable adsorption of fuchsin and MB onto the synthesized particles.

Taking into account the use of the Freundlich multilayer adsorption model and the increased value of the maximum sorption capacity relative to the content of sulfonate groups in the synthesized microspheres, it can be assumed that the adsorption of fuchsin and MB occurs not only due to ion–ion interaction. It is possible that other interactions, such as hydrogen bonds [26] or π–π stacking between the aromatic rings of DS and the aromatic ring in the PSS structure, are also important in adsorption. In addition, it is known that MB is prone to self-association and formation of dimers and trimers [27], so it can be assumed that not only monomeric MB molecules, but also dimers and trimers are involved in adsorption, which may be the reason for such a high sorption capacity.

CONCLUSION

Cross-linked polystyrene sulfonate microspheres were synthesized by reverse emulsion polymerization with and without the use of VA monomer. It was shown that this method formed microspheres with a high content of sulfonate groups, which were localized both in the surface layer and in the volume of the microspheres. Such localization of sulfonate groups influences the sorption properties of microspheres with respect to model cationic chromophores – fuchsin and methylene blue. The obtained polyelectrolyte microspheres possess developed specific surface area, which was confirmed by BET method. The obtained results indicate that the polyelectrolyte microspheres obtained are promising for their further study as carriers of hydrocarbons.

FUNDING

The work was performed within the framework of the state assignment (No. 124013000730-3).

ETHICS DECLARATION

There are no human or animal studies in this paper.

CONFLICT OF INTERESTS

The authors declare that they have no conflict of interests.

REFERENCES

1. *Adepu S., Ramakrishna S.* Controlled drug delivery systems: current status and future directions // Molecules. 2021. Vol. 26. No. 19. P. 5905. https://doi.org/10.3390/molecules26195905
2. *Takenaga M., Serizawa Y., Azechi Y., Ochiai A., Kosaka Y., Igarashi R., Mizushima Y.* Microparticle resins as a potential nasal drug delivery system for insulin // J. Control. Release. 1998. Vol. 52. Nos. 1–2. Pp. 81–87. https://doi.org/10.1016/S0168-3659(97)00193-4
3. *Dong L., Zhang H., Zhang G., Li F., Li M., Wang H., Ye X., Ren X., Zhang J., Peng C., Liu H., Wu L.* Polystyrene sulfonate resin as an ophthalmic carrier for enhanced bioavailability of ligustrazine phosphate controlled release system // J. Pharm Sci. 2024. Vol. 113. No. 9. Pp. 2786–2794. https://doi.org/10.1016/j.xphs.2024.07.002
4. *Imazato S., Kitagawa H., Tsuboi R., Kitagawa R., Thongthai P., Sasaki J.* Non-biodegradable polymer particles for drug delivery: A new technology for "bio-active" restorative materials // Dent. Mater. J. 2017. Vol. 36. No. 5. Pp. 524–532. https://doi.org/10.4012/dmj.2017-156
5. *Kalenichenko D., Nifontova G., Karaulov A., Sukhanova A., Nabiev I.* Designing functionalized polyelectrolyte microcapsules for cancer treatment // Nanomaterials. 2021. Vol. 11. No. 11. P. 3055. https://doi.org/10.3390/nano11113055
6. *Kedik S.A., Suslov V.V., Shnyak E.A., Domnina Yu.M.* Gel-forming polymers for the creation of liquid embolizates // Razrabotka i registratsiya lekarstvennykh sredstv. 2017. Vol. 21. No. 4. Pp. 56–63.
7. *Wang J., Li B., Qiu L., Qiao X., Yang H.* Dendrimer-based drug delivery systems: history, challenges, and latest developments // J. Biol. Eng. 2022. Vol. 16. No. 18. P. 18. https://doi.org/10.1186/s13036-022-00298-5
8. *de Lima C.S.A., Balogh T.S., Varca J.P.R.O., Varca G.H.C., Lugão A.B., Camacho-Cruz L.A., Bucio E., Kadlubowski S.S.* An updated review of macro, micro, and nanostructured hydrogels for biomedical and pharmaceutical applications // Pharmaceutics. 2020. Vol. 12. No. 10. P. 970. https://doi.org/10.3390/pharmaceutics12100970
9. *Wechsler M.E., Stephenson R.E., Murphy A.C., Oldenkamp H.F., Singh A., Peppas N.A.* Engineered microscale hydrogels for drug delivery, cell therapy, and sequencing // Biomed. Microdevices. 2019. Vol. 21. P. 31. https://doi.org/10.1007/s10544-019-0358-0
10. *Oh J.K., Drumright R., Siegwart D.J., Matyjaszewski K.* The development of microgels/nanogels for drug delivery applications // Prog. Polym. Sci. 2008. Vol. 33. No. 4. Pp. 448–477. https://doi.org/10.1016/j.progpolymsci.2008.01.002
11. *Stewart S.A., Domínguez-Robles J., Donnelly R.F., Larrañeta E.* Implantable polymeric drug delivery devices: classification, manufacture, materials, and clinical applications // Polymers (Basel). 2018. Vol. 10. No. 12. P. 1379. https://doi.org/10.3390/polym10121379
12. *Bettencourt A., Almeida A.J.* Poly(methyl methacrylate) particulate carriers in drug delivery // J. Microencapsul. 2012. Vol. 29. No. 4. Pp. 353–367. https://doi.org/10.3109/02652048.2011.651500
13. *Shaked E., Shani Y., Zilberman M., Scheinowitz M.* Poly(methyl methacrylate) particles for local drug delivery using shock wave lithotripsy: In vitro proof of concept experiment // J. Biomed. Mater. Res. B Appl. Biomater. 2015. Vol. 103. No. 6. Pp. 1228–1237. https://doi.org/10.1002/jbm.b.33301
14. *Schneider C., Langer R., Loveday D., Hair D.* Applications of ethylene vinyl acetate copolymers (EVA) in drug delivery systems // J. Control. Release. 2017. Vol. 262. Pp. 284–295. https://doi.org/10.1016/j.jconrel.2017.08.004
15. *Rivera-Hernández G., Antunes-Ricardo M., Martínez-Morales P., Sánchez M.* Polyvinyl alcohol based-drug delivery systems for cancer treatment // Int. J. Pharm. 2021. Vol. 600. P. 120478. https://doi.org/10.1016/j.ijpharm.2021.120478

16. *Lankalapalli S., Kolapalli V.R.M.* Polyelectrolyte complexes: A review of their applicability in drug delivery technology // Indian J. Pharm. Sci. 2009. Vol. 71. No. 5. Pp. 481–487. https://doi.org/10.4103/0250-474X.58165
17. *Laishevkina S.G., Iakobson O.D., Ivankova E.M., Shabsels B.M., Shevchenko N.N.* Effect of the structure of sulfonated polyelectrolyte matrices on ion adsorption Cu^{2+} // Colloid Journal. 2024. Vol. 86. No. 1. Pp. 94–105. https://doi.org/10.31857/S0023291224010092
18. *Sudareva N., Suvorova O., Saprykina N., Vlasova H., Vilesov A.* Doxorubicin delivery systems based on do ped $CaCO_3$ cores and polyanion drug conjugates // J. Microencapsul. 2021. Vol. 38. No. 3. Pp. 164–176. https://doi.org/10.1080/02652048.2021.1872724
19. *Li F., Ye X., Li M., Nie Q., Wang H., Zhang G., Dong L., Wang C., Wu L., Liu H., Wang L., Peng C., Zhang J.* Enhanced ophthalmic bioavailability and stability of atropine sulfate via sustained release particles using polystyrene sulfonate resin // Int. J. Pharm. 2024. Vol. 660. P. 124294. https://doi.org/10.1016/j.ijpharm.2024.124294
20. *Jahn P., Zelner M., Freger V., Ulbricht M.* Polystyrene sulfonate particles as building blocks for nanofiltration membranes // Membranes (Basel). 2022. Vol. 12. No. 11. P. 1138. https://doi.org/10.3390/membranes12111138
21. *Tiwari R., Walther A.* Strong anionic polyelectrolyte microgels // Polym. Chem. 2015. Vol. 6. No. 31. Pp. 5550–5554. https://doi.org/10.1039/c5py00426h
22. *Hofman A.H., Pedone M., Kamperman M.* Protected poly(3-sulfopropyl methacrylate) copolymers: synthesis, stability, and orthogonal deprotection // ACS Polymers Au. 2022. Vol. 2. No. 3. Pp. 169–180. https://doi.org/10.1021/acspolymersau.1c00044
23. *Fu Z., Liu M., Xu J., Wang Q., Fan Z.* Stabilization of water-in-octane nano-emulsion. Part I: Stabilized by mixed surfactant systems // Fuel. 2010. Vol. 89. No. 10. Pp. 2838–2843. https://doi.org/10.1016/j.fuel.2010.05.031
24. *Voronina N.S., Nechaev A.I., Strel'nikov V.N. Val'tsifer V.A.* Inverse Emulsion Copolymerization of acrylamide and 2-acrylamido-2-methylpropane sulfonic acid sodium salt for preparing water-soluble drag reduction additives // Russ. J. Appl. Chem. 2021. Vol. 94. Pp. 748–757. https://doi.org/10.1134/S1070427221060082
25. *Reddy B.V., Rao G.R.* Vibrational spectra and modified valence force field for N,N'-methylenebisacrylamide // Indian J. Pure Appl. Phys. 2008. Vol. 46. No. 9. Pp. 611–616.
26. *Li C., He Y., Zhou L., Xu T., Hu J., Peng C., Liu H.* Fast adsorption of methylene blue, basic fuchsin, and malachite green by a novel sulfonic-grafted triptycene-based porous organic polymer // RSC Adv. 2018. Vol. 8. No. 73. Pp. 41986–41993. https://doi.org/10.1039/C8RA09012B
27. *Florence Ng., Naorem H.* Dimerization of methylene blue in aqueous and mixed aqueous organic solvent: a spectroscopic study // J. Mol. Liq. 2014. Vol. 198. Pp. 255–258. https://doi.org/10.1016/j.molliq.2014.06.030

COLLOID JOURNAL, 2025, Vol. 87, No. 1, pp. 32–36

STABILIZATION OF BULK NANOBUBBLES WITH A HYDRATE LAYER

© 2025 Yu. K. Levin*

Institute of Applied Mechanics of the Russian Academy of Sciences,
Moscow, Russia

**e-mail: iam-ras@mail.ru*

Received September 24, 2024
Revised November 05, 2024
Accepted November 17, 2024

Abstract. The stabilization of bulk nanobubbles is considered with the balance of the Laplace pressure at their boundary due to surface tension and electrostatic pressure due to Coulomb forces. The presence of a hydrate layer of thickness ~1 nm with a tangential orientation of water dipoles around it is taken into account, the low permittivity of which, approximately equal to 3, increases the pressure at the nanobubble boundary. The sizes and charge of a stable nanobubble are determined. It is shown that in salt water, the hydration layer, regardless of the charge of the nanobubble, increases the pressure at its boundary by almost 30 times, and in fresh water – several times less.

Keywords: *dielectric liquid medium, Coulomb and Laplace pressure, hydration layer, anomalous permittivity, size and charge of nanobubbles*

DOI: 10.31857/S00232912250104e4

INTRODUCTION

Interest in bulk nanobubbles (BNBs) in water is associated with the prospects of their application in various fields [1–30]. A distinction is made between surface nanobubbles (SNBs) and bulk nanobubbles (BNBs). The main difference between them is that the former is stationary and the latter is mobile. Nanobubble technologies are widely demanded to address climate change, environmental protection, cost and energy reduction in industrial processes such as flotation, aeration and ozonation, which can remove pollutants and color, disinfect water and oxidize organic pollutants. Also, BNBs are used to solve problems in ecology, agriculture, in medicine/biomedical, in optimizing therapeutic and diagnostic methods and other fields due to their small size, large specific surface area, long residence time in water, high mass transfer capacity, and high zeta potential [3]. The use of BNBs in the treatment of commercial and domestic wastewater instead of the previously used biological approaches reduces energy costs, increases efficiency, and eliminates expensive chemicals and multi-stage treatment [6]. Therefore, the study of the properties of BNBs, including their stability, is relevant, which explains the wide discussion of this issue in the literature.

Atomic force microscopy experiments for the detection of SNPs can be considered as already proven, but the existence of BNBs, which are attempted to be proven by dynamic light scattering techniques [1], is still open to debate; however, there are strong indications for their existence [19]. BNBs are generated using solvent replacement, temperature change, hydrodynamic cavitation, and electrolysis [4].

For practical application, BNBs should be stable, i.e., have long lifetimes. The stability mechanism has been widely discussed in the literature [21–24]. In the hydrodynamic approach, taking into account the possible coalescence of neighboring BNBs, it was found that gases dissolved in the electrolyte inhibit the coalescence of BNBs, taking into account the reduction of the force of attraction between them. Similarly, but to a lesser extent, the surface tension gradient at bubble fusion (Gibbs–Marangoni effect) has an effect [21, 22]. The influence of ion hydration has also been noted [23]. The electrostatic approach is more widespread [1, 2, 5, 7, 8, 10, 11,1 3,1 6, 17, 20, 24–31], in which it is usually assumed that the stability of the BNB is ensured by the fact that the Coulomb pressure P_0 and the Laplace pressure P_L acting on the boundary of the BNB balance each other. The gas pressure inside the BNB is not taken into account, since it is by orders of magnitude smaller than the pressures P_C and P_L in the whole range of BNB sizes. It is clear that the stability of BNBs has a thermodynamic character and cannot be considered in isolation from their homogeneous generation, fission, and coalescence. In [28], the regions of charge and radius values where BNBs are stable, coalesce and fission were determined. In [29] the thermodynamic analysis of their homogeneous generation BNBs in supersaturated aqueous solution was carried out, the minimum work of formation and the radius of critical nuclei were calculated, and the conditions of BNBs stability were derived. It was shown in [30] that homogeneous generation of BNBs is due to the minimization of the Gibbs energy of the gas-liquid disperse system. Note that the model of a single charged bubble in a homogeneous liquid dielectric was usually used, which was refined in [31] by the hypothesis of the presence of a hydrate shell of BNB with a thickness $\Delta \sim 1$ nm and relative permittivity (RP) of water $\varepsilon = 3$ with a tangent orientation of dipoles. This was explained by the conservation of hydrogen bonding energy of water dipoles in the "tangential" shell structure compared to the energy of their polarization orientation in the previously assumed "radial" structure. The basis for this hypothesis was the known results of the molecular dynamics method [34] where it is said that molecules tend to keep the maximum number of hydrogen bonds, "packing forces" create a dense layer in contact with the surface. The directions of dipole moments $\mathbf{p}$ are aligned in the near-surface layer in the tangential direction. Moreover, the orientation of the dipole polarization vector is determined by hydrogen bonding rather than the electric field. In addition, scanning dielectric microscopy of the local water capacitance between atomically flat walls [32] revealed an interfacial $\boldsymbol{\Delta}$-layer ($\Delta \sim 1$ nm, $\varepsilon = 3$) near the charged electrode. It is known from [33] that near the interface, water is ordered in layers extending several molecular diameters from the interface. It was also shown in [35] that water exhibits a clear layered structure near all surfaces, regardless of their hydrophilicity within $\Delta \approx 1$ nm from the electrode. Since the law of energy conservation is universal and does not depend on the shape of the surface near which it is realized, its effect at extended charged surfaces [32–35] can be fairly applied to the spherical BNBs surface [31]. Probably, an indirect experimental confirmation of the presence of an electrically "dead" shell of the BNBs can be considered as their increased stability. The calculations in [36] of the van der Waals forces at the registered stable bubbles lead to the conclusion about the peculiarity of interfacial properties at the BNB boundary, which also serves as an indirect support of the conclusion [31] about the presence of the BNB hydrate shell. The refined model was used in [37] in analyzing the characteristics of stable BNB, where the conditions for the existence of its Stern layer were found. In [38], an increase in stability is reported due to the reduction of the BNB capacitance by the Δ-layer.

As noted above, BNB stability is usually considered to be ensured by the balance of Coulomb pressure at the BNB boundary (hereinafter referred to as BNB pressure):

$$P_{\mathrm{C}}(r_0) = \frac{{q_0}^2}{32\pi^2\varepsilon_0\varepsilon {r_0}^4} \qquad (1)$$

and Laplace pressure:

$$P_{\mathrm{L}}(r_0) = 2\alpha / r_0, \qquad (2)$$

where r_0 and q_0 are the radius and charge of BNB, respectively; $\varepsilon_0 = 8.85 \cdot 10^{-12}\,\frac{\mathrm{F}}{\mathrm{m}}$ is the dielectric constant of vacuum; $\alpha = 0.072$ N/m is the surface tension coefficient of water.

1. PROBLEM STATEMENT

Note that formula (1) is valid for a homogeneous dielectric medium. However, as noted above, a hydrate Δ-layer ($\Delta \approx 1$ nm, $\varepsilon_1 \approx 3$) of polar water molecules with a tangent orientation of the polarization vector is formed at the boundary of the BNB. Outside the Δ-layer, the RP of water returns to the usual value of $\varepsilon_2 \approx 80$ (Fig. 1). Therefore, let us refine the formula (1) taking into account the influence of the hydrate Δ-layer and the concentration of dissolved c salts.

2. ANALYZING THE STRUCTURE OF NANOBUBBLES IN WATER

A spherical system with a double-layer dielectric is similar to two capacitors of capacitance C_1 and C_2 [39]. For the BNB with radius r_0, the inner capacitor has the shell radii r_0 and $r_0+\Delta$, RP $\varepsilon_1 \approx 3$, and the outer capacitor parameters are $(r_0+\Delta)$, $(r_0+\Delta+L)$ and RP $\varepsilon_2 \approx 80$, where: $L = \sqrt{\varepsilon_0\varepsilon_2 k_{\mathrm{B}}T / 2e^2 N_{\mathrm{A}} c}$ – Debye length, m; $k_{\mathrm{B}} = 1.38 \cdot 10^{-23}$ J/K is the Boltzmann constant; $N_{\mathrm{A}} = 6 \cdot 10^{23}$ mol^{-1} is Avogadro's number; $T = 293$ K is the temperature, c is the concentration of the salt solution, mol/m^3; $e = 1.6 \cdot 10^{-19}$ C is the elementary charge.

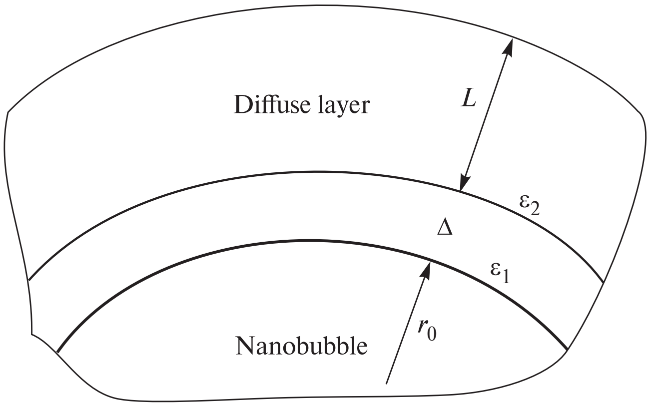

Fig. 1. Structure of the shell of the bulk nanobubble.

Capacitor capacities, $C_1 = 4\pi\varepsilon_0\varepsilon_1\left(\frac{1}{r_0} - \frac{1}{r_0 + \Delta}\right)^{-1}$, $C_2 = 4\pi\varepsilon_0\varepsilon_2\left(\frac{1}{r_0 + \Delta} - \frac{1}{r_0 + \Delta + L}\right)^{-1}$, respectively. The total capacitance is determined by the well-known formula:

$$C(r_0) = 4\pi\varepsilon_0\left[\begin{array}{l}\frac{1}{\varepsilon_1}\left(\frac{1}{r_0} - \frac{1}{r_0 + \Delta}\right) + \\ + \frac{1}{\varepsilon_2}\left(\frac{1}{r_0 + \Delta} - \frac{1}{r_0 + \Delta + L}\right)\end{array}\right]^{-1}. \quad (3)$$

Let's determine the electrostatic pressure of the BNB $P_C(r_0)$ in a liquid dielectric ($\varepsilon_2 = 80$) without Δ-layer and the pressure $P(r_0)$ for the BNB with Δ-layer. The energy of each of the BNB variants is $U = q_0^2/2C$. The pressure for the BNB at $\Delta = 0$ is [40]:

$$P_C(r_0) = -\frac{\partial U}{\partial r_0}\frac{1}{4\pi r_0^2} = -\frac{q_0^2}{8\pi r_0^2}\frac{\partial}{\partial r_0}\left(\frac{1}{C}\right) = \\ = \frac{q_0^2(L + 2r_0)L}{32\pi^2\varepsilon_0\varepsilon_2 r_0^4(L + r_0)^2}, \quad (4)$$

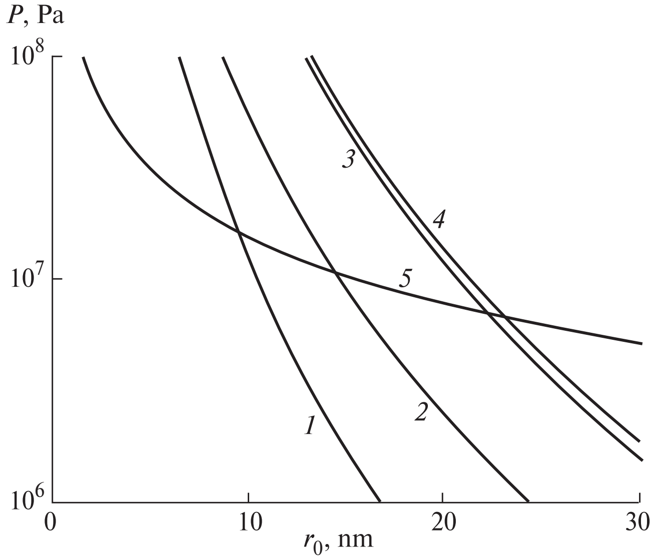

Fig. 2. Plots of dependence of pressures $P_i(r_0)$ at the nanobubble boundary ($q_0 = 4\cdot 10^{-16}$ C) as a function of its radius: curves *1*, *2* – pressures $P_1(r_0)$ and $P_2(r_0)$ for BNB without Δ-layer in salt (c = 100 mol/m^3) and pure (c = 1 mol/m^3), water, respectively; curves *3*, *4* – pressures $P_3(r_0)$ and $P_4(r_0)$, for BNB with Δ-layer in salt (c = 100 mol/m^3) and pure (c = 1 mol/m^3) water, respectively; curve *5* – Laplace pressure $P_5(r_0) = P_L(r_0)$ according to formula (2).

where the capacitance $C = 4\pi\varepsilon_0\varepsilon_2 r_0(1 + r_0 / L)$. Similarly, taking into account (3), we find for BNB with Δ-layer:

$$P(r_0) = \frac{q_0^2}{32\pi^2\varepsilon_0 r_0^2}\times \\ \times\left[\frac{\Delta(2r_0 + \Delta)}{\varepsilon_1(r_0 + \Delta)^2 r_0^2} + \frac{L(2r_0 + 2\Delta + L)}{\varepsilon_2(r_0 + \Delta)^2(r_0 + \Delta + L)^2}\right], \quad (5)$$

which refines (1) taking into account the Debye length L and Δ-layer. As one would expect, formulas (4) and (5) at $\Delta = 0$, $L \to \infty$ come to the form (1). Note that the Debye length $L = 9.6$ nm in pure water and $L = 0.96$ nm in salt water.

Fig. 2 shows the dependences of pressure $P_i(r_0)$ on the BNB radius according to formulas (4) and (5) in pure (c = 1 mol/m^3) and salt (c = 100 mol/m^3) water, as well as the Laplace pressure $P_L(r_0)$, where the pressure index $P_i(r_0)$ corresponds to the number of the curve in the graph of Fig. 2. The increase in Coulomb pressure due to Δ-layer of BNB can be seen, which increases its stability and is particularly strong in salt water. Note that when $P_i(r_0) > P_L(r_0)$, it is the charge that makes the BNB stable, especially in its smaller size region. This points to erroneous conclusion [41] about the unattainability of BNB stability by fulfilling the condition $P(r_0) = P_L(r_0)$.

Let us compare the effectiveness of the influence of Δ-layer in salt and pure water by determining the pressure ratio $k_0(r_0) = P_4(r_0)/P_2(r_0)$ in pure and $k_c(r_0) = P_3(r_0)/P_1(r_0)$ in salt water for BNB with and without Δ-layer, which is shown in Fig. 3.

Let us analyze the obtained results. The increase in pressure $P(r_0)$ at the BNB with Δ-layer is due to the fact that the capacitance $C(r_0)$ of the series connected capacitors C_1 and C_2 is determined by the smallest of these values – the capacitance C_1 of the BNB Δ-layer, taking into account $\varepsilon_1 \ll \varepsilon_2$. This, according to (5), increases $P(r_0)$. It can also be seen in Fig. 2 that as the radius of the BNB increases, its pressure $P(r_0)$ becomes lower than the Laplace pressure $P_L(r_0)$, since $P_L(r_0)/P(r_0) \sim r_0^3$, subject to (1), (2). In addition, the size of the stable BNB due to Δ-layer increases with increasing its radius, but decreases with increasing salinity of c solution. This can be explained by the decrease in the Debye length L and the capacity of the BNB, considering (5). It can also be seen that Δ-layer weakens the effect of salinity on pressure and on BNB stability. This is due to the fact that the influence of the capacitance C_2 is suppressed by the first summand in square brackets (5), which is relatively large for the above reason $\varepsilon_1 \ll \varepsilon_2$.

Fig. 3 shows that in salt water Δ-layer increases the pressure of BNB almost 30 times, and in fresh water – from 10 to 4 times in the range of BNB sizes of 5–100 nm. This is also explained by the competition of the above-mentioned summands of formula (5). Moreover, in salt water, the summand dependent on L is so small that its change almost does not affect the value of $k_c(r_0)$, in contrast to the dependence of $k_0(r_0)$ in pure water. It is

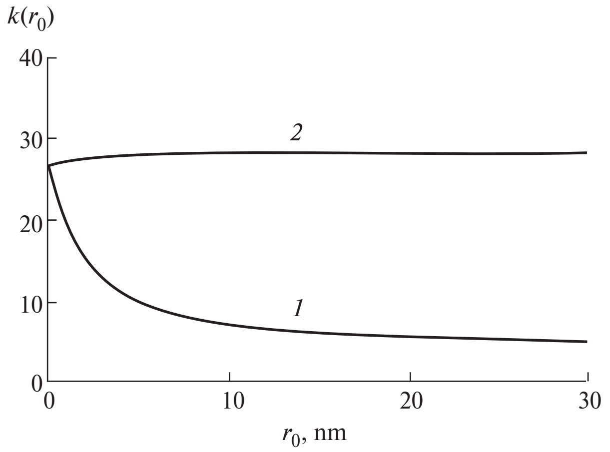

Fig. 3. Graph of dependence of the ratio $P(r_0)/P_C(r_0)$ on the BNB radius with and without Δ-layer: curve *1* – pressure ratio $k_0(r_0) = P_4(r_0)/P_2(r_0)$ in pure water ($c = 1$ mol/m^3); Curve *2* – pressure ratio $k_c(r_0) = P_3(r_0)/P_1(r_0)$ in salt water ($c = 100$ mol/m^3).

also important to note that the plots of Fig. 2 depend on the value of the BNB charge q_0, while the plots of Fig. 3 do not, since q_0 is a factor in expressions (4) and (5).

CONCLUSION

— The stability of the BNB is provided by Δ-layer with an RP of $\varepsilon_1 = 3$;

— the multiplicity of BNB pressure rise due to Δ-layer is independent of its charge;

— the BNB pressure due to salinity drops markedly for BNB without Δ-layer and slightly for BNB with Δ-layer.

FUNDING

This work was supported by the Ministry of Science and Higher Education of the Russian Federation (state task No. 121112200122-7).

ETHICS DECLARATION

There are no human or animal studies in this paper.

CONFLICT OF INTERESTS

The author declares that he has no conflict of interests.

REFERENCES

1. *Tan B.H., An H., Ohl C.-D.* How bulk nanobubbles might survive // Physical Review Letters. 2020. Vol. 124. P. 134503. https://doi.org/10.1103/PhysRevLett.124.134503
2. *Bunkin N.F., Shkirin A.F.* Investigation of the babston-cluster structure of water and aqueous electrolyte solutions by laser diagnostic methods // Trudy IOFAN im. A.M. Prokhorova. 2013. Vol. 69. Pp. 3–57.
3. *Favvas E.P., Kyzas G.Z., Efthimiadou E.K., Mitropoulos A.Ch.* Bulk nanobubbles, generation methods and potential applications// *Current Opinion in Colloid & Interface Science*. 2020. Vol. 54. P. 101455. https://doi.org/10.1016/j.cocis.2021.101455
4. *Nazary S., Hassanzadeh A., He Y., Khoshdast H., Kowalczuk P.B.* Recent developments in generation, detection and application of nanobubbles in flotation // Minerals. 2022. Vol. 12. No. 4. P. 462. https://doi.org/10.3390/min12040462
5. *Wang H., Varghese J., Pilon L.* Simulation of electric double layer capacitors with mesoporous electrodes: Effects of morphology and electrolyte permittivity // Electrochim. Acta. 2011. Vol. 56. No. 17. Pp. 6189–6197. https://doi.org/10.1016/j.electacta.2011.03.140
6. *Singh S.B., Shukla N., Cho C.H., Kim B.S., Park M.H., Kim K.* Effect and application of micro- and nanobubbles in water purification // Toxicology and Environmental Health Sciences. 2021. Vol. 13. Pp. 9–16. https://doi.org/10.1007/s13530-021-00081-x
7. *Meegoda J.N, Hewage S.A., Batagoda J.H.* Stability of nanobubbles // Environmental Engineering Science. 2018. Vol. 35. No. 11. Pp. 1216–1227. http:// doi.org/10.1089/ees.2018.0203
8. *Meegoda J.N., Hewage S.A., Batagoda J.H.* Application of the diffused double layer theory to nanobubbles // Langmuir 2019. Vol. 35. No. 37. Pp. 12100–12112. https://doi.org/10.1021/acs.langmuir.9b01443
9. *Kelsall G.H., Tang S., Yurdakult S., Smith A.L.* Electrophoretic behaviour of bubbles in aqueous electrolytes // J. Chem. SOC., Faraday Trans. 1996. Vol. 92. No. 20. Pp. 3887–3893. https://doi.org/10.1039/FT9969203887
10. *Chan D.Y.C., Mitchell D.J.* The free energy of an electrical double layer // Journal of Colloid and Interface Science. 1983. Vol. 95. No. 1. Pp. 193–197.
11. *Bunkin N.F., Bunkin F.V.* Bastion structure of water and aqueous electrolyte solutions // Uspekhi fizicheskikh nauk. 2016. Vol. 186. No. 9. Pp. 933–952. https://doi.org/10.3367/UFNr.2016.05.037796
12. *Hewage S.A., Kewalramani J., Meegoda J.N.* Stability of nanobubbles in different salts solutions // Colloids and Surfaces A: Physicochemical and Engineering Aspects. 2021. Vol. 609. P. 125669. https://doi.org/10.1016/j.colsurfa.2020.125669
13. *Lopez-Garsia J.J., Moya A.A., Horno J., Delgado A., Lez-Caballero F.G.* A network model of the electrical double layer around a colloid particle // Journal of colloid and interface science. 1996. Vol. 183. No. 1. Pp. 124–130. https://doi.org/10.1006/jcis.1996.0525
14. *Jadhav A.J., Barigou M.* On the clustering of bulk nanobubbles and their colloidal stability // Journal of Colloid and Interface Science. 2021. Vol. 601. Pp. 816–824. https://doi.org/10.1016/j.jcis.2021.05.154
15. *Ma X., Li M., Pfeiffer P.* Ion adsorption stabilizes bulk nanobubbles // J. Colloid Interfac. Sci. 2022. Vol. 606. Pp. 1380–1394. https://doi.org/10.1016/j.jcis.2021.08.101

16. *Nirmalkar N., Pacek A.W., Barigou M.* On the existence and stability of bulk nanobubbles // Langmuir. 2018. Vol. 34. No. 37. Pp. 10964–10973. https://doi.org/10.1021/acs.langmuir.8b01163
17. *Zhang H., Guo Z., Zhang X.* Surface enrichment of ions leads to the stability of bulk nanobubbles // Soft Matter. 2020. Vol. 16. Pp. 5470–5477. https://doi.org/10.1039/d0sm00116c
18. *Temesgen T., Bui T.T., Han M., Kim T., Park H.* Micro and nanobubble technologies as a new horizon for watertreatment techniques: A review // Advances in Colloid and Interface Science. 2017. Vol. 246. Pp. 40–51. https://doi.org/10.1016/j.cis.2017.06.011
19. *Kyzas G.Z., Mitropoulos A.C.* From bubbles to nanobubbles // *Nanomaterials*. 2021. Vol. 11. No. 10. P. 2592. https://doi.org/10.3390/nano11102592
20. *Levin Yu.K.* Mechanism of stability of nanobubbles in water // Izv. vuzov. Fizika. 2024. Vol. 67. No. 10. Pp. 58–61. https://doi.org/10.17223/00213411/67/10/7
21. *Weissenborn P.K., Pugh R.J.* Surface tension of aqueous solutions of electrolytes: Relations with ion hydration. Oxygen solubility, and bubble coalescence// J. Colloid Interface Science. 1996. Vol. 184. No. 2. Pp. 550–563. https://doi.org/10.1006/jcis.1996.0651
22. *Craig V.S.J., Ninham B.W., Pashley R.M.* The effect of electrolytes on bubble coalescence in water // J. Phys. Chem. 1993. Vol. 97. No. 39. Pp. 10192–10197. https://doi.org/10.1021/j100141a047
23. *Tsao H.K., Koch D.L.* Collisions of slightly deformable, high Reynolds number bubbles with shortrange repulsive forces // Physics of Fluids. 1994. Vol. 6. No. 8. Pp. 2591–2605. https://doi.org/10.1063/1.868149
24. *Koshoridze S.I., Levin Yu.K.* Thermodynamic analysis of the stability of nanobubbles in water // Nanoscience and Technology: An International Journal. 2019. Vol. 10. No. 1. Pp. 21–27. https://doi.org/10.1615/NanoSciTechnolIntJ.2018028801
25. *Calgaroto S., Willberg K.Q., Rubio J.* On the nanobubbles interfacial properties and future applications in flotation // Minerals Engineering. 2014. Vol. 60. Pp. 33–40. https://doi.org/10.1016/j.mineng.2014.02.002
26. *Koshoridze S.I., Levin Yu.K.* Comment on “Can bulk nanobubbles be stabilized by electrostatic interaction?” by S. Wang, L. Zhou and Y. Gao, Phys. Chem. Chem. Phys. 2021. 23. 16501 // Phys. Chem. Chem. Phys. 2022. Vol. 24. Pp. 10622–10625. https://doi.org/10.1039/D1CP04406K
27. *Joly L., Ybert C., Trizac E., Bocquet L.* Hydrodynamics within the electric double layer on slipping surfaces // Phys. Rev. Lett. 2004. Vol. 93. P. 257805. https://doi.org/10.1103/PhysRevLett.93.257805
28. *Boshenyatov B.V., Koshoridze S.I., Levin Yu.K.* On the stability of nanobubbles in water // Izv. vuzov. Fizika. 2018. Vol. 61. No. 10. Pp. 149–155.
29. *Koshoridze S.I., Levin Yu.K.* Conditions of nucleation and stability of bulk nanobubbles // Izv. vuzov. Fizika. 2022. No. 1. Pp. 89–95. https://doi.org/10.17223/00213411/65/1/89c
30. *Koshoridze S.I., Levin Yu.K.* Stability of charged nanobubbles in water // Pis’ma v ZhTF. 2019. Vol. 45. Pp. 61–62. https://doi.org/10.21883/PJTF.2019.01.47161.17521
31. *Levin Yu.K.* Stability conditions of the Stern layer of bulk nanobubbles in water // Izv. vuzov. Fizika 2022. Vol. 65. No. 12. Pp. 55–59. https://doi.org/10.17223/00213411/65/12/55
32. *Fumagalli L., Esfandiar A., Fabregas R., Hu S., Ares P., Janardanan A., Yang Q., Radha B., Taniguchi T., Watanabe K., Gomila G., Novoselov K.S., Geim A.K.* Anomalously low dielectric constant of confined water // Science. 2018. Vol. 360. Pp. 1339–1342. https://doi.org/10.1126/science.aat4191
33. *Toney M.F., Howard J.N., Richer J., Gary L., Gordon J.G., Melroy O.R., Wiesler D.G.; Yee D., Sorensen L.B.* Voltage-dependent ordering of water molecules at an electrode-electrolyte interface // Nature. 1994. Vol. 368. Pp. 444–446. https://doi.org/10.1038/368444a0
34. *Lee C.Y., McCammon J.A., Rossky P.J.* The structure of liquid water at an extended hydrophobic surface // J. Chem. Phys. 1984. Vol. 80. No. 9. Pp. 4448–4455. https://doi.org/10.1063/1.447226
35. *Velasco-Velez J -J., Wu C.H., Pascal T.A., Wan L.F., Guo J.A., Prendergast D., Salmeron M.* The structure of interfacial water on gold electrodes studied by x-ray absorption spectroscopy // Science. 2014. Vol. 346. Pp. 831–834. https://doi.org/10.1126/science.1259437
36. *Hewage S.A., Kewalramani J., Meegoda J.N.* Stability of nanobubbles in different salts solutions // Colloids and Surfaces. A: Physicochemical and Engineering Aspects. 2021. Vol. 609. P. 125669. https://doi.org/10.1016/j.colsurfa.2020.125669
37. *Levin Yu.K.* Characteristics of a double electric layer of volumetric nanobubbles in water // Colloid Journal. 2023. Vol. 85. No. 3. Pp. 350–354. https://doi.org/10.31857/S0023291223600220
38. *Koshoridze S.I.* The effect of the structure of the double electric layer on the stability of bulk nanobubbles // Inzhenernaya fizika. 2023. No. 7. Pp. 22–25. https://doi.org/10.25791/infizik.7.2023.1342
39. *Meledin G.V., Cherkasskiy V.S.* Electrodynamics in problems. Part.1 // NGU. 2009.
40. *Feinman R., Leyton R., Sands M.* The Feinman Lectures on Physics. Iss. 5. M.: Mir, 1966.
41. *Levin Yu.K.* A new concept of stability of nanobubbles in water // Proceedings of the 13th All-Russian Conference “Mechanics of composite materials and structures, complex and heterogeneous media”. 2023. (P. 208, part 1). M.: IPRIM RAS. https://doi.org/10.33113/conf.mkmk.ras.2023.28

COLLOID JOURNAL, 2025, Vol. 87, No. 1, pp. 37–47

RHEOLOGY OF STRUCTURED LIQUIDS. FLOW REGIMES AND RHEOLOGICAL EQUATIONS

© 2025 V. N. Matveenko[a], * and E. A. Kirsanov[b]

[a] *Lomonosov Moscow State University, Moscow, Russia*

[b] *State Social and Humanitarian University, Kolomna, Russia*

**e-mail: 13121946VNM@gmail.com*

Received September 03, 2024
Revised October 17, 2024
Accepted October 17, 2024

Abstract. A system of rheological equations is presented, obtained on the basis of structural-kinetic representations, which describes viscous and elastic properties of structured liquids, namely concentrated suspensions, emulsions, micellar solutions, solutions and polymer melts. The structural model equations hold for equilibrium steady-state flow and for equilibrium oscillating flow. The equations are suitable for approximating rheological curves $\tau(\dot{\gamma})$, $N_1(\dot{\gamma})$, $G''(\omega)$, $G'(\omega)$, at individual intervals of shear rate or oscillation frequency. Each such interval corresponds to a certain state of the structure. As an example, the results of approximation of shear viscosity curves for polymer solution, micellar solution and emulsion are given.

Keywords: *rheological equations, structural rheological model, equilibrium stationary flow, equilibrium oscillating flow*

DOI: 10.31857/S00232912250105e8

INTRODUCTION

At present, there are no generally accepted views on the problem of non-Newtonian flow. Types of flow in suspensions, emulsions, micellar solutions, polymer solutions and melts are considered separately. Many local models and rheological equations have been proposed for each type of these structured systems [1–4].

Two main classes of rheological models can be distinguished, which consider fluid media either as homogeneous, homogeneous, or as heterogeneous, possessing some structure. In the first case, the methods of theoretical rheology based on continuum mechanics are used. Some physical justification of such rheological models is provided by mechanical models composed of springs, dampers, dry friction elements (Maxwell, Kelvin–Voigt, etc.).

In the second case, models describing aggregates of particles or associations of macromolecules that move in a viscous medium are used. The hydrodynamic approach is based on the laws of flow of particles and aggregates with viscous fluid and on the consideration of hydrodynamic forces that break the aggregates. The kinetic approach is based on kinetic equations describing the processes of formation and destruction of particle aggregates in shear flow.

The current state of the problem of non-Newtonian flow is described in various monographs, e.g., [5–7]. We have proposed a structural rheological model [8, 9] that allows us to describe the rheological behavior of various disperse and polymeric systems under steady-state and oscillatory flow.

The model is obtained by modifying and combining the well-known models of Casson [10] and Cross [11] (see Appendix 1).

In this paper, rheological equations derived from a unified structural approach will be fully summarized for both steady-state and oscillatory flow. These rheological equations are suitable for describing both viscous and elastic properties. As an example of using the rheological equations of the structural model, we have approximated the flow curves of some disperse systems.

STRUCTURED LIQUIDS

The structural rheological model describes shear flow of structured systems under equilibrium flow conditions. Such flow, the characteristics of which do not depend on time, is called steady-state or stationary flow. The structure of a system is the organization of particles by means of physical or chemical bonds into a unified whole. Concentrated suspensions, emulsions, micellar solutions, polymer solutions and melts, liquid crystals can be called structured liquids because they have some structure and shear flow.

In concentrated suspensions, particles combine into aggregates during collisions. In the process of shear flow, an individual aggregate moves for some time as a whole, i.e. as an independent flow unit. Aggregates are capable of disintegrating spontaneously, e.g. due to thermal motion, or forced, e.g. due to hydrodynamic breaking forces. Under certain conditions, particles form aggregates during collisions in shear flow (shear induced structure).

Aggregates and individual particles are elements of the structure. If a unit volume contains $\tilde{N}$ particles, we denote the number of aggregated particles (included in all aggregates) as $\tilde{N}_2$, and the number of individual particles as $\tilde{N}_1$. In this way we can introduce an integral characteristic of a structured system, assuming that with increasing $\tilde{N}_2$ both the number of aggregates and their sizes increase.

In polymer melts and solutions, the role of particles is played by macromolecules, and the role of contacts is played by entanglements between macromolecules or direct interaction of chemical groups of neighboring macromolecules.

EQUATIONS OF THE STRUCTURAL RHEOLOGICAL MODEL

We can conditionally divide the full interval of shear velocities $\dot{\gamma}$ and the full interval of shear oscillation frequencies ω into four parts. In each separate interval there is a special structural state to which a certain flow regime corresponds. Measured rheological quantities: shear stress $\tau(\dot{\gamma})$, first normal stress difference $N_1(\dot{\gamma})$, loss modulus $G''(\omega)$, accumulation modulus $G'(\omega)$.

Here we briefly review the existing flow regimes, which are described in more detail in [9, 12–16]. Rheological curves $\tau(\dot{\gamma})$, $N_1(\dot{\gamma})$, $G''(\omega)$, $G'(\omega)$ can be conditionally divided into the following sections: low (II), high (III), very low (I), very high (IV) shear rates or oscillation frequencies.

Based on hydrodynamic considerations, a generalized flow equation [8, 9] was derived for the high shear rate interval (III) in the form:

$$\tau^{1/2} = \frac{\tau_c{}^{1/2}\dot{\gamma}^{1/2}}{\dot{\gamma}^{1/2} + \chi} + \eta_c{}^{1/2}\dot{\gamma}^{1/2}. \tag{1}$$

The shear viscosity can be written in the following form

$$\eta^{1/2} = \frac{\tau_c{}^{1/2}}{\dot{\gamma}^{1/2} + \chi} + \eta_c{}^{1/2}. \tag{2}$$

The physical meaning of the coefficients χ, $\tau_c^{1/2}$, $\eta_c^{1/2}$ is described in [8, 9], their values, in accordance with the hydrodynamic approach of Casson, have the following form:

$$\tau_c^{1/2} = \tau_{0c}^{1/2}\left[\left(\frac{1}{1-k_2\Phi}\right)^{A_2} - 1\right],$$

$$\eta_c^{1/2} = \eta_0^{1/2} \cdot \left[\frac{1}{1-k\Phi}\right]^{A}.$$

The coefficient χ reflects the compactness or friability of the aggregates and is zero if a continuous mesh of particles is formed.

Taking into account the presence of square roots in equation (2), let us write the equation for shear viscosity, according to the kinetic approach of Cross:

$$\eta^{1/2} = \eta_\infty^{1/2} + B\tilde{N}_2, \tag{3}$$

where the coefficient $\eta_\infty^{1/2}$ describes the viscosity of all individual single particles, B is some positive constant independent of the shear rate.

Using the kinetic approach, let us write down the kinetic equation of formation and destruction of particle aggregates:

$$\frac{d\tilde{N}_2}{dt} = \tilde{k}_2\tilde{N} - \tilde{k}_0\tilde{N}_2 - \tilde{k}_1\dot{\gamma}^{1/2}\tilde{N}_2 + \tilde{k}_3\dot{\gamma}^{1/2}\tilde{N}_1. \tag{4}$$

Equation (4) contains the following coefficients: $\tilde{k}_2$ – rate constant of aggregate formation at particle collisions; $\tilde{k}_0$ – rate constant of spontaneous destruction of aggregates, for example, as a result of thermal motion; $\tilde{k}_1$ – rate constant of aggregate destruction under the action of tensile hydrodynamic forces, $\tilde{k}_3$ – rate constant of formation of particle aggregates from single particles under the action of shear. This kinetic equation does not consider the interaction of aggregates of different sizes with each other, nor does it introduce a specific form of aggregate as a duplex as, for example, in [17]. The integral characteristics of the system, namely the total number of aggregated particles and the total number of particles in a unit volume, are used to describe the process of destruction/aggregate formation. A comparison of the proposed kinetic equation with other similar equations reviewed in [18] is given in Appendix 1.

At the interval of high shear rates (III), shear-induced contact failure occurs, which leads to a decrease in the number of aggregated particles $\tilde{N}_2$ under the condition ($\tilde{k}_1 > 0$, $\tilde{k}_3 = 0$). The equation of state under equilibrium conditions $d\tilde{N}_2/dt = 0$ takes the form:

$$\frac{\tilde{N}_2}{\tilde{N}} = \frac{\tilde{k}_2}{\tilde{k}_1\dot{\gamma}^{1/2} + \tilde{k}_0}. \tag{5}$$

Substituting (5) into (3) we obtain a rheological equation similar to the generalized flow equation in the form (2):

$$\eta^{1/2} = \frac{B\tilde{N}\tilde{k}_2 / \tilde{k}_1}{\dot{\gamma}^{1/2} + \tilde{k}_0 / \tilde{k}_1} + \eta_\infty^{1/2}. \tag{6}$$

Thus, the coefficients of the generalized flow equation (1) or (2) can be expressed through the rate constants of the kinetic equation (4): $\tau_c^{1/2} = B\tilde{N}\tilde{k}_2 / \tilde{k}_1$, $\chi = \tilde{k}_0 / \tilde{k}_1$, $\eta_\infty^{1/2} = \eta_c^{1/2}$.

At interval (III), the shear viscosity decreases naturally with increasing shear rate, with the value of the structural viscosity $\tau_c^{1/2} / \chi$ or the value of the aggregation coefficient $\tau_c^{1/2}$ being much larger than the value of the coefficient $\eta_c^{1/2}$.

If shear results in strong contacts between particles under the condition ($\tilde{k}_1 > 0$, $\tilde{k}_3 > 0$), it is necessary to use equations (3) and (4) containing all four positive coefficients. Then one can obtain [9] an approximate expression for shear viscosity under the condition $\dot{\gamma} > \left(\dfrac{\tilde{k}_0}{\tilde{k}_3 + \tilde{k}_1}\right)^2$:

$$\eta^{1/2} \approx \left(\eta_\infty^{1/2} + B\tilde{N}\frac{\tilde{k}_3}{\tilde{k}_3 + \tilde{k}_1}\right) - B\tilde{N}\frac{(\tilde{k}_0 - \tilde{k}_2)}{(\tilde{k}_3 + \tilde{k}_1)\dot{\gamma}^{1/2}}. \quad (7)$$

Hence the rheological equation of the form

$$\tau^{1/2} = \eta_{cv}^{1/2}\dot{\gamma}^{1/2} - \tau_{cv}^{1/2}, \quad (8)$$

whose coefficients are equal to:

$$\eta_{cv}^{1/2} = \eta_\infty^{1/2} + B\tilde{N}\tilde{k}_3 / (\tilde{k}_3 + \tilde{k}_1);$$
$$\tau_{cv}^{1/2} = B\tilde{N}(\tilde{k}_0 - \tilde{k}_2) / (\tilde{k}_3 + \tilde{k}_1).$$

The coefficient $\tau_{cv}^{1/2}$ is positive if $\tilde{k}_0 > \tilde{k}_2$, and negative if $\tilde{k}_0 < \tilde{k}_2$. Therefore, three types of rheological behavior are possible in the interval (II). In the first case, the viscosity increases with increasing shear rate (shear solidification phenomenon). In the second case, the viscosity decreases with increasing shear rate, with the coefficient $\tau_{cv}^{1/2}$ being less than or comparable in magnitude to the coefficient $\eta_{cv}^{1/2}$. In the third case, the coefficient $\tau_{cv}^{1/2}$ is close to zero under the condition $\tilde{k}_0 \approx \tilde{k}_2$, then the rheological behavior is similar to "Newtonian" flow with an almost constant value of shear viscosity η_{cv}.

In the interval (IV) of very high shear rates, a significant decrease in shear stress τ is observed compared to the values calculated from equation (1). The value of τ decreases with increasing $\dot{\gamma}$ or remains constant over a large range of shear rates. This phenomenon is referred to as flow "stall"; it is possibly related to shear delamination of the sample or to a change in the flow velocity profile. In the interval (I) of very low shear rates, flow with constant shear viscosity is observed, possibly because the shear magnitude is not large enough to break existing particle aggregates or to create new strong contacts. Thus, the structure of the system remains constant. This "Newtonian" flow regime is usually observed at low velocities.

Separation of flow curves into separate intervals with different flow regimes can be done using root coordinates ($\tau^{1/2} - \dot{\gamma}^{1/2}$), where rectilinear dependencies are clearly visible ($\tau^{1/2} \sim \dot{\gamma}^{1/2}$). Each section has a separate flow regime with its own values of the coefficients of the rheological equation. Therefore, it is impossible to describe the entire range of measurements with one rheological equation.

Note that individual particles can be solids, droplets, micelles, macromolecules. The role of aggregates of particles can be played by groupings of micelles, associations of macromolecules linked by entanglements.

The reasoning presented above can be applied to explain the elastic properties of matter under equilibrium shear flow. The elastic behavior at steady-state flow is described by the first normal stress difference $N_1 = \tau_{11} - \tau_{22}$. Let us introduce an expression for shear elasticity of the form $\eta_{ST} = N_1 / \dot{\gamma}$. Let us write the equation for shear elasticity in the form:

$$\eta_{ST}^{1/2} = n_\infty + B\tilde{N}_2. \quad (9)$$

If there are no aggregates, the shear elasticity is provided only by the elasticity of individual particles, i.e. it is related to the coefficient n_∞.

Let us assume that the number of particles forming "elastic" aggregates is equal to $\tilde{N}_2$. Let us write the kinetic equation of destruction and formation of "elastic" aggregates in the form similar to (4):

$$\frac{d\tilde{N}_2}{dt} = k_2\tilde{N} - k_0\tilde{N}_2 - k_1\dot{\gamma}^{1/2}\tilde{N}_2 + k_3\dot{\gamma}^{1/2}\tilde{N}_1. \quad (10)$$

The meaning of the rate constants remains the same, but their magnitude changes. Similar previous considerations lead to the rheological equation for the interval (III) of high velocities:

$$N_1^{1/2} = \frac{n_{ST}}{\dot{\gamma}^{1/2} + \chi_{ST}}\dot{\gamma}^{1/2} + n_\infty\dot{\gamma}^{1/2}, \quad (11)$$

where $\chi_{ST} = k_0 / k_1$; $n_{ST} = B\tilde{N}k_2 / k_1$.

For the interval (II) of low shear rates, we obtain the equation:

$$N_1^{1/2} = n_0\dot{\gamma}^{1/2} - \Delta N_1^{1/2}, \quad (12)$$

where
$$n_0 = n_\infty + B\tilde{N}\frac{k_3}{k_3 + k_1}; \ \Delta N_1^{1/2} = B\tilde{N}(k_0 - k_2) / (k_3 + k_1).$$

The coefficient $\Delta N_1^{1/2}$ is positive if $k_0 > k_2$, and negative if $k_0 < k_2$.

At the interval of very high shear rates, no anomalies similar to "stall" were observed on the curves $N_1(\dot{\gamma})$, considered by us [16].

In the interval (I) of very low shear rates, a power-law dependence of the following form is observed

$$N_1 \approx n_{00}\dot{\gamma}^{n}, \quad (13)$$

where $n \approx 2$. This kind of dependence does not follow from the mechanism of formation/destruction of particle aggregates. The structure of the system should probably be considered unchanged over the interval (I), and the elastic response should be attributed to the reaction of the entire system of bound particles. It is important to note that the boundaries of the flow regimes found for the dependence $\tau(\dot{\gamma})$ and for the dependence $N_1(\dot{\gamma})$ in the same structured fluid do not coincide completely.

We consider oscillating shear flow [9] as a type of shear flow whose magnitude and direction change according to a harmonic law. The amplitude of the shear velocity ($\gamma_0\,\omega$) is some analog of the shear velocity $\dot{\gamma}$: $\dot{\gamma} = k_{\mathrm{DIS}}\,\omega$, where k_{DIS} is the displacement factor. The model describing the dynamic moduli $G''(\omega)$ and $G'(\omega)$, is completely analogous to the model developed for steady-state flow [9]. The rheological equation describing viscous properties for the high frequency interval (III) has the following form:

$$G''^{1/2} = \frac{g'\,\omega^{1/2}}{\omega^{1/2} + \chi'} + \eta_{\infty}'^{\,1/2}\omega^{1/2}. \tag{14}$$

The aggregation coefficient g' indicates the degree of particle aggregation or the strength of macromolecule entanglements, the compactness coefficient χ' indicates the tendency to form loose aggregates of particles or associates of macromolecules, the ultimate viscosity coefficient $\eta_{\infty}'^{1/2}$ describes the viscosity resulting from the streamline of individual particles or macromolecules. The values of the coefficients present in equation (14) are: $\chi' = k_0' / k_1'$; $g' = B\,\tilde{N}\,k_2' / k_1'$.

The rheological equation for the low frequency interval (II) is as follows:

$$G''^{1/2} = g_0'\omega^{1/2} - \Delta G''^{1/2}, \tag{15}$$

where $g_0' = \eta_{\infty}'^{1/2} + B\tilde{N}k_3' / (k_3' + k_1')$;
$\Delta G''^{1/2} = B\tilde{N}\,(k_0' - k_2') / (k_3' + k_1')$.

The coefficient $\Delta G''^{1/2}$ is positive if $k_0' > k_2'$, and negative if $k_0 < k_2$. If $\tilde{k}_0 \approx \tilde{k}_2$, the rheological behavior is similar to “Newtonian” with a nearly constant value of dynamic viscosity η'.

Quite similarly, we obtain the equations describing the elastic properties:

$$G'^{1/2} = \frac{g''\,\omega^{1/2}}{\omega^{1/2} + \chi''} + \eta_{\infty}''^{1/2}\omega^{1/2}, \tag{16}$$

where $\chi'' = k_0'' / k_1''$; $g'' = B\,\tilde{N}\,k_2'' / k_1''$ and

$$G'^{1/2} = g_0''\omega^{1/2} - \Delta G'^{1/2}, \tag{17}$$

where $g_0'' = \eta_{\infty}''^{1/2} + B\tilde{N}k_3'' / (k_3'' + k_1'')$;
$\Delta G'^{1/2} = B\tilde{N}\,(k_0'' - k_2'') / (k_3'' + k_1'')$.

The coefficient $\Delta G'^{1/2}$ is positive if $k_0'' > k_2''$, and negative if $k_0'' < k_2''$. The physical meaning of these rate constants is the same as described earlier in the case of steady-state flow.

At very low frequencies on the interval (I) there is a power-law dependence

$$G'^{1/2} = g_{00}''\,\omega^{\mathrm{n}/2}, \tag{18}$$

where $n \approx 2$. It can be assumed that at this frequency interval the structure of the system does not change with increasing frequency. Then the frequency dependence (18) is due to the response of the entire elastic entanglement mesh to the action of oscillating shear flow.

At the interval (IV), an anomalous decrease of the dynamical moduli G'' and G', is observed, and their value can even decrease with increasing frequency. We will call this phenomenon the “stall” of the oscillating flow or the “stall” of the moduli G'' and G'.

Examples of analyzing the frequency dependences of the loss modulus G'' and accumulation modulus G' from the viewpoint of the structural model are given in [13–15]. Here, some rheological curves obtained for steady-state flow of structured fluids of different nature will be shown and interpreted.

EXAMPLES OF STEADY-STATE FLOW REGIMES. VISCOSITY–STRUCTURE RELATIONSHIP

In [19], the viscosity curve of polymer aqueous solution of polyethylene oxide (PEO) is given, which has a section (II) of shear solidification at low shear rates ($\dot{\gamma} \leq 0.1$ s^{-1}). The experimental data are shown in Table 2 (Appendix 2); the viscosity curve with approximation results is shown in Fig. 1. Shear solidification at low velocities was attempted by the authors [19] to be explained by a special intermolecular interaction. However, the uncharged, flexible and hydrophilic PEO chains are hardly capable of strong intermolecular interaction, although the formation of dimers is quite possible.

Plot (II) in Fig. 1 corresponds to the equilibrium flow, during which the processes of entanglement formation and destruction due to shear occur, but the formation process prevails ($\tilde{k}_1 > 0$, $\tilde{k}_3 > 0$, $\tilde{k}_0 > \tilde{k}_2$). Plot (III) corresponds to equilibrium flow, in which shear entanglement formation does not occur ($\tilde{k}_1 > 0$, $\tilde{k}_3 = 0$) and the process of entanglement destruction predominates.

At plot (IV), there is an abnormal decrease in viscosity, which gradually approaches the dependence $\eta \sim 1/\dot{\gamma}$ (dashed line in Fig. 1). Such rheological behavior is called flow stall.

Fig. 2 shows the results of approximation by equations (1) and (8) in root coordinate plots.

According to the structural rheological model [9], the coefficient $\eta_c^{1/2}$ is the root of the minimum limiting viscosity, i.e., the viscosity of the non-aggregated system. This viscosity arises from the movement of individual macromolecules in aqueous solution and is quite small compared to the zero viscosity of a polymer solution with entanglements, which is described by the coefficient $\eta^{1/2}(0)$.

The coefficients of equation (8) are equal:

$$\eta_{cv}^{1/2} = \eta_\infty^{1/2} + B\tilde{N}\tilde{k}_3 \,/\, (\tilde{k}_3 + \tilde{k}_1), \qquad (19)$$

$$\tau_{cv}^{1/2} = B\tilde{N}\,(\tilde{k}_0 - \tilde{k}_2) \,/\, (\tilde{k}_3 + \tilde{k}_1). \qquad (20)$$

It follows from equation (19) that $\eta_{cv}^{1/2} > \eta_\infty^{1/2}$; the coefficient $\eta_{cv}^{1/2}$ can be comparable in magnitude to the coefficient $\eta^{1/2}(0)$. It follows from equation (20) that the value of $\tau_{cv}^{1/2}$ can be negative, positive and close to zero depending on the relationship between the rate constants $\tilde{k}_0$ and $\tilde{k}_2$. These conclusions are confirmed by comparing the magnitudes of the coefficients in Table 1.

In [20], the rheological behavior of aqueous micellar solutions was considered. The cationic compound cetyltrimethylammonium bromide (CTAB) was used as a surface active agent, and the organic salt sodium salicylate (NaSal) was used as an additive. In such systems, cylindrical or worm-like micelles are formed. Shear solidification in micellar solutions is attributed to the formation of shear induced structure (SIS).

The experimental data are shown in Table 3 (Appendix 2), the viscosity curve with approximation results is shown in Fig. 3.

The graph (Fig. 3) shows three sections of the viscosity curve with three different flow regimes. At very low shear rates, the Newtonian flow regime is observed (plot I). Since the viscosity does not change, it can be assumed that the structure of the system also remains constant. Since the Newtonian viscosity η_N is less than the maximum viscosity but greater than the minimum viscosity present in the plot, it can be assumed that the constant structure at very low velocities contains both individual micelles and small micelle associations.

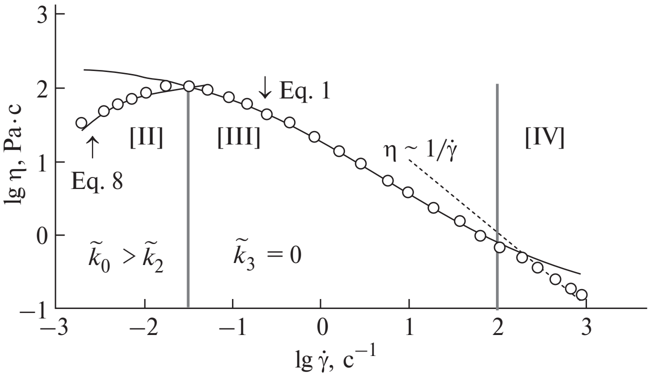

Fig. 1. Dependence of viscosity on shear rate in double logarithmic coordinates for aqueous solution of polyethylene oxide with a mass concentration of 2.5 %. Experimental data from [19].

Fig. 4 shows the results of approximation by equations (1) and (8) in root coordinate plots.

The coefficients of the rheological equations are presented in Table 2. It can be seen that the value of $\eta_c^{1/2}$ is much smaller than $\eta^{1/2}(0)$; the value of $\eta^{1/2}(0)$ is comparable to the value of $\eta_{cv}^{1/2}$. The value of $\tau_{cv}^{1/2}$ is positive, which indicates the predominance of the process of formation over the process of destruction of contacts between micelles.

Fig. 5 shows the viscosity curve for the emulsion of Newtonian oil in aqueous solution given in the book [7]. The experimental data are presented in Table 4 (Appendix 2). The oil is a mixture of: tritolyl phosphate

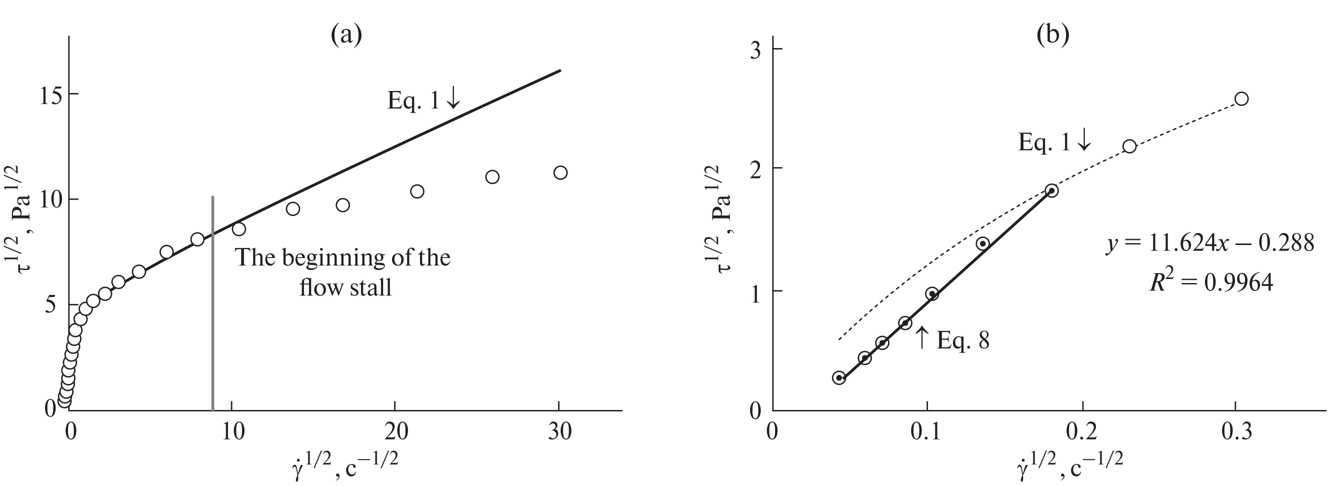

Fig. 2. Dependence of shear stress on shear rate in root coordinates for aqueous solution of polyethylene oxide with a mass concentration of 2.5%. a – on the full range of shear rates; b – on the range of low shear rates.

(24 wt%) and dioctyl phthalate (76 wt%). The aqueous solution has a viscosity of 0.00265 Pa·s and contains 20 wt. % of anionic surfactant. The ratio of the viscosity of the oil to the viscosity of the aqueous solution is 24.7.

Fig. 6 shows the results of approximation by equations (1) and (8) in root coordinate plots.

In Fig. 5. there are two flow regimes. Regime (II) corresponds to equilibrium flow, during which the processes of formation and destruction of contacts between drops due to shear occur, but the destruction process prevails ($\tilde{k}_1 > 0$, $\tilde{k}_3 > 0$, $\tilde{k}_0 < \tilde{k}_2$). Therefore, the value of $\tau_{cv}^{1/2}$ is less than zero. Plot (III) corresponds to the equilibrium flow, in which no contacts are formed due to shear, but only the destruction of contacts takes place ($\tilde{k}_1 > 0$, $\tilde{k}_3 = 0$).

The coefficients of the rheological equations are presented in Table 2. The value of $\eta_c^{1/2}$ is much smaller than $\eta^{1/2}(0)$; the value of $\eta^{1/2}(0)$ is comparable to the value of $\eta_{cv}^{1/2}$. The value of $\tau_{cv}^{1/2}$ is negative, which indicates the predominance of the process of destruction over the process of formation of contacts between the droplets.

The considered examples show that “experimental windows” demonstrate different flow regimes in the study of different structured fluids. Difficulties in data interpretation can arise if the flow regimes are only partially represented in the plots. Therefore, it is important to perform measurements over as large an interval of shear rates as possible, as well as to choose a measurement time sufficient to reach the equilibrium flow state at each measurement.

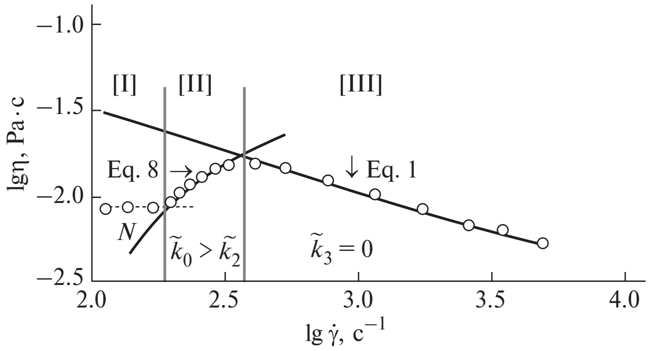

Fig. 3. Dependence of viscosity on shear rate in double logarithmic coordinates for CTAB/NaSal micellar solution with surfactant concentration $\boldsymbol{C}_\mathrm{D}(\boldsymbol{M}) = 0.08$. Experimental data from [20].

It should be added that there is another structural approach to describe the viscosity of a structured fluid. The rheological model [21] describes the dependence of shear viscosity on the volume concentration $\eta(\Phi)$, with each viscosity curve obtained for a constant shear rate [22]. In the model proposed by us, the coefficients (parameters) of the rheological equation of the form $\eta(\dot{\gamma})$ depend on the concentration of the dispersed phase. The generalized flow equation is able to approximate the flow curves, which were previously described by the Herschel–Bulkley or Cross equations, for a variety of disperse systems, including polymer composites [23].

CONCLUSION

This paper presents the equations of the structural rheological model, which describe equilibrium steady-state and equilibrium oscillatory flow from a unified point of view. These equations are necessary and sufficient for analyzing rheological curves $\tau(\dot{\gamma})$, $N_1(\dot{\gamma})$, $G''(\omega)$, $G'(\omega)$. The equations provide an alternative to equations using the power law (Herschel–Bulkley, etc.) and equations based on mechanical models (spring, damper, dry friction element).

Four flow regimes are distinguished on the full interval of shear rates (or oscillation frequency). In the interval (I) the structure of the system is practically constant, which corresponds to the “Newtonian” behavior. In the interval (II) there is simultaneous formation and destruction of contacts between particles (entanglements between macromolecules), which is described by a rheological equation with two coefficients. If the formation process prevails, the shear viscosity η increases; if the destruction process prevails, the viscosity η decreases with increasing shear rate $\dot{\gamma}$. The same applies to shear elasticity η_{ST} ($= N_1 / \dot{\gamma}$), dynamic viscosity η′ and dynamic elasticity η″. In the interval (III), only shear-induced contact failure

Table 1. Rheological characteristics of polymer solution, micellar solution, and emulsion: coefficients of rheological equations 1 and 8 (SI system)

Structured fluid	$\tau_c^{1/2}$	$\eta_c^{1/2}$	χ	$\eta^{1/2}(0)$	$\eta_{cv}^{1/2}$	$\tau_{cv}^{1/2}$
Polyethylene oxide solution	5.29	0.364	0.362	14.98	11.62	0.288
CTAB/NaSal micellar solution	2.36	0.042	7.32	0.364	0.232	1.924
Oil emulsion in aqueous solution	5.35	0.306	0.676	8.211	2.30	−1.04

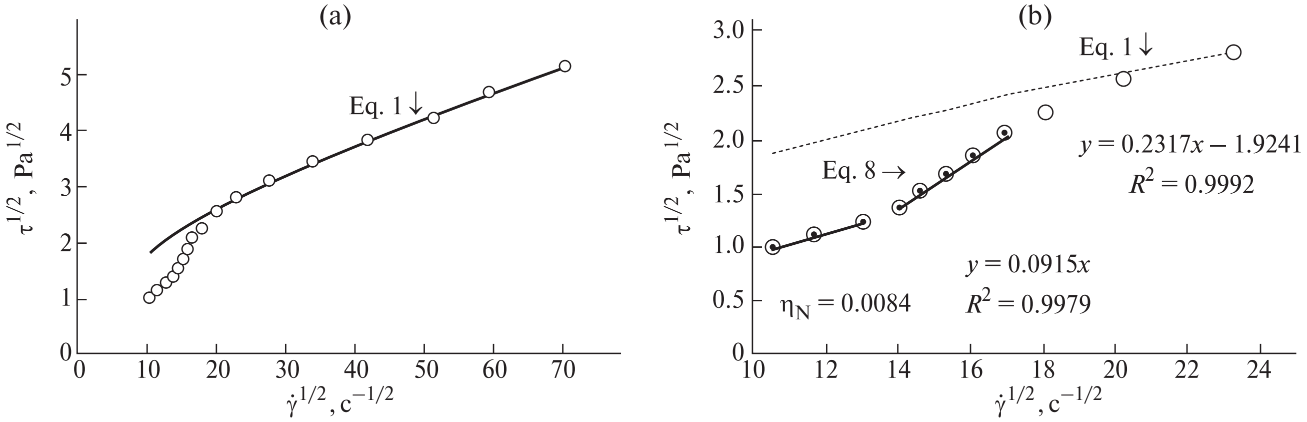

Fig. 4. Dependence of shear stress on shear rate in root coordinates for CTAB/NaSal micellar solution with surfactant concentration $C_D(M) = 0.08$. a – at full shear rate interval; b – at low shear rate interval.

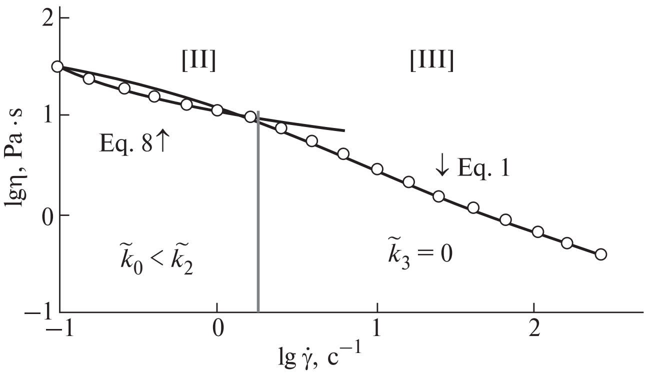

Fig. 5. Dependence of viscosity on shear rate in double logarithmic coordinates for aqueous oil emulsion with volume concentration $\varphi = 0.8$.
Experimental data from [7].

(entanglement rupture) occurs, which is described by a rheological equation with three coefficients. As the shear rate (or frequency) increases, the rheological quantities η, η_{ST}, η', η'' decrease.

At interval (IV), there is an anomalous decrease in rheological values τ, G'' and G', which is possibly due to shear stratification and change in flow velocity profile.

Examples of the use of the equations at selected shear rate intervals in describing the flow curves of some disperse systems (polymer solution, micellar solution, emulsion) are given.

FUNDING

The research was carried out under the budgetary funding of Lomonosov Moscow State University, Faculty of Chemistry, CiT&S No. 121031300084-1.

ETHICS DECLARATION

There are no human or animal studies in this paper.

CONFLICT OF INTERESTS

The authors declare that they have no conflict of interests.

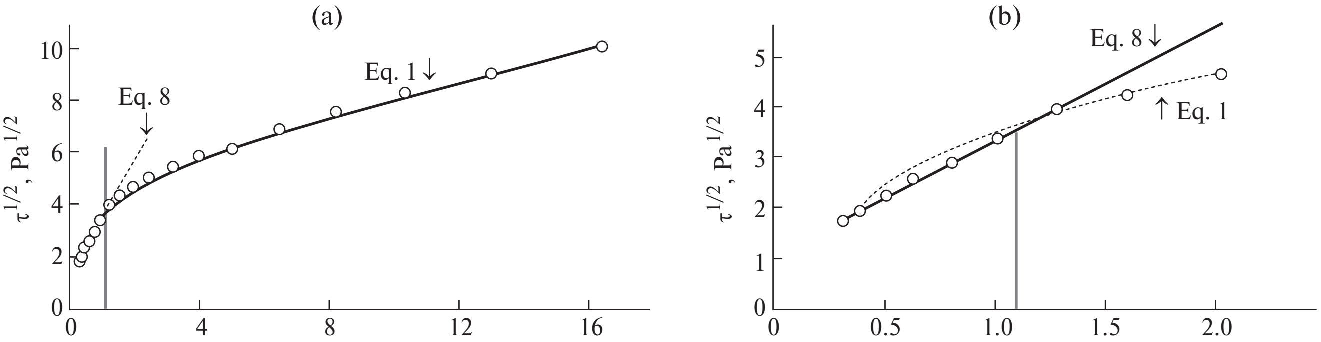

Fig. 6. Dependence of shear stress on shear rate in root coordinates for aqueous oil emulsion with volume concentration $\varphi = 0.8$: *a* – at the full range of shear rates; *b* – at the interval of low shear rates.

REFERENCES

1. *Vinogradov G.V., Malkin A.Ya.* Rheology of polymers. M.: Khimiya, 1977. 440 p.
2. *Hunter R.J.* Rheology of colloidal dispersions. Oxford University Press. 1989. Pp. 993–1052.
3. *Barnes H.A., Hutton J.F., Walters K.* An introduction to rheology. Amsterdam: Elsevier. 1989. 199 p.
4. *Barnes H.A.* A Handbook of elementary rheology. Aberystwyth: University of Wales. 2000. 201 p.
5. *Shramm G.* Fundamentals of practical rheology and rheometry / trans. from Eng., V.G. Kulichikhin (ed.). M: Kolos. 2003. 312 p.
6. *Malkin A.Ya., Isaev A.I.* Rheology: concepts, methods, applications / trans. from Eng. SPb: Professiya. 2007. 560 p.
7. *Larson R.G.* The structure and rheology of complex fluids. New York, Oxford: Oxford University Press. 1999. 668 p.
8. *Kirsanov E.A.* Flow of dispersed and liquid crystal systems. Ivanovo: Izd-vo “Ivanovskiy gosudarstvennyy universitet”. 2006. 232 p.
9. *Kirsanov E.A., Matveenko V.N.* Non-Newtonian flow of dispersed, polymer, and liquid crystal systems. The structural approach. M.: Tekhnosfera. 2016. 384 p.
10. *Casson N.* A flow equation for pigment-oil suspensions of the printing ink type // Rheology of disperse systems / ed. Mill C.C. London: Pergamon Press. 1959. Pp. 84–104.
11. *Cross M.* Rheology of non-Newtonian fluids: a new flow equation for pseudoplastic systems // J. Colloid Sci. 1965. Vol. 20. Pp. 417–437.
12. *Matveenko V.N., Kirsanov E.A.* Structural substantiation of the non-Newtonian flow // Vestnik Moskovskogo universiteta. Seriya 2. Khimiya. 2017. Vol. 58. No. 2. Pp. 59–82.
13. *Matveenko V.N., Kirsanov E.A.* Structural viscosity and structural elasticity of polymer melts // Zhurn. prikl. khimii. 2018. Vol. 91. No. 5. Pp. 72–748.
14. *Matveenko V.N., Kirsanov E.A.* Structural model of viscoelasticity of polymers // Vestnik Moskovskogo universiteta. Seriya 2. Khimiya. 2019. Vol. 60. No. 4. Pp. 207–225.
15. *Matveenko V.N., Kirsanov E.A.* Rheology of polydimethylsiloxane melt. Structural approach // Vestnik Moskovskogo universiteta. Seriya 2. Khimiya. 2022. Vol. 63. No. 2. Pp. 55–68.
16. *Matveenko V.N., Kirsanov E.A.* Normal stresses in the rheology of structured systems // Vestnik Moskovskogo universiteta. Seriya 2. Khimiya. 2022. Vol. 63. No. 3. Pp. 187–204.
17. *Levinskiy A.I.* On the rheology of thixotropic and rheopex suspensions // Colloid Journal. 2023. Vol. 85. No. 6. Pp. 762–767. https://doi.org/10.31857/S0023291223600591
18. *Yufei Wei.* Investigating and modeling the rheology and flow instabilities of thixotropic yield stress fluids. A dissertation submitted in partial fulfillment of the requirements for the degree of Doctor of Philosophy (Chemical Engineering). University of Michigan. 2019. 139 p.
19. *Ebagninin K.W., Benchabane A., Bekkour K.* Rheological characterization of poly(ethylene oxide) solutions of different molecular weights // J. Colloid Interface Sci. 2009. Vol. 336. No. 1. Pp. 360–367. https://doi.org/10.1016/j.jcis.2009.03.01
20. *Cressely R., Hartmann V.* Rheological behaviour and shear thickening exhibited by aqueous CTAB micellar solutions // Eur. Phys. J. B. 1998. Vol. 6. Pp. 57–62. https://doi.org/10.1007/s100510050526
21. *Rajinder Pal.* New generalized viscosity model for non-colloidal suspensions and emulsions // Fluids. 2020. Vol. 5. No.150. Pp. 1–28. https://doi.org/10.3390/fluids5030150
22. *Mehdi Maleki, Clément de Loubens, Hugues Bodiguel.* Viscous resuspension of droplets // Phys. Rev. Fluid. 2022. Vol. 7. No. 1. P. L011602. https://doi.org/10.1103/PhysRevFluids.7.L011602
23. *Fedorov Yu.I., Mikhaylov A.S.* Application of the generalized flow equation for highly filled polymer systems // Vestnik tekhnologicheskogo universiteta. 2020. Vol. 23. No. 8. Pp. 90–93.

APPENDIX 1

Casson rheological model [10]. The model considers fluid systems possessing a limiting dynamic shear stress. The plastic behavior of such systems is well described by the equation $\tau^{1/2} = \tau_c^{1/2} + \eta_c^{1/2}\dot{\gamma}^{1/2}$, where the Casson coefficients $\tau_c^{1/2}$ and $\eta_c^{1/2}$ correspond to the limiting dynamic shear stress and viscosity coefficient at infinitely large shear rate. Experimental points in the root coordinates $\tau^{1/2} - \dot{\gamma}^{1/2}$ in this case are located on the same straight line, which is well confirmed by experimental data for dye dispersions, blood and many structured fluids.

Casson derived this equation based on the microrheological theory, in which aggregates-chains of two or more particles arise under the action of some cohesive forces F_s. Since hydrodynamic calculations to describe the chain breakage and energy dissipation during chain flow proved to be too complicated, Casson replaced chains with long model cylinders, assuming that their hydrodynamic behavior in simple shear flow is identical to that of rigid chains of particles. When flowing around opposite parts of the cylinder, a hydrodynamic force F_H along the axis arises, which at a certain orientation of the cylinder contributes to its rupture. The cylinder breaks into two parts if the tensile hydrodynamic force F_H exceeds the cohesive force F_s, which prevents the cylinder from breaking. Long cylinders rupture in shear flow, and short cylinders spontaneously unite upon collision into longer cylinders. This replacement of chains by cylinders made it possible to use Kuhn's model to calculate the hydrodynamic rupturing force and the magnitude of energy dissipation.

Omitting Casson's calculations given by us in published monographs [8, 9], let us write down the expression for the viscosity of the "diluted" suspension of model cylinders:

$$\eta = \eta_0 \ (1 - \Phi) + \eta_0 \bar{a} \Phi \left(\alpha + \beta / (\eta_0 \dot{\gamma})^{1/2}\right),$$

where η_0 – is the viscosity of the dispersion (liquid) medium, the coefficient $\bar{a} \approx 0.7$ assuming random initial orientation of model cylinders. The parameter α can be interpreted as an extremely low axial ratio at infinite shear rate. The root of the shear rate appears in the equation. The mean-field method (approximation of Brinkman and Roscoe, 1952) was used to account for the hydrodynamic interaction of the particles. As a result of the calculation, the root of the viscosity value appears in the equation:

$$\eta^{1/2} = \frac{\tau_c^{1/2}}{\dot{\gamma}^{1/2}} + \eta_c^{1/2} .$$

As a result of modification of the Casson model, we obtained a generalized flow equation $\tau^{1/2} = \frac{\tau_c^{1/2}}{\dot{\gamma}^{1/2} + \chi}\dot{\gamma}^{1/2} + \eta_c^{1/2}\dot{\gamma}^{1/2}$, and the calculated values of coefficients slightly differ from those obtained in the Casson model.

Cross rheological model [11]. The processes of destruction and recovery of aggregates during shear flow can be described using kinetic equations. This approach was used by Cross, who replaced the concentration of a substance used in chemical kinetics by the number of bonds between particles (L). Cross assumed that a suspension consists of chains of particles with an average number L of bonds between particles, introduced a rate constant for bond formation ($\tilde{k}_2$), a rate constant for spontaneous bond breaking ($\tilde{k}_0$) and a rate constant for bond breaking due to shear flow ($\tilde{k}_1\dot{\gamma}^n$). The rate of change of the number of bonds between particles is assumed to $\frac{dL}{dt} = \tilde{k}_2 N - \left(\tilde{k}_0 + \tilde{k}_1\dot{\gamma}^n\right) L$, where N is the total number of initial particles in a unit volume, L is the number of bonds between particles.

Cross used an empirical expression from polymer theory: $\eta = \eta_\infty + BL$, where η_∞ is the viscosity of the system at $\dot{\gamma} \to \infty$, when all bonds are broken, B is some coefficient. Omitting here Cross's calculations, let us write down the final equation of Cross in the form:

$$\frac{\eta - \eta_\infty}{\eta(0) - \eta_\infty} = \frac{1}{1 + \left(\tilde{k}_1/\tilde{k}_0\right)\dot{\gamma}^n}.$$

Commenting on the derivation of the Cross equation, Hunter noted that there is no theoretical justification for the choice of the constant as $\tilde{k}_1\dot{\gamma}^n$. The Cross equation is widely used to describe dispersed and polymeric systems.

As a result of the modification of the Cross model, we obtained an equation similar to the generalized flow equation, where the coefficients are expressed through the rate constants of fracture/aggregate formation, the number of bonds is replaced by the number of aggregated particles, and the viscosity root and shear rate root are introduced by analogy with the Casson model.

Coagulation and aggregation of particles. Let us consider the relationship between the equations of the structural model and the classical theory of coagulation. Let us assume that there is no spontaneous detachment of particles from aggregates ($\tilde{k}_0 = 0$) and no flow ($\tilde{k}_1\dot{\gamma}^{1/2}=0$). Then the process of particle aggregation formally occurs up to the formation of a continuous mesh

$$(N_2 = N){:}\ \frac{dN_2}{dt} = \tilde{k}_2 N;\ \int_0^N dN_2 = \int_0^{t_g} \tilde{k}_2 N dt;\ N = \tilde{k}_2 N t_g;$$

i.e., the time of formation of a continuous mesh is equal to $t_g = 1/\tilde{k}_2$.

In coagulation theory, the initial equation contains some number of "conditional" particles ν, which represent both individual particles and aggregates of particles: $\frac{d\nu}{dt} = -k\nu^2$. The solution has the form: $\nu(t) = \frac{\nu_0}{1 + k\nu_0 t}$. The formation of a continuous mesh of particles is formally equivalent to the formation of one large "particle" i.e.

$\frac{\nu_0}{1 + k\nu_0 t_g} = 1$. Hence, the time of “complete” coagulation is formally equal to $t_g = \frac{1}{k}(1 - \frac{1}{\nu_0}) \approx \frac{1}{k}$. Thus, there is no direct contradiction between the description of the aggregation process (in the Cross equation) and the description of the coagulation process, although both kinetic equations actually no longer work when large aggregates of particles appear.

Kinetic equations for aggregate formation/destruction processes

We have proposed the expression

$$\frac{d\tilde{N}_2}{dt} = \tilde{k}_2\tilde{N} - \tilde{k}_0\tilde{N}_2 - \tilde{k}_1\dot{\gamma}^{1/2}\tilde{N}_2 + \tilde{k}_3\dot{\gamma}^{1/2}\tilde{N}_1.$$

In [17], a kinetic equation is presented, which we present here in the form necessary for comparison, replacing the volume concentration by the number of $\tilde{N}_1$ singlet or $\tilde{N}_2$ duplets in a unit volume and substituting indices for the rate constants:

$$\frac{d\tilde{N}_1}{dt} = -\tilde{k}_2\tilde{N}_1^2 + \tilde{k}_0\tilde{N}_2 + \tilde{k}_1\dot{\gamma}\tilde{N}_2 \text{ or}$$

$$\frac{d\tilde{N}_2}{dt} = \tilde{k}_2\tilde{N}_1^2 - \tilde{k}_0\tilde{N}_2 - \tilde{k}_1\dot{\gamma}\tilde{N}_2.$$

The difference is the lack of square root, the change of the system to singlet and duplets, and the use of classical coagulation theory for the particle aggregation process.

In [18], a kinetic equation for thixotropic dispersion of the form $d\Lambda / dt = -k_1\Lambda\dot{\gamma}^{\beta} + k_3(1 - \Lambda)\dot{\gamma}^{1/2} + k_0(1 - \Lambda)$, where Λ is a structural parameter that describes the change in internal structure with changing shear rate, is used. If we write the structural parameter as the relative number of aggregated particles ($\Lambda = \tilde{N}_2 / \tilde{N}$), we obtain an equation of the form $d\tilde{N}_2 / dt = k_0\tilde{N} - k_0\tilde{N}_2 - k_1\dot{\gamma}^{\beta}\tilde{N}_2 + k_3\dot{\gamma}^{1/2}\tilde{N}_1$.

The difference is that the rate constants $\tilde{k}_0 = \tilde{k}_2$ are equated and the degree exponent β has an arbitrary value. It is important to note that the terms of the equations describing the formation of aggregates under the action of shear completely coincide.

APPENDIX 2

Table 2. Dependence of viscosity on shear rate of aqueous solution of polyethylene oxide with mass concentration of 2.5%

$\lg\dot{\gamma}$, c^{-1}	−2.686	−2.425	−2.273	−2.116	−1.954	−1.724	−1.473
$\lg\eta$, Pa·s	1.479	1.661	1.739	1.818	1.909	2.000	1.987
$\lg\dot{\gamma}$, c^{-1}	−1.028	−0.824	−0.594	−0.343	−0.061	0.211	0.462
$\lg\eta$, Pa·s	1.844	1.739	1.609	1.479	1.297	1.115	0.945
$\lg\dot{\gamma}$, c^{-1}	0.755	1.001	1.283	1.582	1.822	2.042	2.293
$\lg\eta$, Pa·s	0.698	0.548	0.333	0.151	−0.018	−0.188	−0.344
$\lg\dot{\gamma}$, c^{-1}	2.460	2.669	2.837	2.962	–	–	–
$\lg\eta$, Pa·s	−0.487	−0.643	−0.760	−0.865	–	–	–

Table 3. Dependence of viscosity on shear rate of CTAB/NaSal micellar solution with concentration of surface active substance C_D (*M*) = 0.08 at the ratio of $C_D / C_{\mathrm{NaSal}} = 4.21$

$\lg\dot{\gamma}$, c^{-1}	2.050	2.142	2.233	2.300	2.333	2.375
$\lg\eta$, Pa·s	−2.082	−2.078	−2.074	−2.047	−1.990	−1.941
$\lg\dot{\gamma}$, c^{-1}	2.417	2.463	2.517	2.617	2.733	2.892
$\lg\eta$, Pa·s	−1.897	−1.853	−1.826	−1.818	−1.849	−1.924
$\lg\dot{\gamma}$, c^{-1}	3.067	3.250	3.425	3.550	3.700	–
$\lg\eta$, Pa·s	−2.003	−2.091	−2.179	−2.215	−2.281	–

Table 4. Dependence of viscosity on shear rate of oil emulsion in aqueous solution with volume concentration $\varphi = 0.8$ and average droplet radius 7.7 μm

$\lg\dot{\gamma}$, c^{-1}	−1.000	−0.795	−0.577	−0.385	−0.179	0.013
$\lg\eta$, Pa·s	1.484	1.369	1.280	1.204	1.102	1.038
$\lg\dot{\gamma}$, c^{-1}	0.218	0.410	0.615	0.808	1.026	1.218
$\lg\eta$, Pa·s	0.975	0.847	0.720	0.579	0.439	0.312
$\lg\dot{\gamma}$, c^{-1}	1.410	1.628	1.833	2.038	2.230	2.436
$\lg\eta$, Pa·s	0.166	0.045	−0.076	−0.197	−0.312	−0.427

COLLOID JOURNAL, 2025, Vol. 87, No. 1, pp. 48–52

GENERATION OF LATEX PARTICLES AND PHASE FORMATION IN A HETEROGENEOUS STATIC MONOMER–WATER SYSTEM

© 2025 A. A. Hovhannisyan*, G. K. Grigoryan, A. G. Nadaryan, and N. H. Grigoryan

Scientific and Technological Center for Organic and Pharmaceutical Chemistry of the National Academy of Sciences of Armenia, Erevan, Armenia

**e-mail: hovarnos@gmail.com*

Received September 19, 2024
Revised October 16, 2024
Accepted October 16, 2024

Abstract. The aim of this work is to find new ways to synthesize latexes (polymer suspensions) with a given size and surface structure of particles. The need for such latexes is not large-scale, but their development and production are extremely important for the development of high technologies. Monodisperse latexes are especially valuable in immunological diagnostics of a wide range of diseases. The article presents the results of studies of the nucleation of latex particles in a heterogeneous monomer–water system. The results of these studies made it possible to find conditions for the reproducible synthesis of monodisperse polystyrene latexes. In order to change the surface structure of latex particles, cetyl alcohol was dissolved in the initial monomer phase (styrene). The article presents the results of electron microscopic studies of the synthesized latexes. Nano crystals of this alcohol are clearly visible on the surface of the latex particles. It is suggested that, in deep monomer conversions, the process of crystallization of cetyl alcohol begins in polymer-monomer particles.

Keywords: *polymerization, latex, cetyl alcohol, styrene, phase formation, crystallization, interface*

DOI: 10.31857/S00232912250106e3

INTRODUCTION

The mechanism of nucleation and formation of latex particles during emulsion polymerization has been studied by many authors. According to the Harkins theory [1], in micellar emulsions latex particles are formed from micelles in the form of polymer-monomer particles (PMPs). In [2, 3] it is assumed that PMPs are also formed as a result of homogeneous association of oligomers in the aqueous phase.

Latexes are also synthesized without emulsifiers, in monomer–water dispersions. The aim of such works is to synthesize monodisperse latexes with a specific chemical structure of the surface of dispersed particles. Such synthesis is often possible by selection of monomers and co-monomers [4–6]. In [7], the results of a systematic study of polymerization processes and polymer disperse phase formation in emulsifier-free monomer–water systems are presented. The authors showed that the choice of conditions for heterophase polymerization largely determines the colloidal parameters of the final suspension. This work also shows ways to modify the surface structure of emulsifier-free polymer suspensions.

The mechanism of latex particle formation, without emulsifier (in the absence of micelles) has been studied in [8, 9, 10]. In [8], measurements of optical density in different zones of the aqueous phase during polymerization led the author to the conclusion that as a result of polymerization in the monomer–water interface, the monomer is dispersed into small droplets containing polymer molecules. The stability of such polymer-monomer particles, according to the author, is due to the ionic end groups of the polymer molecules. The authors [9, 10] came to the same conclusion after using atypical experimental methods (conductivity measurement, optical microscopy, and polymerization without stirring) to study emulsion polymerization of styrene.

In [11] it is assumed that in emulsifier-free systems PMPs are also formed by the mechanism of homogeneous association of oligomers in the aqueous phase. In [12], the possibility of PMP generation by penetration of a growing radical into the volume of monomer droplets is also considered.

In micellar emulsions, the generation of latex particles can occur simultaneously by different mechanisms [12]. Obviously, for this reason, the size distribution of latex particles narrows in the absence of micelles.

It becomes obvious that one of the ways to synthesize monodisperse latexes may be to find a polymerization method in which only one mechanism of latex particle formation is active. This is what the experimental part of this work is aimed at.

Mass transfer occurring during the polymerization reaction at the monomer–water interface was confirmed experimentally during styrene polymerization in microfluidics, which allowed the use of infrared thermospectroscopy for simultaneous IR transmittance and thermoemission imaging measurements [13]. In this experiment, intense heat and concentration fluxes in the contact layer of laminar flows of styrene and toluene containing an initiator were recorded in the contact zone of the two fluids. Styrene and toluene are unlimitedly soluble in each other, and mass transfer does not change the homogeneity of the system, but in the two-phase system styrene–water solution of the initiator, mass transfer from the monomer phase to the aqueous phase can lead to saturation of the aqueous phase with the monomer [14–15]. In water, nonpolar hydrocarbon molecules tend to associate [16], and a small supersaturation is sufficient for the nucleation of styrene microdroplets in the aqueous phase.

Diffusion in liquids is a slow process, and it can be assumed that microdroplets of monomers can exist in a static system until they transform into PMP, the stability of which is ensured by ionic end groups of growing radicals and polymers.

The formation of monomer microdroplets also follows from the strong dependence of the interfacial surface tension of liquids on temperature. It can be assumed that mixing of liquids and dispersion of the system occurs as a result of a local increase in the temperature of the monomer–water interfacial layer during polymerization reactions there.

Supersaturation and phase formation can also occur in PMP if the monomer phase includes substances that do not participate in polymerization reactions. Depending on the nature of the substances and polymerization conditions, nuclei of a new phase may appear both during polymerization and during evacuation of residual monomer from latex. Phase formation in PMP can also occur when the latex storage temperature changes. Depending on the structure of the impurity molecules, crystals can grow on the surface of latex particles. Obviously, the crystals must be insoluble in water. The experimental part of the paper presents the first results of studying the formation phases in PMP. The studies were carried out during styrene polymerization in a static heterogeneous monomer–water system in the presence of cetyl alcohol (CA).

The choice of CA was conditioned by the fact that this alcohol is insoluble in water, is not an emulsifier and crystallizes from solutions of organic solvents. The low density and melting point of this alcohol were also taken into account. All these qualities of CA allowed us to hopefully detect nanoscale CA crystals on the surface of styrene latex particles.

RESULTS AND DISCUSSION

1. Starting substances and methods of research

Starting materials: styrene (Aldrich) was purified from stabilizer by distillation under vacuum, potassium persulfate (Sigma Aldrich), cetyl alcohol, azoisobutyric acid dinitrile – reagent grade products, water – double distillate.

Electron microscopic photographs were obtained using a Prism3 scanning electron microscope (Czech Republic), NMR spectra were obtained using a Mercury 300 spectrometer (Varian). The size and Z-potential of latex particles were determined using a Liteizer 500 device.

2. Polymerization and phase formation in static and semi-static monomer–water systems

Polymerization was carried out in temperature-controlled tubes in which the monomer phase (styrene or a solution of CA in styrene) was gently applied to the surface of an aqueous solution of potassium persulfate (PP). The experimental temperature was 50 °C, the volume of monomer phase was 2 mL, the volume of aqueous phase was 30 mL, and the concentration of potassium persulfate in water was 0.4%. The dry residue of the aqueous phase was determined by gravimetry, the viscosity of the monomer phase was determined by viscometry.

In the static system, polymerization is accompanied by turbidity (change in optical density) of the aqueous phase, which indicates the formation of a dispersed phase in the system. The turbidity of the aqueous phase was determined using a SF-24 spectrophotometer at a wavelength of 540 nm. The experiments were carried out simultaneously in six test tubes. One sample was taken from each tube for analysis.

As noted above, in the static system polymerization is accompanied by a turbidity of the aqueous phase, which is recorded by the spectrometer after a certain period of time from the beginning of polymerization. In our experiments, this period lasted 90 min and did not depend on the concentration of CA (from 0 to 6%). This result indicates the inertness of CA in the process of "emulsification" of the system. A photograph of the initial stage of aqueous phase turbidity is presented in Fig. 1.

As can be seen in Fig. 1, turbidity begins at the monomer–water interface and gradually deepens into the aqueous phase. This pattern is particularly clear when an inert salt (potassium sulfate) is dissolved in water [8], or ethanol in styrene [17]. Potassium sulfate increases the density of the aqueous phase, while ethanol decreases the density of dispersed particles. In both cases, the residence time of dispersed particles in the zone of their formation increases.

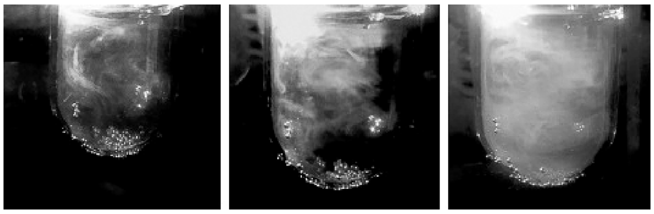

Fig. 1. The picture of turbidity change in the aqueous phase at the initial stage of polymerization.

Fig. 2. Photographs of tubes in which polymerization was carried out in semi-static (tube 1) and static (tube 2) mode.

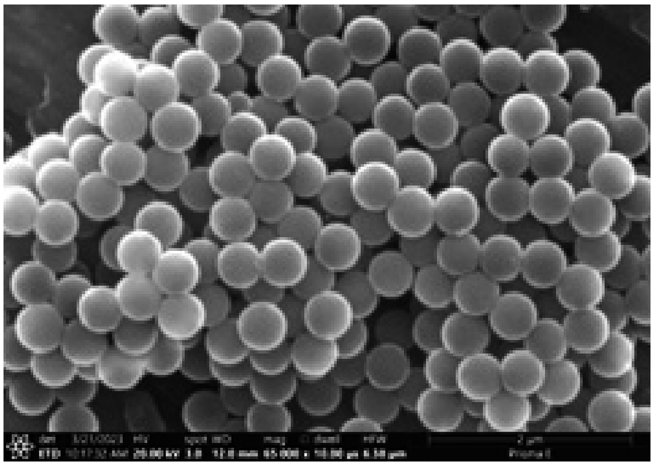

Fig. 3. Electron microscopic photograph of polystyrene latex synthesized in a semi-static monomer–water system.

The concentration of latexes synthesized in the static system does not exceed 2%. The time to reach this concentration is approximately 24 hours. The viscosity of the monomer phase does not change during this time.

The dynamics of aqueous phase turbidity changed dramatically when polymerization was carried out in a semi-static system in which only the aqueous phase was stirred. A photograph of this experiment is shown in Fig. 2. In the first test tube, the polymerization was carried out under semi-static conditions, while in the second test tube, the static condition was maintained. In the semi-static system, the aqueous phase remained transparent in throughout the entire stirring time (more than 240 min). In all probability, this is the amount of time required to reach supersaturation in the entire volume of the aqueous phase in this experiment. Turbidity in this test tube only began to be observed after the mechanical stirrer was suspended. In the control tube, the results of the previous experiment were reproduced (Fig. 1).

In a semi-static system, local supersaturation of the aqueous phase is impossible, and the results of this simple experiment can be considered to confirm the assumption that in a static system the driving force for the nucleation of monomer microdroplets is the supersaturation of the monomer–water interface layer by styrene molecules.

An electron microscopic photograph of latex synthesized in a semi-static system is shown in Fig. 3. The sample was taken after complete turbidity of the aqueous phase. As can be seen from the figures, the latex synthesized in the semi-static system has a rather narrow particle diameter distribution. This result is well reproducible.

The synthesized latexes are stable (*Z*-potential of particles is equal to –67.3 mV), have a fairly narrow distribution of particles in diameter, which allows their use in immunodiagnostics, as well as for other applied purposes. The particle diameter distribution is shown in Fig. 4.

3. Phase formation in a polymer-monomer particle

Initially, phase formation in PMP was investigated by polymerization of styrene in a block. The CA content in styrene was 6%. The polymerization was initiated by azoisobutyric acid dinitrile. Crystallization began to be observed in the viscous polymer-monomer mixture when the temperature of the system was slowly lowered to 5°C. (Fig. 5). The 1H NMR spectrum of the crystalline

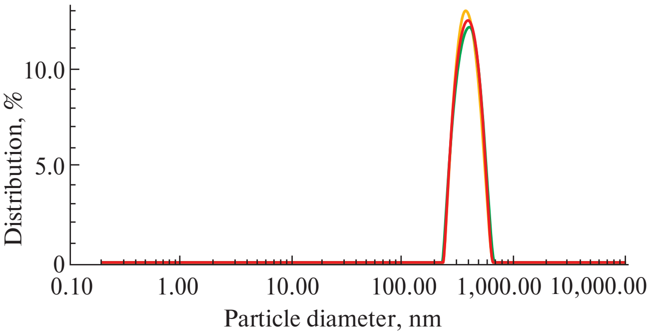

Fig. 4. Particle diameter distribution of latex synthesized in a semi-static styrene–water potassium persulfate solution system.

Fig. 5. Appearance of CA crystals in styrene block copolymer when the temperature is lowered to 5°C.

Fig. 6. Crystallization of CA in styrene when the solution temperature is lowered to 5°C. The concentration of CA in styrene is 6%.

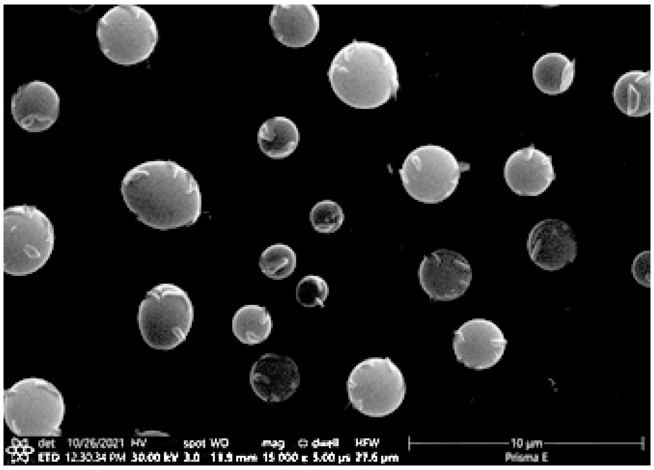

Fig. 8. Electron microscopic photograph of diluted polystyrene latex synthesized in the presence of 2% CA in styrene.

particles was identical to that of the CA. The nucleation and growth of the CA crystal was also observed when the temperature of the solution of this alcohol in styrene was lowered (Fig. 6).

Electron microscopic photographs of latex particles synthesized in a static heterogeneous styrene–water PP solution system in the presence of CA are shown in Fig. 7. The needle-like crystals and the "growth cone" on the PMP surface are clearly visible in these photographs. These photos also show very small spherical particles, the composition of which is not very clear yet.

Structural formations on the surface of latex particles are also detected at low concentrations of CA in styrene. Fig. 8 shows electron microscopic photograph of polystyrene latex synthesized at 2% CA in styrene.

CONCLUSION

The results of this work allowed us to make a final conclusion that in the static heterogeneous monomer–water system the interface is one of the generation zones of latex particles, which allowed us to find conditions for reproducible synthesis of monodisperse polystyrene latexes.

The paper reveals the conditions for the synthesis of latex particles in the heterogeneous monomer–water system carrying nanoscale crystals of organic substances on their surface.

FUNDING

This work was funded through the organization's budget. No additional grants were received to conduct or supervise this particular study.

ETHICS DECLARATION

There are no human or animal studies in this paper.

CONFLICT OF INTERESTS

The authors of this paper declare that they have no conflict of interests.

Fig. 7. Electron microscopic photographs of polystyrene latex synthesized in the presence of 6% CA in styrene.

REFERENCES

1. *Harkins W.D.* General theory of mechanism of emulsion polymerization. II // J. Polym. Sci. 1950. Vol. 5. Pp. 217–251. https://doi.org/10.1002/pol.1950.120050208
2. *Fitch R.M., Tsai C.H.* Homogeneous nucleation of polymer colloids: the sole of soluble oligomeric radicals // Amer. Chem. Soc. Polym. Prep. 1970. Vol. II. Pp. 811–816.
3. *Hansen F.K., Ugelstad J.* Particle nucleation in emulsion polymerization. I. Theory for homogeneous nucleation // J. Polym. Sci., Polym. Chem. Ed. 1978. Vol. 16. No. 8. Pp. 1953–1979. https://doi.org/10.1002/pol.1978.170160814
4. *Grant T.D. Shouldice, Gerald A. Vandezande, Alfred Rudin.* Practical aspects of the emulsifier-free emulsion polymerization of styrene // Eur. Polym. J. 1994. Vol. 30. No. 2. Pp. 179–183. https://doi.org/10.1016/0014-3057(94)90157-0
5. *Ali Safinejad, Saeed Pourmahdian, Behzad Shirkavand Hadavand.* Emulsifier-free emulsion polymerization of acrylonitrile-butadiene-carboxylic acid monomers: a kinetic study based on polymerization pressure profile // J. Dispers. Sci. Technol. 2020. Vol. 41. No. 2. Pp. 157–167. https://doi.org/10.1080/01932691.2018.1496835
6. *Chad E. Reese, Sanford A. Asher.* Emulsifier-free emulsion polymerization produces highly charged, monodisperse particles for near infrared photonic crystals // J. Colloid Interface Sci. 2002. Vol. 248. No. 1. Pp. 41–46. https://doi.org/10.1006/jcis.2001.8193
7. *Prokopov N.I., Gritskova I.A., Cherkasov V.P., Chalykh A.E.* Synthesis of monodisperse functional polymer microspheres for immunological research // Uspekhi khimii. 1996. Vol. 65. No. 2. P. 178.
8. *Oganesyan A.* Free radical polymerization and phase formation in heterogeneous monomer/water systems // *Doctoral (Chem.) Dissertation*, Moscow, Inst. of Fine Chemical Technology, 1986 (in Russ.).
9. *Tauer K., Hernandez H., Kozempel S., Lazarev O., Nazaran P.* Towards a consistent mechanism of emulsion polymerization – new experimental details // Colloid Polym. Sci. 2008. Vol. 286. Pp. 499–515. https://doi.org/10.1007/s00396-007-1797-3
10. *Prokopov N.I., Gritskova I.A., Kiryutina O.P., Khaddazh M., Tauer K., Kozempel S.* Study of the mechanism of emulsifier-free polymerization of styrene // Vysokomolek. Soed. B. 2010 Vol. 52. No. 6. Pp. 1043–1049.
11. *Goodall A.R., Wilkinson M.C., Hern J.* Mechanism of emulsion polymerization of styrene in soap-free systems // J. Polym. Sci., Polym. Chem. 1977. Vol. 15. Pp. 2193–2218. https://doi.org/10.1002/pol.1977.170150912
12. *Peter A. Lovell, F. Joseph Schork.* Fundamentals of emulsion polymerization // Biomacromolecules. 2020. Vol. 21. No. 11. Pp. 4396–4441. https://doi.org/10.1021/acs.biomac.0c00769
13. *Ryu M., Kimber J.A., Sato T., Nakatani R., Hayakawaa T., Romano M., Pradere C., Hovhannisyan A.A., Kazarian S.G., Morikawa J.* Infrared thermo-spectroscopic imaging of styrene radical polymerization in microfluidics // Chem. Eng. J. 2017. Vol. 324. No. 15. Pp. 259–265. https://doi.org/10.1016/j.cej.2017.05.001
14. *Kuzmin A.O., Parmon V.N., Pravdina M.Kh., Yavorskii A.I., Yavorskii N.I.* Mass transfer in a medium with a rapidly renewed interface // Theor. Found. Chem. Eng. 2006. Vol. 40. Pp. 225–232. https://doi.org/10.1134/S0040579506030018
15. *Hovhannisyan A.A., Grigoryan G.K, Khaddazh M., Grigoryan N.G.* On the mechanism of latex particles formation in polymerization in heterogeneous monomer–water system // J. Chem. Chem. Eng. 2015. Vol. 9. Pp. 363–368. https://doi.org/10.17265/1934-7375/2015.05.009
16. *Morawetz H.* Macromolecules in solutions. M.: Mir. 1967. P. 398 (in Russ.).
17. *Oganesyan A.A., Grigoryan, G.K., Khaddazhb M., Gritskova I.A., Nadaryan A.G.* Polymerization in the static heterogeneous system styrene–water in the presence of methanol // Theor. Found. Chem. Eng. 2013. Vol. 47. Pp. 600–603. https://doi.org/10.1134/S0040579513050230

COLLOID JOURNAL, 2025, Vol. 87, No. 1, pp. 53–68

SURFACE MODIFIERS FOR REDUCING BACTERIAL CONTAMINATION IN MEDICINE AND FOOD INDUSTRY

© 2025 Y. V. Cherednichenko*, I. R. Ishmukhametov, and G. I. Fakhrullina

Institute of Fundamental Medicine and Biology, Kazan Federal University, Kazan, Russia

**e-mail: serova.yuliya87@gmail.com*

Received September 08, 2024
Revised November 11, 2024
Accepted November 11, 2024

Abstract. Antibacterial coatings are used in the food and textile industries, in the construction industry, in biotechnology and medicine. The review considers the main types of coatings that prevent fouling with biomacromolecules and microorganisms: anti-adhesive, contact, release-based, multifunctional and intelligent (“smart”) coatings. For each type of coating, the most relevant and effective active substances and their mechanism of action are described. Despite the widespread use of anti-adhesive surfaces and contact coatings, they have many disadvantages that limit the scope of their application and reduce activity and durability. Numerous studies show that multifunctional and intelligent coatings have high potential for practical application and further research on their modification to obtain universal and cost-effective coatings. The main problem of the practical application of such surfaces is the imperfection of methods for assessing the stability and antibacterial properties of the coating in laboratory conditions.

Keywords: *antibacterial coatings, contact, release-based, anti-adhesive, multifunctional, intelligent*

DOI: 10.31857/S00232912250107e9

INTRODUCTION

The original role of surface coatings in industrial applications was to provide corrosion protection and mechanical resistance of materials [1]. Recently, there has been great interest in developing surfaces that reduce microbial adhesion and provide biocidal activity or exhibit combined effects [2–5]. Antimicrobial coatings are materials and substances that modify the surface of another material and give them functions that limit or prevent the growth and multiplication of microorganisms without changing the characteristics of the material itself [6, 7]. To create such coatings, various physical and chemical methods are used to ensure the formation of homogeneous layers. For coatings to be effective, they must include active compounds with a wide range of antimicrobial activity, including antibiotic-resistant microorganisms [8].

Bacterial resistance to antibiotics is one of the most important problems of modern medicine. Bacterial strains can modify the targets of antibiotic action, inhibit the penetration and active excretion of antibiotics from the microbial cell (efflux), form metabolic “shunts”, and produce enzymes that destroy antimicrobial drugs [9, 10]. A particularly alarming factor is the ubiquity of bacterial strains with multiple resistance to antimicrobial agents, as well as the ability of microorganisms to form biofilms [11]. Bacterial biofilms are aggregations of bacteria in a self-secreted polymer matrix. They are formed both on biological and non-biological surfaces and are an important step in the emergence of persistent infections. Within the biofilm, microbes have increased resistance to immune system factors, antibiotics and disinfectants [12]. The matrix of bacterial biofilms slows down the diffusion of antibiotics, and changes in the chemical microenvironment within the biofilm leads to the formation of persistent forms of bacteria that have increased resistance to antimicrobial agents [13, 14]. Therefore, to combat antibiotic resistance, it is necessary to search for new antibacterial agents that would be effective against isolated bacterial strains and bacterial communities forming biofilms.

The development and creation of coatings with antimicrobial properties is of great practical importance and finds application in various fields [15–17]. For example, food packaging systems containing antimicrobial agents can be used not only to reduce the number of pathogens, but also to combat microorganisms that cause food spoilage [18]. Such packaging isolates food from the environment and suppresses microbial growth without affecting its composition [19]. Due to the slow and/or controlled release of antibacterial agents, their inhibition during transportation and storage is ensured, which increases the shelf life of foods [20, 21]. In healthcare facilities, antimicrobial coatings are used as a modern hygienic method to control bacterial contamination [22–24]. Current coatings against bacterial fouling and contamination are capable of: controlling pathogen populations on surfaces and minimizing the risks of resistance to their constituent antimicrobial agents; being stable and (eco)toxicologically safe; affordable and easily implemented in hospital settings [25–27]. Recent advances in the architectonics of nanomaterials have led to the emergence of antibacterial nanoparticles, which can be useful in the textile industry to enhance the antibacterial properties of fabrics, control the spread of pathogenic bacteria and associated infections among humans, and safe for human health and the environment. Such nanoparticles are introduced into the surface of the fabric by plasma technique, laser treatment, cationization, and by functionalizing or modifying the surface of the textile. Moreover, biosensor nanoparticles are embedded into the fabric to monitor human disease states [28–30]. The antimicrobial properties of materials are used in the construction of institutions where high standards of hygiene are required to prevent the formation of bacterial biofilms, mold and mildew, and to protect structures from biodegradation [31, 32]. Antimicrobial agents are introduced by applying paint or coating to the finished surface after construction, by mixing inorganic additives (metal nanoparticles, metal oxides) with concrete or mortar during construction and by mixing antimicrobial agents during the manufacture of building materials [33]. The creation of a protective layer, in the form of a paint or coating, which is active against a wide range of microorganisms and stable over a wide pH range is more demanded in the construction field [34–36].

Thus, modern antibacterial coatings in the medical and food industries must meet such criteria as: efficiency, safety and durability. The review considers the main types of existing antibacterial coatings, mechanisms of action of coatings and their constituent components. Advantages and disadvantages for further design of future antimicrobial materials are evaluated.

TYPES OF ANTIBACTERIAL COATINGS

Over the past two decades, the attention of scientists and biomedical manufacturers has been focused on the development of coatings capable of resisting bacterial colonization that could be applied to various surfaces and devices [37, 38]. Antimicrobial coatings (Fig. 1), depending on their mechanism of action, are divided into: contact-type antimicrobial coatings [39–41] and release-based coatings, anti-adhesive antimicrobial coatings [42–45], multifunctional coatings [46–48], and smart antimicrobial coatings [49–51].

Earlier designs of antibacterial coatings for the strategy of preventing bacterial adhesion and subsequent biofilm formation were mostly monofunctional. They were based on the antibacterial effect inactivating microorganisms in contact with the surface or preventing their attachment [52, 53]. The first in this field were coatings with copper oxide, arsenic, mercury oxide and organoleaf derivatives that prevented biofouling of marine vessels [54, 55]. Since 1906, the development of anti-corrosion and anti-fouling paints for marine vessels based on zinc oxide and mercury oxide began [56]. In 1954 G.J.M. Der Van Kerk and J.G.A. Luijten showed biocidal properties of organotin compounds [57], which later became widespread as effective antifouling coatings. In 1995, polyurethane films containing quaternary ammonium compounds were developed, showing high biocidal activity against *Escherichia coli* [58] and polymer coatings modified with silver nitrate, which showed antibacterial effect against *Staphylococcus epidermidis* [59]. Lowe A.B. et al. in 2000 described a statistical copolymer of butyl acrylate with sulfobetaines, which when adsorbed on plastic disks reduced the adhesion of *Pseudomonas aeruginosa*, macrophages and fibroblasts [60].

Current coatings against bacterial contamination and fouling, focus on the synergistic combination of antibacterial and anti-adhesion effects in the form of multifunctional, smart coatings or interfacial materials [61]. The first example of a smart coating consisting of zwitterionic polymer derivatives that can rapidly switch their chemical structures and possess antibacterial, anti-adhesive properties and self-cleaning ability was described by Cheng G. et al., 2008 [62]. Subsequently, nanostructured coatings composed of temperature-sensitive poly N-isopropylacrylamide and quaternary ammonium salt were prepared by interferometric lithography and surface polymerization, which exhibit biocidal properties and the ability to release inactivated bacteria in response to temperature changes [63]. In 2018, a hybrid film was fabricated by successive deposition of a layer of gold nanoparticles and a phase transition lysozyme film, which had bactericidal activity under near-infrared laser irradiation, and its immersion in vitamin C promoted the removal of killed bacteria and surface regeneration [64]. In recent years, machine learning methods have been actively introduced in the development of various coatings. In 2021, a machine learning method (using an artificial neural network model and a model based on support vector regression) was developed to synthesize new anti-adhesive polymer brushes that demonstrated excellent resistance to protein adsorption at optimal film thickness [65].

Contact-type antibacterial coatings and antibacterial release coatings

Bactericidal coatings provide a reliable and simple way to prevent biofilm formation by exerting a biocidal effect on bacteria attached to the surface or suspended near the surface [5]. They are based on the introduction of antibacterial agents into the material or on its surface,

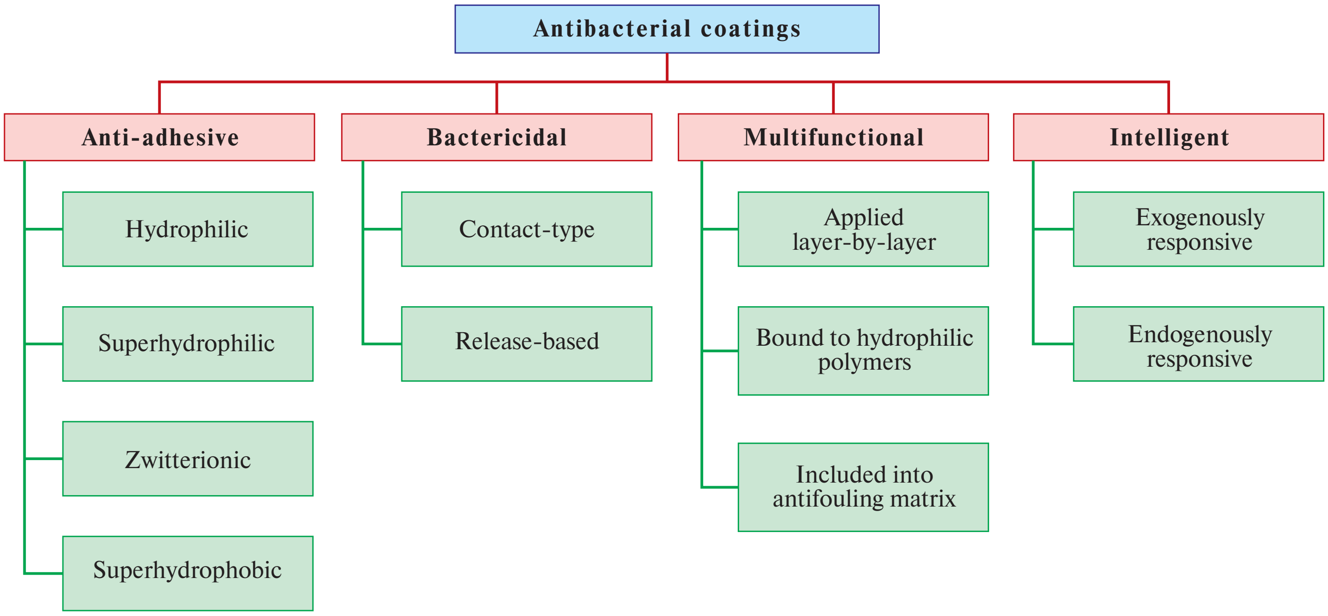

Fig. 1. Classification of the main types of antibacterial coatings.

which through gradual release of agents (Fig. 2b) or contact action (Fig. 2a) inactivate, damage or inhibit bacterial growth [66, 61]. Different biocides are fixed on the surface by dipping the coating in antimicrobial agent, spraying and centrifugation, and using layer-by-layer application technique or surface modification with different polymers [52]. Contact coatings can be divided into inorganic and organic coatings. Inorganic antimicrobial coatings are represented by nanoparticles of metals and their oxides (Ag, Au, Zn, Mg, and Cu) [67] and antibiotics (aminoglycosides, quinolones, penicillins, glycopeptides, tetracyclines, rifamycins) [68]. Organic antimicrobial coatings, are represented by quaternary ammonium salts (QAS) [69] and natural organic substances (antimicrobial peptides (AMP), enzymes and polysaccharides (chitosan)) [70–72]. Metal nanoparticles and their oxides are effective antibacterial agents because they can penetrate bacterial cells through ion channels and trigger the Fenton reaction with the formation of excess reactive oxygen species, increase bacterial cell wall permeability and oxidative stress in the bacterial cell body; can form secondary toxic metabolites, affecting the metabolic activity of bacteria; and induce changes in bacterial genetic information (e.g., 16S rDNA) [73]. Coatings, releasing antibiotics are able to deliver them directly to the site of action, thus providing higher efficacy and avoiding high dose antibiotic administration, systemic toxicity and development of drug resistance [74]. Antibiotics can inhibit bacterial cell protein synthesis, DNA replication and transcription by acting on DNA topoisomerases II and IV or by binding to RNA polymerase, disrupt cell wall peptidoglycan synthesis by enzymatic inhibition or by binding to amino acids [75, 76]. AMPs (Fig. 2c) are considered a promising candidate to replace conventional antibiotics because of their broad spectrum and nonspecific antibacterial mechanism of action [77]. They attach to the surface of the bacterial cell membrane, resulting in various forms of membrane damage; interfere with DNA and RNA synthesis and inhibit enzyme activity, causing bacterial death. In addition, AMPs exhibit excellent antibiofilm activity. Cationic molecules (e.g., QASs) can effectively kill bacteria through contact killing effect [78]. They can first adsorb on the bacterial cell wall through electrostatic action and then diffuse inward by disrupting the membrane potential, resulting in membrane damage, cytoplasmic leakage and bacterial death [73]. Chitosan and its derivatives exhibit antibacterial activity against fungi, Gram-positive and Gram-negative bacteria. The antibacterial activity of this polymer may be due to the interaction of amino groups of chitosan with the electronegative charges of the bacterial cell surface, resulting in the leakage of intracellular components [79]. It also exhibits biodegradability, biocompatibility, polymorphism and sorption properties [80]. Antibacterial enzymes are able to directly attack the microorganism, inhibit biofilm formation, degrade the biofilm, and/or catalyze reactions that lead to the production of antimicrobial compounds [81]. Release-based surfaces exhibit their antibacterial activity by releasing antibacterial agents by diffusion, erosion, degradation, or hydrolysis of covalent bonds into the environment [82]. The compounds are released from the surface of the material and the antibacterial activity occurs locally, only where it is needed. Depending on the antibacterial agent incorporated in the matrix, release-based coatings are capable of releasing antibiotics (penicillin, chlortetracycline, streptomycin, vancomycin), metal ions and oxides (Ag, Zn, and Cu) and non-metallic materials, fluorine (F) [83, 84, 27]. Polymethacrylic acid, polyacrylic acid, lactic and glycolic acid-based copolymers, hydroxyapatite, polyurethane, hyaluronic acid, chitosan, and ceramic nanoparticles are used as a carrier in such surfaces. Antibacterial release based surfaces are prepared by impregnating a porous material or coating with the desired antibacterial compound, by layer-by-layer application or by plasma spraying of polyelectorlites [85, 86, 52].

The main disadvantages of such coatings are the limited supply of antibacterial agents, which make the coatings unusable once they are depleted, and the toxicity of some antibacterial agents (QASs, nanoparticles and metal ions). Nanoparticles penetrate cells and subsequently exert toxic effects on intracellular structures. They cause mitochondrial damage, oxidative stress and autophagy [87, 88], and in high concentrations, cell necrosis and apoptosis [89]. Metal oxides (ZnO, MgO, CuO) are also cytotoxic and cause apoptosis, autophagy, oxidative stress and necrosis [90]. The accumulation of inactivated bacteria and intracellular components not only reduces coating efficacy, but can also promote biofilm formation [61] and induce immune reactions or inflammation. In addition, most biocidal agents are positively charged and can interact electrostatically with proteins. Moreover, different biocidal methods are based on different killing mechanisms and each method is effective for a specific type of bacteria. With the emergence of multidrug-resistant bacterial strains, approaches using a single killing mechanism are becoming less effective [5]. For example, silver-based materials have a strong bactericidal effect, but their activity decreases over time as the coatings continuously release the biocidal agent. In the case of polycationic polymer-based coatings, surface treatment with a cationic surfactant may be required to restore antimicrobial activity. Low molecular weight bactericidal agents often cause resistance and gradually lose their effectiveness over time [91].

Anti-adhesion antimicrobial coatings

Surface characteristics of materials, including surface charge, free energy, morphology, wettability, etc., have an important influence on bacterial adhesion [92]. Bacteria can attach to various surfaces and form biofilms through non-specific interactions such as hydrogen bonds, electrostatic forces, hydrophobic interactions, and van der Waals forces (Fig. 3a). Thus, bacterial adhesion on the surface of implanted devices contributes to device-associated infections and is the main reason for the development of anti-adhesion coatings [93]. To prevent the development of biofilms on biomaterial surfaces, the surface must be able to prevent initial bacterial adhesion [22]. Anti-adhesion coatings are functional coatings created by modifying the surface of materials by changing their physicochemical properties (roughness, degree of wettability, charge, etc.), which prevents the adhesion of bacteria, fungi and proteins (Fig. 3b) [94]. The action of such coatings is based on steric, electrostatic and superhydrophobic effects, which can be observed on hydrophilic, superhydrophilic, charged and superhydrophobic surfaces, respectively (Fig. 3c) [52]. Hydrophilic surfaces prevent the attachment of cells and bacteria due to the fact that they are covered by a layer of water molecules that are closely hydrogen bonded to the hydrophilic material and act as a physical and energetic barrier that must be overcome for adsorption. Hydrophilic polymers can also inhibit bacterial attachment to some extent, but high antifouling properties are acquired only when steric repulsion complements surface hydration [95]. Thus, highly hydrated polymers such as polyethylene glycol (PEG), neutral and hydrophilic polymers poly(2-alkyl-2-oxazoline) have demonstrated the ability to reduce bacterial and protein adhesion through steric hindrance [96, 97]. Hydrophilic coatings are prepared by physical, chemical adsorption, direct covalent attachment and block or grafted copolymerization [98]. Laser treatment of metal-based coatings with antibacterial properties makes it possible to obtain superhydrophilic coatings. In the zone of laser beam exposure the surface is heated and melting, sublimation and explosive ablation of the material takes place. At the same time, metal particles are removed from the surface and subsequently deposited, forming a micro-relief around the impact zone in the form of micro- and nanoparticles. Due to the high wettability of superhydrophilic coatings, the contact area is increased and metal ions from the formed nanoparticles are more efficiently transported into the liquid causing oxidative stress of bacterial cells. In addition, the formation of hierarchical surface porosity leads to bacterial death as a result of perforation and deformation of the membrane by the nanotexture elements and loss of intracellular fluid [99–101]. Compared to hydrophilic polymers, the interaction of bound water through ionic solvation is stronger than the hydrogen bonded water layer, which enhances the antifouling nature of zwitterionic surfaces [102]. Surfaces functionalized with zwitterionic polymers, which have a uniform distribution of anionic and cationic groups along their main chain in their structure, exhibit antifouling properties. These include polymethacryloyloxyethyl phosphorylcholine, polysulfobetainmethacrylate and polysulfobetainacrylamide as they contain cationic quaternary ammonium salt on the one hand and anionic carboxylate, phosphate and sulfate groups on the other hand, respectively [103]. In addition to the steric hindrance effect of this hydration layer, the cationic groups can also kill bacteria on contact. In addition, the surfaces functionalized with zwitterionic polymers are more versatile and stable regardless of temperature and salt concentration than PEG functionalization. Consequently, these polymers are widely used as antibacterial coatings [104]. Superhydrophobic surfaces have attracted much attention for their excellent self-cleaning properties and potential applications in various industries [105]. The water contact angle of such surfaces exceeds 150° and hence they are difficult to wet. The superhydrophobicity reduces the adhesion force between bacteria and the surface and facilitates the removal of

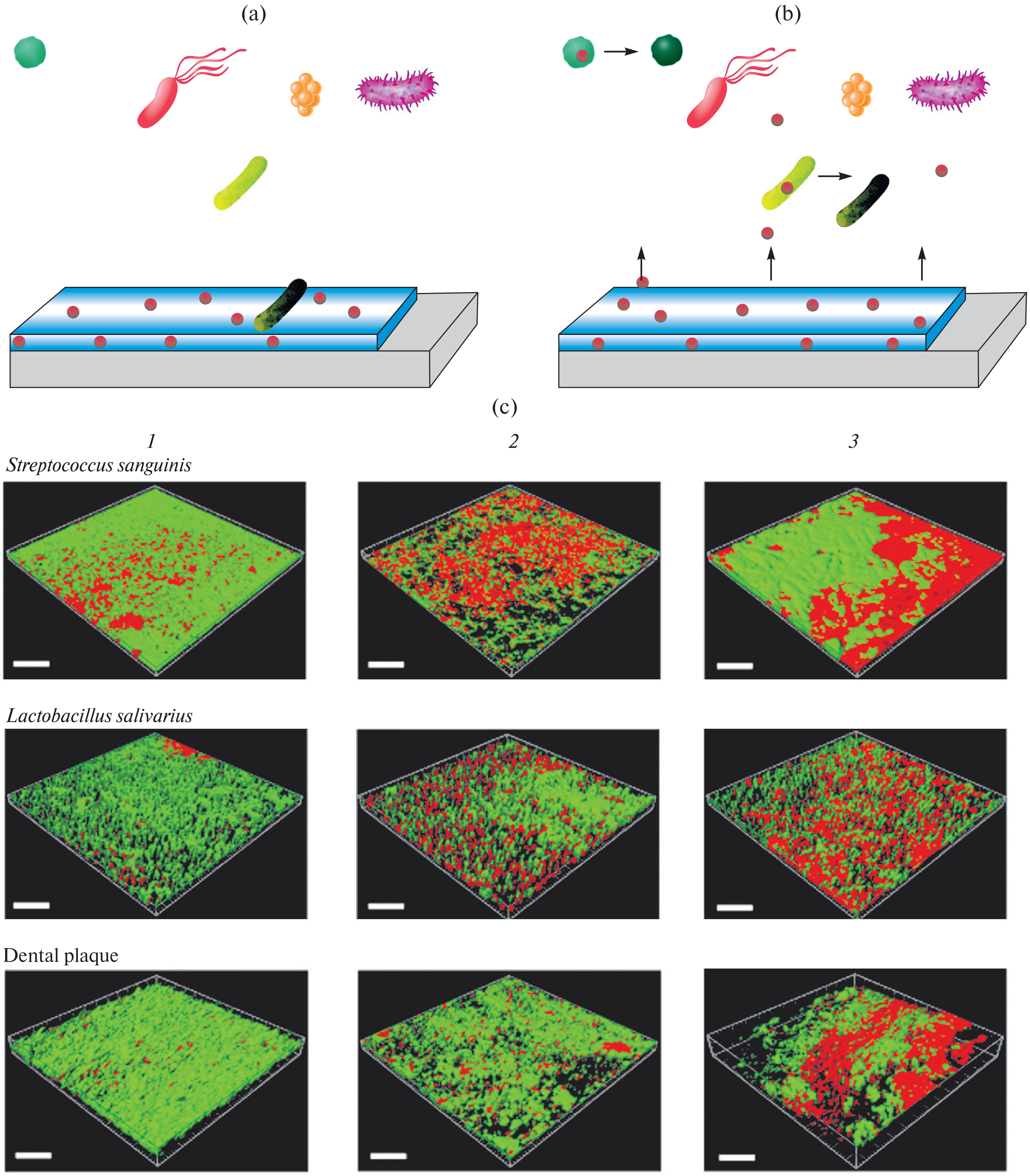

Fig. 2. a – Schematic representation of the mechanism of action of contact-type antibacterial coatings; b – Schematic representation of the mechanism of action of antibacterial coatings based on release; c – Images of viable cells (green) and dead bacteria (red) of *S. sanguinis*, *L. salivarius* and dental plaque obtained by confocal microscopy with 20x objective magnification after 4 weeks of incubation at 37°C (*1*) on titanium surface, (*2*) on titanium surface with silver electrodeposition, (*3*) on titanium surface coated with silane triethoxysilylpropylantharic anhydride, with immobilized hLf1-11 peptide. Reproduced from [39], with permission of the American Chemical Society, 2015.

initially adhered bacteria before biofilm formation [106, 52, 22]. This phenomenon is attributed to two physical principles: low surface energy and rough structures at the microscopic scale. Chemistry and surface topography are the main factors that interfere with interactions at the liquid–solid interface. Surface energy affects the adhesion of substances to the interface, including liquids and microorganisms. Low surface energy reduces the work of adhesion and hence increases hydrophobicity [107]. Superhydrophobic surfaces are achieved by preparing micro/nanostructures and then passivating them with low surface energy molecules [7]. The methods to obtain superhydrophobic antifouling coatings include chemical and physical etching, immersion method, sol-gel method, chemical vapor deposition, photolithography, centrifugation, electrospinning, layer-by-layer deposition, and/or a combination of these [108]. However, superior durability of functional properties for such surfaces is demonstrated by the laser texturing method [109, 110].

Antifouling coatings only prevent bacterial adhesion, not eliminate it (Fig. 3d). Therefore, over time there is an increase in the concentration of planktonic bacteria in the substrate, which contributes to bacterial contamination and leads to infections. In addition, hydrophilic polymers can be gradually neutralized, passivated or degraded by other compounds such as proteins, salts and amphiphiles. Any localized defects in superhydrophobic coatings can act as local adhesion sites for bacteria with subsequent biofilm formation.

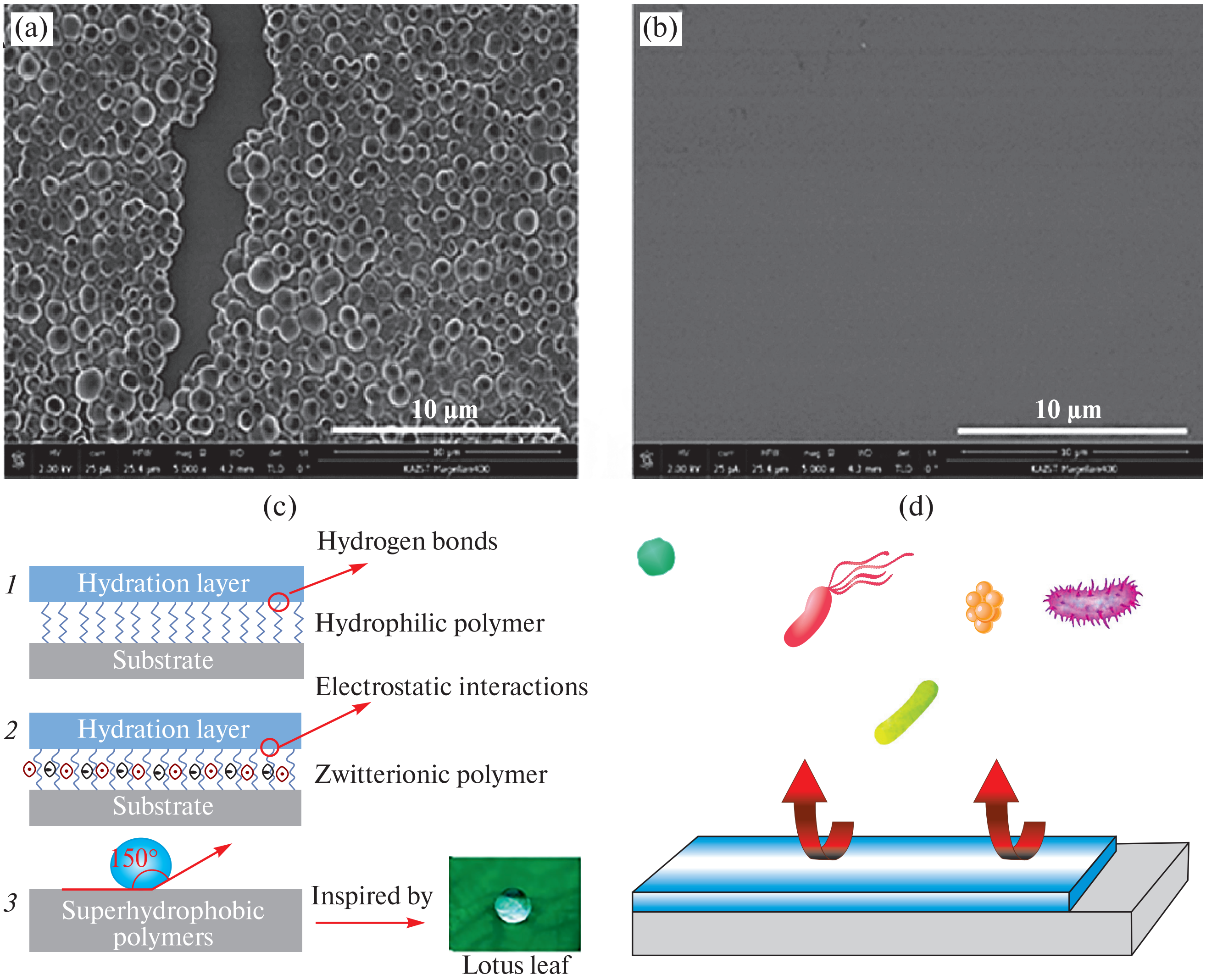

Fig. 3. a – Electron micrograph of a 7-day *S. aureus* biofilm on an uncoated surface; b – Electron micrograph of a polydodecyl methacrylate-polyethylene glycol methacrylate-acrylic acid coating preventing biofilm formation from *S. aureus* for 7 days. Reproduced from [43], with permission from the American Chemical Society, 2017; c – Schematic representations of anti-adhesion coatings. (*1*) Hydrophilic polymers, (*2*) zwitterionic coatings, (*3*) superhydrophobic coatings, water contact angle greater than 150° like in a lotus leaf. Reproduced from [93], with permission of John Wiley & Sons, Inc., 2020; d – Schematic representation of the mechanism of action of the anti-adhesion coating.

Multifunctional antimicrobial coatings

Advances in antibacterial and antifouling coatings have provided the basis for the development of multifunctional coatings [111–113]. They represent a class of antimicrobial materials that, in addition to inactivating bacteria, have additional capabilities such as long-term activity, stability, and recoverability. Various studies have shown that such coatings can reduce the number of bacteria on a surface by more than 99% compared to an uncoated surface [114–116]. The mechanism of action of multifunctional antibacterial coatings (Fig. 4a) includes: antibiofouling, bactericidal and removal of dead and/or live attached bacteria. Thus, the surface can resist or prevent the initial adhesion and spread of bacteria by steric and electrostatic repulsion or by reduced surface energy, and if bacteria make contact or partially attach to it, the bactericidal additives contained in the coatings destroy them (Fig. 4b, c) [117, 118]. Depending on the method used to incorporate antibacterial agents into anti-adhesion materials, such surfaces can be divided into three categories: bound to hydrophilic polymers, layer-by-layer applied or retained in and released from a non-fouling matrix. Natural and synthetic chemicals such as QASs compounds, antimicrobial enzymes, AMPs, chitosan and bacteriophages can be used as antibacterial agents [119]. Such coatings are prepared by sequential layer deposition, chemical modification, plasma deposition, covalent binding, conjugation, immobilization and graft polymerization [120].

Despite the high efficiency of multifunctional coatings, there are still many unsolved problems in the practice of their application and manufacture. Bactericidal agents included in the composition of such coatings have disadvantages related to storage stability, long-term effectiveness, biocompatibility, cost and labor intensity of their introduction into the coating composition. In addition, it is quite difficult to select materials for coating development that exhibit good biocidal activity, bacterial resistance properties and removal of dead bacteria. When using multifunctional coatings on medical devices, it is necessary to consider their composition, as it is not always the case that materials that combine antibacterial and anti-adhesive properties can be a universal means of combating bacterial infections. For example, the use of anti-adhesive materials is inadmissible in the manufacture of orthopedic and dental implants, because the surfaces must inhibit bacterial colonization and simultaneously promote osteoblast adhesion [121]. At the same time, the use of anti-adhesive materials in the fabrication of multifunctional coatings for urinary and intravascular catheters enhances the bactericidal properties of the surface because they do not require special conditions in addition to antibacterial properties [122]. Moreover, for practical applications, surface fabrication should be simple, inexpensive and reproducible. For objects in contact with seawater, it is essential that the surfaces demonstrate enhanced corrosion resistance and durability, as well as resistance to fouling by various organisms that may colonize any underwater surface [123]. It should be noted that for biomedical applications, the toxic effects of antibacterial surfaces need to be determined first and their biocompatibility improved [124].

Intelligent antimicrobial coatings

In recent years, smart antibacterial coatings have been developed that combine: anti-adhesion, bactericidal and self-cleaning functions, and realize controlled release

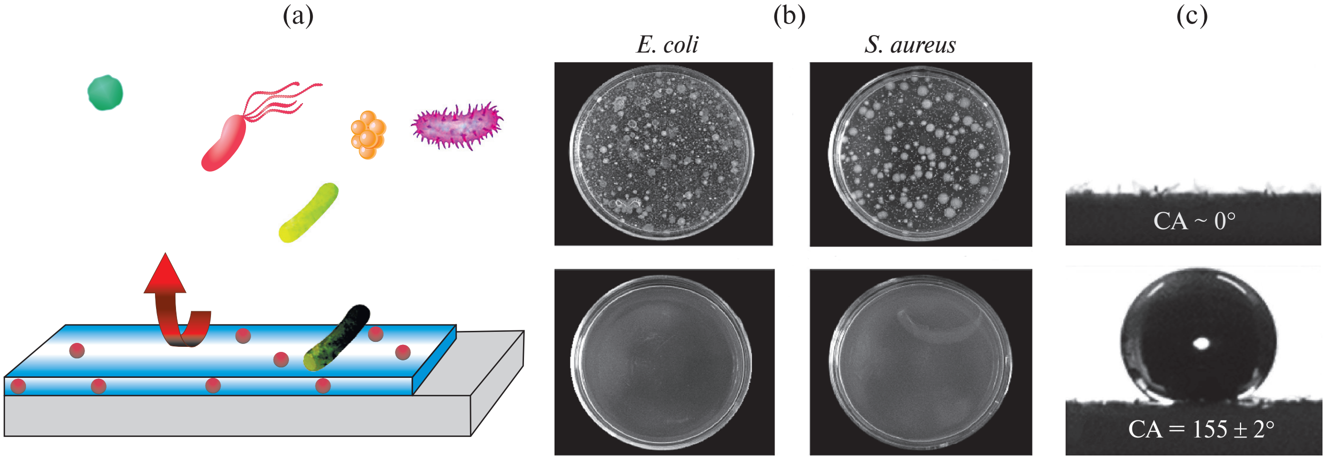

Fig. 4. a – Schematic representation of the mechanism of action of multifunctional antibacterial coating; b – Antibacterial activity of uncoated and coated cotton fabrics containing polyethylenimine, phytic acid, iron ion (Fe3+) and dimethyloctadecyl [3-trimethoxysilyl-propyl] ammonium chloride against *E. coli* and *S. aureus*, respectively; c – Optical images of water droplets placed on uncoated and coated cotton fabrics, respectively. *E. coli* and *S. aureus*, respectively; c – Optical images of water droplets placed on uncoated and multifunctional coated cotton fabrics, respectively. Reproduced from [48], with permission from Elsevier B.V., 2022.

of antibacterial agents through physical and chemical approaches, thereby achieving prolonged exposure, reducing potential side effects (Fig. 5a). Thus, smart antibacterial coatings are considered to be most optimal of all existing coatings. They can be categorized into endogenously and exogenously responsive types [125]. Endogenously responsive coatings primarily involve response to pH and bacterial secretions. The former is mainly stimulated through acidification of the medium by bacterial infection [126], whereas the latter refers to the response to various enzymes (such as phospholipase, hyaluronidase, cholesterol esterase and metalloprotease) or toxins secreted during the metabolic process [127, 128]. Conventional pH-sensitive coatings are produced by electrostatic interactions. For example, coatings containing negatively charged molecules and positively charged antibiotics are prepared by layer-by-layer self-assembly [129–132], or acid-sensitive Schiff bases [133, 134], metal coordination bonds [135], and boronic acid esters [136, 137] are used for synthesis. In addition, pH-sensitive coatings can be derived from reactive binding between nanoparticles and drugs, as well as sensitive molecules such as polymethacrylic acid [138]. Exogenously stimulated coatings exhibit antibacterial activity when stimulated by external conditions. Such coatings can solve the problems of poor stability, uncontrolled drug release and emergence of bacterial resistance. Exogenously sensitive coatings include temperature responsive surfaces,

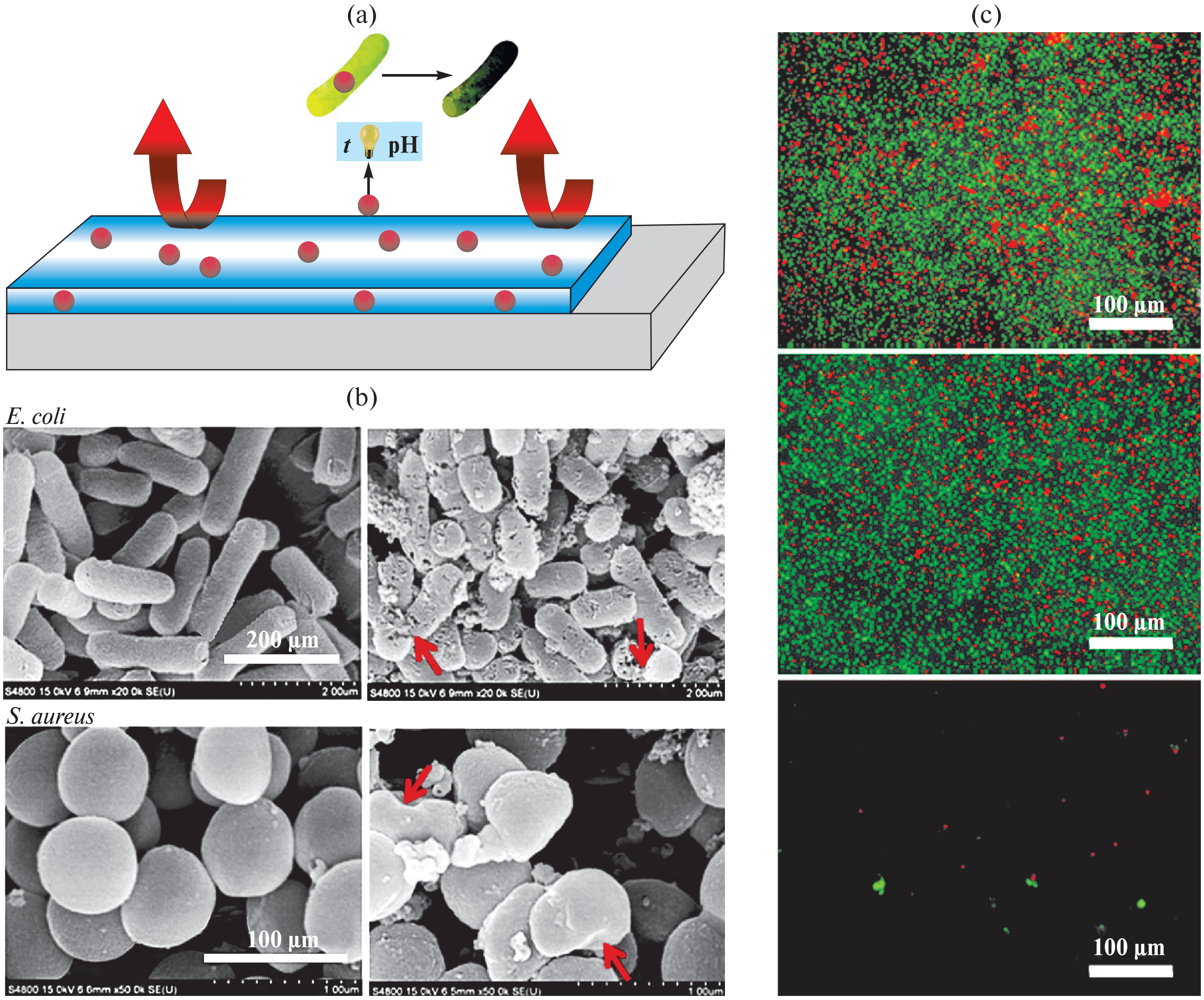

Fig. 5. a – Schematic representation of the mechanism of action of the smart antibacterial coating; b – Electron micrographs of *E. coli* and *S. aureus* cultured with carbon capsules modified with polyethylene glycol and doped with nitrogen with and without 808 nm laser irradiation. Reproduced from [138], with permission from the American Chemical Society, 2018; c – Confocal microscopy images of viable cells (green) and dead bacteria (red) of *S. aureus* obtained using confocal microscopy of uncoated 3D nanoporous surface, tannic acid-coated 3D nanoporous surface, tannic acid and gentamicin-coated 3D nanoporous surface, respectively. Reproduced from [129], with permission from the American Chemical Society, 2015.

photosensitive surfaces that are activated by light and bioelectric surfaces that are activated by an external electric field [139–141]. Such coatings are obtained by covalent bonding, vapor deposition, multilayer films or hydrogel coatings containing enzyme-sensitive components, photopolymerization, or a combination of several methods [127].

The analysis of the conducted studies indicates a great potential of smart antibacterial coatings for practical applications, but there is a lot of room for improvement of current coating methods to make them more effective, versatile and cost-effective. Promising in this direction would be the development of smart coatings that have the ability to activate biocidal activity in response to changes in certain biological microenvironments, as well as improving their stability, durability and reducing cytotoxicity [142].

CONCLUSION

In the last decades, active research has been conducted to improve antibacterial coatings and give them new properties such as the ability to regenerate and clean up dead bacteria. In addition, the combination of several antibacterial agents or the combination of different types of antibacterial coatings improve their effectiveness and durability. For example, in multifunctional materials where more than one protection strategy (superhydrophobic and anti-adhesive) incorporated into the coatings, bacterial adhesion is more effectively prevented, and if the compositions contain released antimicrobial agents, microbial cells will be inactivated upon contact with them. In addition, the need and use of an antimicrobial agent is reduced, and the service life of such a coating can be significantly longer than that of contact-type antimicrobial surfaces. Smart coatings based on the activation of antibacterial agents in response to changing environmental factors make surfaces even more effective durable, environmentally friendly, and in demand. Thus, further research on next-generation antibacterial coatings should focus on finding new and extending existing mechanisms of action against bacteria and developing additional pathways for their activation, as well as obtaining surfaces with multiple integrated functions.

The field of antimicrobial and antifouling surface development is a promising one and the potential for large and rapid impact through the implementation of developed technologies is evident. A large number of developments and studies described in the literature in the field of antimicrobial coatings do not reach practical application or even clinical trials. This is due to the fact that in laboratory conditions for testing antibacterial materials it is difficult to create conditions that occur in living organisms. The use of artificial intelligence and digital tools can help solve these problems. Thus analytical tools help to quickly and accurately process and analyze huge amounts of data, and artificial intelligence, by analyzing the chemical structure of coatings, helps to determine the toxicity of materials and select compounds for inclusion, saving time, resources and minimizing the risks of adverse effects in clinical trials.

FUNDING

The research was carried out under the grant of the Russian Science Foundation and the Academy of Sciences of the Republic of Tatarstan under the project No. 24-26-20074.

ETHICS DECLARATION

There are no human or animal studies in this paper.

CONFLICT OF INTERESTS

The authors declare that they have no conflict of interests.

REFERENCES

1. *Jiang C.C., Cao Y.K., Xiao G.Y. et al.* A review on the application of inorganic nanoparticles in chemical surface coatings on metallic substrates // RSC Advances. 2017. Vol. 7. No. 13. Pp. 7531–7539. https://doi.org/10.1039/C6RA25841G
2. *Kausar A.* Polymer coating technology for high performance applications: Fundamentals and advances // Journal of Macromolecular Science, Part A. 2018. Vol. 55. No. 5. Pp. 440–448. https://doi.org/10.1080/10601325.2018.1453266
3. *Makvandi P., Wang C.Y., Zare E.N. et al.* Metal-based nanomaterials in biomedical applications: Antimicrobial activity and cytotoxicity aspects // Advanced Functional Materials. 2020. Vol. 30. No. 22. P. 1910021. https://doi.org/10.1002/adfm.201910021
4. *Erkoc P., Ulucan-Karnak F.* Nanotechnology-based antimicrobial and antiviral surface coating strategies // Prosthesis. 2021. Vol. 3. No. 1. Pp. 25–52. https://doi.org/10.3390/prosthesis3010005
5. *Wei T., Yu Q., Chen H.* Responsive and synergistic antibacterial coatings: Fighting against bacteria in a smart and effective way // Advanced Healthcare Materials. 2019. Vol. 8. No. 3. P. 18001381. https://doi.org/10.1002/adhm.201801381
6. *DeFlorio W., Liu S., White A.R. et al.* Recent developments in antimicrobial and antifouling coatings to reduce or prevent contamination and cross-contamination of food contact surfaces by bacteria // Comprehensive Reviews in Food Science and Food Safety. 2021. Vol. 20. No. 3. Pp. 3093–3134. https://doi.org/10.1111/1541-4337.12750
7. *Wang L., Guo X., Zhang H. et al.* Recent advances in superhydrophobic and antibacterial coatings for biomedical materials // Coatings. 2022. Vol. 12. No. 10. P. 1469. https://doi.org/10.3390/coatings12101469

8. *Rezić I., Meštrović E.* Characterization of nanoparticles in antimicrobial coatings for medical applications — A review // Coatings. 2023. Vol. 13. No. 11. P. 1830. https://doi.org/10.3390/coatings13111830
9. *Blair J.M., Webber M.A., Baylay A.J. et al.* Molecular mechanisms of antibiotic resistance // Nature reviews microbiology. 2015. Vol. 13. No. 1. Pp. 42–51. https://doi.org/10.1038/nrmicro3380
10. *Davidovich N.V., Kukalevskaya N.N., Bashilova E.N., Bazhukova T.A.* Basic principles of the evolution of antibiotic resistance in bacteria (literature review) // Klinicheskaya laboratornaya diagnostika. 2020. Vol. 65. No. 6. Pp. 387–393. http://dx.doi.org/10.18821/0869-2084-2020-65-6-387-393
11. *Urban-Chmiel R., Marek A., Stępień-Pyśniak D. et al.* Antibiotic resistance in bacteria — A review // Antibiotics. 2022. Vol. 11. No. 8. P. 1079. https://doi.org/10.3390/antibiotics11081079
12. *Cherednichenko Y., Batasheva S., Akhatova F. et al.* Antibiofilm activity of silver nanoparticles-halloysite nanocomposite in Serratia marcescens // Journal of Nanoparticle Research. 2024. Vol. 26. No. 4. P. 71. https://doi.org/10.1007/s11051-024-05971-y
13. *Stewart P.S., Costerton J.W.* Antibiotic resistance of bacteria in biofilms // The Lancet. 2001. Vol. 358. No. 9276. Pp. 135–138. https://doi.org/10.1016/S0140-6736(01)05321-1
14. *Chebotar I.V., Mayansky A.N., Konchakova E.D. et al.* Antibiotic resistance of biofilm bacteria // Clinical microbiology and antimicrobial chemotherapy. 2012. Vol. 14. No. 1. Pp. 51–58.
15. *De Silva R.T., Pasbakhsh P., Lee S.M., Kit A.Y.* ZnO deposited / Encapsulated halloysite–poly (lactic acid) (PLA) nanocomposites for high performance packaging films with improved mechanical and antimicrobial properties // Applied Clay Science. 2015. Vol. 111. Pp. 10–20. https://doi.org/10.1016/j.clay.2015.03.024
16. *Karthikeyan P., Mitu L., Pandian K. et al.* Electrochemical deposition of a Zn-HNT / P (EDOT-co-EDOP) nanocomposite on LN SS for anti-bacterial and anti-corrosive applications // New Journal of Chemistry. 2017. Vol. 41. No. 12. Pp. 4758–4762. https://doi.org/10.1039/C6NJ03927H
17. *Stavitskaya A., Batasheva S., Vinokurov V. et al.* Antimicrobial applications of clay nanotube-based composites // Nanomaterials. 2019. Vol. 9. No. 5. P. 708. https://doi.org/10.3390/nano9050708
18. *Mauriello G.* Chapter 11 — Control of microbial activity using antimicrobial packaging // Barros-Velazquez J. (ed). Antimicrobial Food Packaging. London, San Diego, USA: Academic Press. 2016. Pp. 141–152. https://doi.org/10.1016/B978-0-12-800723-5.00011-5
19. *Valencia-Chamorro S.A., Palou L., Del Río M.A., Pérez-Gago M.B.* Antimicrobial edible films and coatings for fresh and minimally processed fruits and vegetables: A review // Critical Reviews in Food Science and Nutrition. 2011. Vol. 51. No. 9. Pp. 872–900. https://doi.org/10.1080/10408398.2010.485705
20. *Malhotra B., Keshwani A., Kharkwal H.* Antimicrobial food packaging: Potential and pitfalls // Frontiers in microbiology. 2015. Vol. 6. P. 611. https://doi.org/10.3389/fmicb.2015.00611
21. *Fu Y., Dudley E.G.* Antimicrobial-coated films as food packaging: A review // Comprehensive Reviews in Food Science and Food Safety. 2021. Vol. 20. No. 4. Pp. 3404–3437. https://doi.org/10.1111/1541-4337.12769
22. *Pemmada R., Shrivastava A., Dash M. et al.* Science-based strategies of antibacterial coatings with bactericidal properties for biomedical and healthcare settings // Current Opinion in Biomedical Engineering. 2023. Vol. 25. P. 100442. https://doi.org/10.1016/j.cobme.2022.100442
23. *Paladini F., Pollini M., Sannino A., Ambrosio L.* Metal-based antibacterial substrates for biomedical applications // Biomacromolecules. 2015. Vol. 16. No. 7. Pp. 1873–1885. https://doi.org/10.1021/acs.biomac.5b00773
24. *Jose A., Gizdavic-Nikolaidis M., Swift S.* Antimicrobial coatings: reviewing options for healthcare applications // Applied Microbiology. 2023. Vol. 3. No. 1. Pp. 145–174. https://doi.org/10.3390/applmicrobiol3010012
25. *Adlhart C., Verran J., Azevedo N.F. et al.* Surface modifications for antimicrobial effects in the healthcare setting: A critical overview // Journal of Hospital Infection. 2018. Vol. 99. No. 3. Pp. 239–249. https://doi.org/10.1016/j.jhin.2018.01.018
26. *Simchi A., Tamjid E., Pishbin F., Boccaccini A.R.* Recent progress in inorganic and composite coatings with bactericidal capability for orthopaedic applications // Nanomedicine: Nanotechnology, Biology and Medicine. 2011. Vol. 7. No. 1. Pp. 22–39. https://doi.org/10.1016/j.nano.2010.10.005
27. *Chen X., Zhou J., Qian Y., Zhao L.* Antibacterial coatings on orthopedic implants // Materials Today Bio. 2023. Vol. 19. P. 100586. https://doi.org/10.1016/j.mtbio.2023.100586
28. *Andra S., Balu S.K., Jeevanandam J., Muthalagu M.* Emerging nanomaterials for antibacterial textile fabrication // Naunyn-Schmiedeberg's Archives of Pharmacology. 2021. Vol. 394. Pp. 1355–1382. https://doi.org/10.1007/s00210-021-02064-8
29. *Dastjerdi R., Montazer M.* A review on the application of inorganic nano-structured materials in the modification of textiles: Focus on anti-microbial properties // Colloids and Surfaces B: Biointerfaces. 2010. Vol. 79. No. 1. Pp. 5–18. https://doi.org/10.1016/j.colsurfb.2010.03.029
30. *Aguda O.N., Lateef A.* Recent advances in functionalization of nanotextiles: A strategy to combat harmful microorganisms and emerging pathogens in the 21st century // Heliyon. 2022. Vol. 8. No. 6. P. e09761. https://doi.org/10.1016/j.heliyon.2022.e09761

31. *Hochmannova L., Vytrasova J.* Photocatalytic and antimicrobial effects of interior paints // Progress in Organic Coatings. 2010. Vol. 67. No. 1. Pp. 1–5. https://doi.org/10.1016/j.porgcoat.2009.09.016
32. *Kocer H.B., Cerkez I., Worley S.D. et al.* N-halamine copolymers for use in antimicrobial paints // ACS Applied Materials & Interfaces. 2011. Vol. 3. No. 8. Pp. 3189–3194. https://doi.org/10.1021/am200684u
33. *Kirthika S.K., Goel G., Matthews A., Goel S.* Review of the untapped potentials of antimicrobial materials in the construction sector // Progress in Materials Science. 2023. Vol. 133. P. 101065. https://doi.org/10.1016/j.pmatsci.2022.101065
34. *Gupta S., Puttaiahgowda Y.M., Nagaraja A., Jalageri M.D.* Antimicrobial polymeric paints: An up-to-date review // Polymers for Advanced Technologies. 2021. Vol. 32. No. 12. Pp. 4642–4662. https://doi.org/10.1002/pat.5485
35. *Tornero A.F., Blasco M.G., Azqueta M.C. et al.* Antimicrobial ecological waterborne paint based on novel hybrid nanoparticles of zinc oxide partially coated with silver // Progress in Organic Coatings. 2018. Vol. 121. Pp. 130–141. https://doi.org/10.1016/j.porgcoat.2018.04.018
36. *Bakina O., Pikuschak E., Prokopchuk A. et al.* Enhanced Biocidal Activity of Heterophase Zinc Oxide/Silver Nanoparticles Contained within Painted Surfaces // Coatings. 2024. Vol. 14. No. 2. P. 241. https://doi.org/10.3390/coatings14020241
37. *Vasilev K., Cook J., Griesser H.J.* Antibacterial surfaces for biomedical devices // Expert Review of Medical Devices. 2009. Vol. 6. No. 5. Pp. 553–567. https://doi.org/10.1586/erd.09.36
38. *Cavallaro A., Taheri S., Vasilev K.* Responsive and “smart” antibacterial surfaces: Common approaches and new developments // Biointerphases. 2014. Vol. 9. No. 2. P. 029005. https://doi.org/10.1116/1.4866697
39. *Godoy-Gallardo M., Wang Z., Shen Y. et al.* Antibacterial coatings on titanium surfaces: A comparison study between in vitro single-species and multispecies biofilm // ACS Applied Materials & Interfaces. 2015. Vol. 7. No. 10. Pp. 5992–6001. https://doi.org/10.1021/acsami.5b00402
40. *Bharadishettar N., Bhat K.U., Bhat Panemangalore D.* Coating technologies for copper based antimicrobial active surfaces: A perspective review // Metals. 2021. Vol. 11. No. 5. P. 711. https://doi.org/10.3390/met11050711
41. *Ferreira T.P.M., Nepomuceno N.C., Medeiros E.L. et al.* Antimicrobial coatings based on poly (dimethyl siloxane) and silver nanoparticles by solution blow spraying // Progress in Organic Coatings. 2019. Vol. 133. Pp. 19–26. https://doi.org/10.1016/j.porgcoat.2019.04.032
42. *Yu K., Lo J.C., Yan M. et al.* Anti-adhesive antimicrobial peptide coating prevents catheter associated infection in a mouse urinary infection model // Biomaterials. 2017. Vol. 116. Pp. 69–81. https://doi.org/10.1016/j.biomaterials.2016.11.047
43. *Keum H., Kim J.Y., Yu B. et al.* Prevention of bacterial colonization on catheters by a one-step coating process involving an antibiofouling polymer in water // ACS Applied Materials & Interfaces. 2017. Vol. 9. No. 23. Pp. 19736–19745. https://doi.org/10.1021/acsami.7b06899
44. *Li X., Li P., Saravanan R. et al.* Antimicrobial functionalization of silicone surfaces with engineered short peptides having broad spectrum antimicrobial and salt-resistant properties // Acta Biomaterialia. 2014. Vol. 10. No. 1. Pp. 258–266. https://doi.org/10.1016/j.actbio.2013.09.009
45. *Banerjee I., Pangule R.C., Kane R.S.* Antifouling coatings: recent developments in the design of surfaces that prevent fouling by proteins, bacteria, and marine organisms // Advanced Materials. 2011. Vol. 23. No. 6. Pp. 690–718. https://doi.org/10.1002/adma.201001215
46. *Raphel J., Holodniy M., Goodman S.B., Heilshorn S.C.* Multifunctional coatings to simultaneously promote osseointegration and prevent infection of orthopaedic implants // Biomaterials. 2016. Vol. 84. Pp. 301–314. https://doi.org/10.1016/j.biomaterials.2016.01.016
47. *Liao T.Y., Easton C.D., Thissen H., Tsai W.B.* Aminomalononitrile-assisted multifunctional antibacterial coatings // ACS Biomaterials Science & Engineering. 2020. Vol. 6. No. 6. Pp. 3349–3360. https://doi.org/10.1021/acsbiomaterials.0c00148
48. *Li C.B., Wang F., Sun R.Y. et al.* A multifunctional coating towards superhydrophobicity, flame retardancy and antibacterial performances // Chemical Engineering Journal. 2022. Vol. 450. P. 138031. https://doi.org/10.1016/j.cej.2022.138031
49. *Ni X., Li C., Lei Y. et al.* Design of a smart self-healing coating with multiple-responsive superhydrophobicity and its application in antibiofouling and antibacterial abilities // ACS Applied Materials & Interfaces. 2021. Vol. 13. No. 48. Pp. 57864–57879. https://doi.org/10.1021/acsami.1c15239
50. *Li X., Wu B., Chen H. et al.* Recent developments in smart antibacterial surfaces to inhibit biofilm formation and bacterial infections // Journal of Materials Chemistry B. 2018. Vol. 6. No. 26. Pp. 4274–4292. https://doi.org/10.1039/C8TB01245H
51. *Wei T., Yu Q., Zhan W., Chen H.* A smart antibacterial surface for the on-demand killing and releasing of bacteria // Advanced Healthcare Materials. 2016. Vol. 5. No. 4. Pp. 449–456. https://doi.org/10.1002/adhm.201500700
52. *Olmo JA-D., Ruiz-Rubio L., Pérez-Alvarez L. et al.* Antibacterial coatings for improving the performance of biomaterials // Coatings. 2020. Vol. 10. No. 2. P. 139. https://doi.org/10.3390/coatings10020139

53. *Jose A., Gizdavic-Nikolaidis M., Swift S.* Antimicrobial coatings: Reviewing options for healthcare applications // Applied Microbiology. 2023. Vol. 3. No. 1. Pp. 145–174. https://doi.org/10.3390/applmicrobiol3010012
54. *Yebra D.M., Kiil S., Dam-Johansen K.* Antifouling technology – Past, present and future steps towards efficient and environmentally friendly antifouling coatings // Progress in Organic Coatings. 2004. Vol. 50. No. 2. Pp. 75–104. https://doi.org/10.1016/j.porgcoat.2003.06.001
55. *Li L., Hong H., Cao J., Yang Y.* Progress in marine antifouling coatings: Current status and prospects // Coatings. 2023. Vol. 13. No. 11. P. 1893. https://doi.org/10.3390/coatings13111893
56. *Francis W.J.* Shipbottom paints. Past, present and future research and development on anticorrosive and antifouling shipbottom compositions // Journal of the American Society for Naval Engineers. 1954. Vol. 66. No. 4. Pp. 857–866. https://doi.org/10.1111/j.1559-3584.1954.tb05931.x
57. *Van Kerk G.J.M.D., Luijten J.G.A.* Investigations on organo-tin compounds. III. The biocidal properties of organo-tin compounds //Journal of Applied Chemistry. 1954. Vol. 4. No. 6. Pp. 314–319. https://doi.org/10.1002/jctb.5010040607
58. *Hazziza-Laskar J., Helary G., Sauvet G.* Biocidal polymers active by contact. IV. Polyurethanes based on polysiloxanes with pendant primary alcohols and quaternary ammonium groups // Journal of Applied Polymer Science. 1995. Vol. 58. No. 1. Pp. 77–84. https://doi.org/10.1002/app.1995.070580108
59. *Jansen B., Kohnen W.* Prevention of biofilm formation by polymer modification // Journal of Industrial Microbiology. 1995. Vol. 15. No. 4. Pp. 391–396. https://doi.org/10.1007/BF01569996
60. *Lowe A.B., Vamvakaki M., Wassall M.A. et al.* Well-defined sulfobetaine-based statistical copolymers as potential antibioadherent coatings // Journal of Biomedical Materials Research. 2000. Vol. 52. No. 1. Pp. 88–94. https://doi.org/10.1002/1097-4636(200010)52:1%3C88::AID-JBM11%3E3.0.CO;2-%23
61. *Mu M., Wang X., Taylor M. et al.* Multifunctional coatings for mitigating bacterial fouling and contamination // Colloid and Interface Science Communications. 2023. Vol. 55. P. 100717. https://doi.org/10.1016/j.colcom.2023.100717
62. *Cheng G., Xue H., Zhang Z. et al.* A switchable biocompatible polymer surface with self-sterilizing and nonfouling capabilities // Angewandte Chemie International Edition. 2008. Vol. 47. No. 46. Pp. 8831–8834. https://doi.org/10.1002/anie.200803570
63. *Yu Q., Cho J., Shivapooja P. et al.* Nanopatterned smart polymer surfaces for controlled attachment, killing, and release of bacteria // ACS Applied Materials & Interfaces. 2013. Vol. 5. No. 19. Pp. 9295–9304. https://doi.org/10.1021/am4022279
64. *Qu Y., Wei T., Zhao J. et al.* Regenerable smart antibacterial surfaces: Full removal of killed bacteria via a sequential degradable layer // Journal of Materials Chemistry B. 2018. Vol. 6. No. 23. Pp. 3946–3955. https://doi.org/10.1039/C8TB01122B
65. *Liu Y., Zhang D., Tang Y. et al.* Machine learning-enabled repurposing and design of antifouling polymer brushes //Chemical Engineering Journal. 2021. Vol. 420. P. 129872. https://doi.org/10.1016/j.cej.2021.129872
66. *Kaur R., Liu S.* Antibacterial surface design – Contact kill // Progress in Surface Science. 2016. Vol. 91. No. 3. Pp. 136–153. https://doi.org/10.1016/j.progsurf.2016.09.001
67. *Nasri N., Rusli A., Teramoto N. et al.* Past and current progress in the development of antiviral / Antimicrobial polymer coating towards COVID-19 prevention: A Review // Polymers. 2021. Vol. 13. No. 23. P. 4234. https://doi.org/10.3390/polym13234234
68. *Pan C., Zhou Z., Yu X.* Coatings as the useful drug delivery system for the prevention of implant-related infections // Journal of Orthopaedic Surgery and Research. 2018. Vol. 13. P. 220. https://doi.org/10.1186/s13018-018-0930-y
69. *Elena P., Miri K.* Formation of contact active antimicrobial surfaces by covalent grafting of quaternary ammonium compounds // Colloids and Surfaces B: Biointerfaces. 2018. Vol. 169. Pp. 195–205. https://doi.org/10.1016/j.colsurfb.2018.04.065
70. *Yu K., Alzahrani A., Khoddami S. et al.* Rapid assembly of infection-resistant coatings: Screening and identification of antimicrobial peptides works in cooperation with an antifouling background // ACS Applied Materials & Interfaces. 2021. Vol. 13. No. 31. Pp. 36784–36799. https://doi.org/10.1021/acsami.1c07515
71. *Alves D., Olívia Pereira M.* Mini-review: Antimicrobial peptides and enzymes as promising candidates to functionalize biomaterial surfaces // Biofouling. 2014. Vol. 30. No. 4. Pp. 483–499. https://doi.org/10.1080/08927014.2014.889120
72. *Qu B., Luo Y.* A review on the preparation and characterization of chitosan-clay nanocomposite films and coatings for food packaging applications // Carbohydrate Polymer Technologies and Applications. 2021. Vol. 2. P. 100102. https://doi.org/10.1016/j.carpta.2021.100102
73. *Li W., Thian E.S., Wang M. et al.* Surface design for antibacterial materials: From fundamentals to advanced strategies // Advanced Science. 2021. Vol. 8. No. 19. P. 2100368. https://doi.org/10.1002/advs.202100368
74. *Shahid A., Aslam B., Muzammil S. et al.* The prospects of antimicrobial coated medical implants // Journal of Applied Biomaterials & Functional Materials. 2021.

Vol. 19. P. 22808000211040304.
https://doi.org/10.1177/22808000211040304

75. *Campoccia D., Montanaro L., Arciola C.R.* A review of the biomaterials technologies for infection-resistant surfaces // Biomaterials. 2013. Vol. 34. No. 34. Pp. 8533–8554.
https://doi.org/10.1016/j.biomaterials.2013.07.089
76. *Zilberman M., Elsner J.J.* Antibiotic-eluting medical devices for various applications // Journal of Controlled Release. 2008. Vol. 130. No. 3. Pp. 202–215.
https://doi.org/10.1016/j.jconrel.2008.05.020
77. *Batoni G., Maisetta G., Esin S.* Antimicrobial peptides and their interaction with biofilms of medically relevant bacteria // Biochimica et Biophysica Acta (BBA) – Biomembranes. 2016. Vol. 1858. No. 5. Pp. 1044–1060.
https://doi.org/10.1016/j.bbamem.2015.10.013
78. *Chen R., Shi C., Xi Y. et al.* Fabrication of cationic polymer surface through plasma polymerization and layer-by-layer assembly // Materials and Manufacturing Processes. 2020. Vol. 35. No. 2. Pp. 221–229.
https://doi.org/10.1080/10426914.2019.1675892
79. *Li J., Zhuang S.* Antibacterial activity of chitosan and its derivatives and their interaction mechanism with bacteria: Current state and perspectives // European Polymer Journal. 2020. Vol. 138. P. 109984.
https://doi.org/10.1016/j.eurpolymj.2020.109984
80. *Wrońska N., Katir N., Miłowska K. et al.* Antimicrobial effect of chitosan films on food spoilage bacteria // International Journal of Molecular Sciences. 2021. Vol. 22. No. 11. P. 5839.
https://doi.org/10.3390/ijms22115839
81. *Thallinger B., Prasetyo E.N., Nyanhongo G.S., Guebitz G.M.* Antimicrobial enzymes: an emerging strategy to fight microbes and microbial biofilms // Biotechnology Journal. 2013. Vol. 8. No. 1. Pp. 97–109.
https://doi.org/10.1002/biot.201200313
82. *Campoccia D., Montanaro L., Arciola C.R.* A review of the biomaterials technologies for infection-resistant surfaces //Biomaterials. 2013. Vol. 34. No. 34. Pp. 8533–8554.
https://doi.org/10.1016/j.biomaterials.2013.07.089
83. *Hickok N.J., Shapiro I.M.* Immobilized antibiotics to prevent orthopaedic implant infections // Advanced drug delivery reviews. 2012. Vol. 64. No. 12. Pp. 1165–1176.
https://doi.org/10.1016/j.addr.2012.03.015
84. *Cooper L.F., Zhou Y., Takebe J. et al.* Fluoride modification effects on osteoblast behavior and bone formation at TiO2 grit-blasted cp titanium endosseous implants // Biomaterials. 2006. Vol. 27. No. 6. Pp. 926–936.
https://doi.org/10.1016/j.biomaterials.2005.07.009
85. *Valverde A., Pérez-Álvarez L., Ruiz-Rubio L. et al.* Antibacterial hyaluronic acid/chitosan multilayers onto smooth and micropatterned titanium surfaces // Carbohydrate polymers. 2019. Vol. 207. Pp. 824–833.
https://doi.org/10.1016/j.carbpol.2018.12.039
86. *Lv H., Chen Z., Yang X. et al.* Layer-by-layer self-assembly of minocycline-loaded chitosan/alginate multilayer on titanium substrates to inhibit biofilm formation //Journal of dentistry. 2014. Vol. 42. No. 11. Pp. 1464–1472.
https://doi.org/10.1016/j.jdent.2014.06.003
87. *Li K., Zhao X.K., Hammer B.K., Du S., Chen Y.* Nanoparticles inhibit DNA replication by binding to DNA: Modeling and experimental validation // ACS Nano. 2013. Vol. 7. No. 11. Pp. 9664–9674.
https://doi.org/10.1002/biot.201200313
88. *Gorbachevskii M.V., Stavitskaya A.V., Novikov A.A. et al.* Fluorescent gold nanoclusters stabilized on halloysite nanotubes: in vitro study on cytotoxicity // Applied Clay Science. 2021. Vol. 207. P. 106106.
https://doi.org/10.1016/j.clay.2021.106106
89. *Iskuzhina L., Batasheva S., Kryuchkova M. et al.* Advances in the Toxicity Assessment of Silver Nanoparticles derived from a Sphagnum fallax extract for Monolayers and Spheroids // Biomolecules. 2024. Vol. 14. No. 6. P. 611.
https://doi.org/10.3390/biom14060611
90. *Mohammadinejad R., Moosavi M.A., Tavakol S. et al.* Necrotic, apoptotic and autophagic cell fates triggered by nanoparticles //Autophagy. 2019. Vol. 15. No. 1. Pp. 4–33.
https://doi.org/10.1080/15548627.2018.1509171
91. *Pangule R.C., Brooks S.J., Dinu C.Z. et al.* Antistaphylococcal nanocomposite films based on enzyme – Nanotube conjugates // ACS Nano. 2010. Vol. 4. No. 7. Pp. 3993–4000.
https://doi.org/10.1021/nn100932t
92. *Zhan Y., Yu S., Amirfazli A. et al.* Recent advances in antibacterial superhydrophobic coatings // Advanced Engineering Materials. 2022. Vol. 24. No. 4. P. 2101053.
https://doi.org/10.1002/adem.202101053
93. *Ghilini F, Pissinis D.E., Minan A. et al.* How functionalized surfaces can inhibit bacterial adhesion and viability // ACS Biomaterials Science & Engineering. 2019. Vol. 5. No. 10. Pp. 4920–4936.
https://doi.org/10.1021/acsbiomaterials.9b00849
94. *Sun X., Zhang S., Li H., Bandara N.* Chapter 1 – Anti-adhesive coatings: A technique for prevention of bacterial surface fouling // Boddula R., Ahamed M.I., Asiri A.M. (ed.). Green Adhesives: Preparation, Properties and Applications. USA: Scrivener Publishing LLC. 2020. Pp. 1–23.
https://doi.org/10.1002/9781119655053.ch1
95. *Desrousseaux C., Sautou V., Descamps S., Traoré O.* Modification of the surfaces of medical devices to prevent microbial adhesion and biofilm formation // Journal of Hospital Infection. 2013. Vol. 85. No. 2. Pp. 87–93.
https://doi.org/10.1016/j.jhin.2013.06.015
96. *Hadjesfandiari N., Yu K., Mei Y., Kizhakkedathu J.N.* Polymer brush-based approaches for the development of infection-resistant surfaces // Journal of Materials

Chemistry B. 2014. Vol. 2. No. 31. Pp. 4968–4978. https://doi.org/10.1039/C4TB00550C

97. *Cloutier M., Mantovani D., Rosei F.* Antibacterial coatings: Challenges, perspectives, and opportunities // Trends in Biotechnology. 2015. Vol. 33. No. 11. Pp. 637–652. https://doi.org/10.1016/j.tibtech.2015.09.002

98. *Huang Z., Ghasemi H.* Hydrophilic polymer-based anti-biofouling coatings: Preparation, mechanism, and durability //Advances in Colloid and Interface Science. 2020 Vol. 284. P. 102264. https://doi.org/10.1016/j.cis.2020.102264

99. *Boinovich L.B., Kaminsky V.V., Domantovsky A.G. et al.* Bactericidal activity of superhydrophobic and superhydrophilic copper in bacterial dispersions // Langmuir. 2019. Vol. 35. No. 7. Pp. 2832–2841. https://doi.org/10.1021/acs.langmuir.8b03817

100. *Emelyanenko A.M., Kaminskii V.V., Pytskii I.S. et al.* Antibacterial properties of superhydrophilic textured copper in contact with bacterial suspensions // Bulletin of Experimental Biology and Medicine. 2020. Vol. 168. Pp. 488–491. https://doi.org/10.1007/s10517-020-04737-5

101. *Omran F.Sh., Kaminskiy V.V., Emelyanenko K.A. et al.* The effect of biological contamination of copper surfaces with extreme wetting on their antibacterial properties // Colloid Journal. 2023. Vol. 85. No. 5. Pp. 641–654. https://doi.org/10.31857/S0023291223600499

102. *Chen S., Li L., Zhao C., Zheng J.* Surface hydration: Principles and applications toward low-fouling / Nonfouling biomaterials // Polymer. 2010. Vol. 51. No. 23. Pp. 5283–5293. https://doi.org/10.1016/j.polymer.2010.08.022

103. *Schlenoff J.B.* Zwitteration: Coating surfaces with zwitterionic functionality to reduce nonspecific adsorption // Langmuir. 2014. Vol. 30. No. 32. Pp. 9625–9636. https://doi.org/10.1021/la500057j

104. *Estephan Z.G., Schlenoff P.S., Schlenoff J.B.* Zwitteration as an alternative to PEGylation // Langmuir. 2011. Vol. 27. No. 11. Pp. 6794–6800. https://doi.org/10.1021/la200227b

105. *Hooda A., Goyat M.S., Pandey J.K. et al.* A review on fundamentals, constraints and fabrication techniques of superhydrophobic coatings // Progress in Organic Coatings. 2020. Vol. 142. P. 105557. https://doi.org/10.1016/j.porgcoat.2020.105557

106. *Kang S.M., You I., Cho W.K. et al.* One-step modification of superhydrophobic surfaces by a mussel-inspired polymer coating // Angewandte Chemie International Edition. 2010. Vol. 49. No. 49. Pp. 9401–9404. https://doi.org/10.1002/anie.201004693

107. *Packham D.E.* Surface energy, surface topography and adhesion // International Journal of Adhesion and Adhesives. 2003. Vol. 23. No. 6. Pp. 437–448. https://doi.org/10.1016/S0143-7496(03)00068-X

108. *Xu L., Karunakaran R.G., Guo J., Yang S.* Transparent, superhydrophobic surfaces from one-step spin coating of hydrophobic nanoparticles // ACS Applied Materials & Interfaces. 2012. Vol. 4. No. 2. Pp. 1118–1125. https://doi.org/10.1021/am201750h

109. *Serles P., Nikumb S., Bordatchev E.* Superhydrophobic and superhydrophilic functionalized surfaces by picosecond laser texturing //Journal of Laser Applications. 2018. Vol. 30. No. 3. P. 032505. https://doi.org/10.2351/1.5040641

110. *Emelyanenko A.M., Shagieva F.M., Domantovsky A.G., Boinovich L.B.* Nanosecond laser micro-and nanotexturing for the design of a superhydrophobic coating robust against long-term contact with water, cavitation, and abrasion //Applied Surface Science. 2015. Vol. 332. Pp. 513–517. https://doi.org/10.1016/j.apsusc.2015.01.202

111. *Song B., Zhang E., Han X. et al.* Engineering and application perspectives on designing an antimicrobial surface // ACS Applied Materials & Interfaces. 2020. Vol. 12. No. 19. Pp. 21330–21341. https://doi.org/10.1021/acsami.9b19992

112. *Cheng G., Li G., Xue H. et al.* Zwitterionic carboxybetaine polymer surfaces and their resistance to long-term biofilm formation // Biomaterials. 2009. Vol. 30. No. 28. Pp. 5234–5240. https://doi.org/10.1016/j.biomaterials.2009.05.058

113. *Wang W., Lu Y., Zhu H., Cao Z.* Superdurable coating fabricated from a double-sided tape with long term “zero” bacterial adhesion // Advanced Materials. 2017. Vol. 29. No. 34. P. 1606506. https://doi.org/10.1002/adma.201606506

114. *Feng Y., Wang Q., He M. et al.* Antibiofouling zwitterionic gradational membranes with moisture retention capability and sustained antimicrobial property for chronic wound infection and skin regeneration // Biomacromolecules. – 2019. Vol. 20. No. 8. Pp. 3057–3069. https://doi.org/10.1021/acs.biomac.9b00629

115. *Liang X., Chen X., Zhu J. et al.* A simple method to prepare superhydrophobic and regenerable antibacterial films // Materials Research Express. 2020. Vol. 7. No. 5. P. 055307. https://doi.org 10.1088/2053-1591/ab903a

116. *Ma Y., Li J., Si Y. et al.* Rechargeable antibacterial N-halamine films with antifouling function for food packaging applications // ACS Applied Materials & Interfaces. Vol. 11. No. 19. Pp. 17814–17822. https://doi.org/10.1021/acsami.9b03464

117. *Del Olmo J.A., Pérez-Álvarez L., Martínez V.S. et al.* Multifunctional antibacterial chitosan-based hydrogel coatings on Ti6Al4V biomaterial for biomedical implant applications // International Journal of Biological Macromolecules. 2023. Vol. 231. P. 123328. https://doi.org/10.1016/j.ijbiomac.2023.123328.

118. *Chug M.K., Brisbois E.J.* Recent developments in multifunctional antimicrobial surfaces and

applications toward advanced nitric oxide-based biomaterials // ACS Materials Au. 2022. Vol. 2. No. 5. Pp. 525–551.
https://doi.org/10.1021/acsmaterialsau.2c00040

119. *Kaminskii V.V., Aleshkin A.V., Zul'karneev E.R. et al.* Development of a bacteriophage complex with superhydrophilic and superhydrophobic nanotextured surfaces of metals preventing healthcare-associated infections (HAI) // Bulletin of Experimental Biology and Medicine. 2019. Vol. 167. Pp. 500–503.
https://doi.org/10.1007/s10517-019-04559-0

120. *Yu Q., Wu Z., Chen H.* Dual-function antibacterial surfaces for biomedical applications // Acta Biomaterialia. 2015. Vol. 16. Pp. 1–13.
https://doi.org/10.1016/j.actbio.2015.01.018

121. *Hu X., Neoh K.G., Shi Z. et al.* An in vitro assessment of titanium functionalized with polysaccharides conjugated with vascular endothelial growth factor for enhanced osseointegration and inhibition of bacterial adhesion // Biomaterials. 2010. Vol. 31. No. 34. Pp. 8854–8863.
https://doi.org/10.1016/j.biomaterials.2010.08.006

122. *Zhao J., Song L., Shi Q. et al.* Antibacterial and hemocompatibility switchable polypropylene nonwoven fabric membrane surface // ACS Applied Materials & Interfaces. 2013. Vol. 5. No. 11. Pp. 5260–5268.
https://doi.org/10.1021/am401098u

123. *Yuan S.J., Pehkonen S.O., Ting Y.P. et al.* Antibacterial inorganic-organic hybrid coatings on stainless steel via consecutive surface-initiated atom transfer radical polymerization for biocorrosion prevention // Langmuir. 2010. Vol. 26. No. 9. Pp. 6728–6736.
https://doi.org/10.1021/la904083r

124. *Zou Y., Zhang Y., Yu Q., Chen H.* Dual-function antibacterial surfaces to resist and kill bacteria: Painting a picture with two brushes simultaneously // Journal of Materials Science & Technology. 2021. Vol. 70. Pp. 24–38.
https://doi.org/10.1016/j.jmst.2020.07.028

125. *Blum A.P., Kammeyer J.K., Rush A.M. et al.* Stimuli-responsive nanomaterials for biomedical applications // Journal of the American Chemical Society. 2015. Vol. 137. No. 6. Pp. 2140–2154.
https://doi.org/10.1021/ja510147n

126. *Zhang J., Liu L., Wang L. et al.* pH responsive zwitterionic-to-cationic transition for safe self-defensive antibacterial application // Journal of Materials Chemistry B. 2020. Vol. 8. No. 38. Pp. 8908–8913.
https://doi.org/10.1039/D0TB01717E

127. *Wei T., Yu Q., Chen H.* Responsive and synergistic antibacterial coatings: Fighting against bacteria in a smart and effective way // Advanced Healthcare Materials. 2019. Vol. 8. No. 3. P. 1801381.
https://doi.org/10.1002/adhm.201801381

128. *Cado G., Aslam R., Séon L. et al.* Self-defensive biomaterial coating against bacteria and yeasts: Polysaccharide multilayer film with embedded antimicrobial peptide // Advanced Functional Materials. 2013. Vol. 23. No. 38. Pp. 4801–4809.
https://doi.org/10.1002/adfm.201300416

129. *Ye J., Zhang X., Xie W. et al.* An enzyme-responsive prodrug with inflammation-triggered therapeutic drug release characteristics // Macromolecular Bioscience. 2020. Vol. 20. No. 9. P. 2000116.
https://doi.org/10.1002/mabi.202000116

130. *Fischer N.G., Chen X., Astleford-Hopper K. et al.* Antimicrobial and enzyme-responsive multi-peptide surfaces for bone-anchored devices // Materials Science and Engineering: C. 2021. Vol. 125. P. 112108.
https://doi.org/10.1016/j.msec.2021.112108

131. *Hizal F., Zhuk I., Sukhishvili S. et al.* Impact of 3D hierarchical nanostructures on the antibacterial efficacy of a bacteria-triggered self-defensive antibiotic coating // ACS Applied Materials & Interfaces. 2015. Vol. 7. No. 36. Pp. 20304–20313.
https://doi.org/10.1021/acsami.5b05947

132. *Sutrisno L., Wang S., Li M. et al.* Construction of three-dimensional net-like polyelectrolyte multilayered nanostructures onto titanium substrates for combined antibacterial and antioxidant applications // Journal of Materials Chemistry B. 2018. Vol. 6. No. 32. Pp. 5290–5302.
https://doi.org/10.1039/C8TB00192H

133. *Bu Y., Zhang L., Liu J. et al.* Synthesis and properties of hemostatic and bacteria-responsive in situ hydrogels for emergency treatment in critical situations // ACS Applied Materials & Interfaces. 2016. Vol. 8. No. 20. Pp. 12674–12683.
https://doi.org/10.1021/acsami.6b03235

134. *Hu Q., Du Y., Bai Y. et al.* Smart zwitterionic coatings with precise pH-responsive antibacterial functions for bone implants to combat bacterial infections // Biomaterials Science. 2024. Vol. 12. No. 17. Pp. 4471–4482.
https://doi.org/10.1039/D4BM00932K

135. *Wang T., Liu X., Zhu Y. et al.* Metal ion coordination polymer-capped pH-triggered drug release system on titania nanotubes for enhancing self-antibacterial capability of Ti implants // ACS Biomaterials Science & Engineering. 2017. Vol. 3. No. 5. Pp. 816–825.
https://doi.org/10.1021/acsbiomaterials.7b00103

136. *Liu T., Yan S., Zhou R. et al.* Self-adaptive antibacterial coating for universal polymeric substrates based on a micrometer-scale hierarchical polymer brush system // ACS Applied Materials & Interfaces. 2020. Vol. 12. No. 38. Pp. 42576–42585.
https://doi.org/10.1021/acsami.0c13413

137. *Zou Y., Lu K., Lin Y. et al.* Dual-functional surfaces based on an antifouling polymer and a natural antibiofilm molecule: Prevention of biofilm formation without using biocides // ACS Applied Materials & Interfaces. 2021. Vol. 13. No. 38. Pp. 45191–45200.
https://doi.org/10.1021/acsami.1c10747

138. *Wei H., Song X., Liu P. et al.* Antimicrobial coating strategy to prevent orthopaedic device-related infections: Recent advances and future perspectives // Biomaterials Advances. 2022. Vol. 135. P. 212739. https://doi.org/10.1016/j.bioadv.2022.212739

139. *Zhang L., Wang Y., Wang J. et al.* Photon-responsive antibacterial nanoplatform for synergistic photothermal-/pharmaco-therapy of skin infection // ACS Applied Materials & Interfaces. 2018. Vol. 11. No. 1. Pp. 300–310. https://doi.org/10.1021/acsami.8b18146

140. *Wu Q., Wei G., Xu Z. et al.* Mechanistic insight into the light-irradiated carbon capsules as an antibacterial agent // ACS Applied Materials & Interfaces. 2018. Vol. 10. No. 30. Pp. 25026–25036. https://doi.org/10.1021/acsami.8b04932

141. *Chen X., Zhou J., Qian Y., Zhao L.* Antibacterial coatings on orthopedic implants // Materials Today Bio. 2023. Vol. 19. P. 100586. https://doi.org/10.1016/j.mtbio.2023.100586

142. *Wei T., Qu Y., Zou Y. et al.* Exploration of smart antibacterial coatings for practical applications // Current Opinion in Chemical Engineering. 2021. Vol. 34. P. 100727. https://doi.org/10.1016/j.coche.2021.100727

COLLOID JOURNAL, 2025, Vol. 87, No. 1, pp. 69–78

KINETICS OF INTERACTION OF Co–Cu MELTS WITH GRAPHITE AND MICROSTRUCTURE OF FORMING METAL-CARBON COMPOSITIONS

© 2025 O. A. Chikova[a, *], I. G. Shirinkina[b], V. S. Tsepelev[a],
N. I. Sinitsin[a], and V. V. Vyukhin[a]

[a]*Ural Federal University named after the first President of Russia B.N. Yeltsin,*
Ekaterinburg, Russia

[b]*Mikheev Institute of Metal Physics, Ural Branch of the RAS,*
Ekaterinburg, Russia

**e-mail: O.A.Chikova@urfu.ru*

Received May 30, 2024
Revised August 12, 2024
Accepted August 13, 2024

Abstract. The time dependences of the contact angle and the wetted surface spot diameter were measured during the interaction of Co–Cu melts with copper contents of 20, 40 and 60 at. % with graphite at temperatures of 1390, 1440, 1490, 1540 and 1590°C. Wetting of graphite by Co–Cu melts does not occur under these conditions: the final contact angle for Co80Cu20 is 95°, Co60Cu40 is 110°, Co40Cu60 is 100°. The final value of the diameter of the wetted surface spot increases somewhat. Metallographic analysis of the microstructure of Co–Cu–C composite materials obtained by contact alloying of Co–Cu melts with carbon showed the dependence of the morphology of the structural components and the phase composition of the samples on the copper content. Composite materials (Co–27%C–10%Cu) + (Co–32%C–62%Cu) + C and (Co–19%C–15%Cu) + (Co–25%C–72%Cu) + C, obtained by the interaction of Co–Cu melts with a copper content of 20, 40 at. % with graphite, have a macro-homogeneous structure.

Keywords: *Co–Cu melt, graphite, contact alloying, metal-carbon materials Co–Cu–C, microstructure*

DOI: 10.31857/S00232912250108e8

INTRODUCTION

The study of the kinetics of interaction of Co–Cu melts with graphite and microstructure of crystallized samples of Co–Cu–C composite materials is relevant both from the fundamental point of view and from the point of view of practical application. The peculiarity of the phase diagram of the Cu–Co system is the presence of a metastable mixing zone: under sufficiently deep supercooling, the Co–Cu melt splits into two liquids: cobalt-rich and copper-rich [1]. Phase separation occurs due to simultaneous nucleation, coalescence and diffusion [2] and determines the crystallization conditions of Cu–Co alloys [3–7]. The microstructure of crystallized Co–Cu samples contains spherulites of one phase embedded in the matrix of another; spherulites in alloys containing more than ~60 at. % Cu solidify from the Co-based melt, and in alloys containing less than~ 40 at. % Cu – from the Cu-based melt [8]. The microstructure of crystallized samples is determined by the morphology, segregation pattern and size distribution of Co-rich droplets, with droplet migration controlled by the Marangoni force and Stokes force [9–10]. The presence of carbon in the melt, as suggested by the authors, can change the crystallization conditions and lead to the formation of a specific microstructure of crystallized Co–Cu–C samples. The technology of contact alloying of melts Co–Cu with carbon allows to obtain bulk samples of metal-carbon materials Co–Cu–C and is simple enough in technical realization [11] . Earlier the method of contact alloying of Fe–Cu melt with carbon allowed to obtain a unique composite material Fe–60%Cu–C, where iron-based phase is stratified into alloys of pre-eutectic and eutectic compositions (gray and white cast iron) [12–13].

Metal-carbon Co–Cu–C compositions are primarily of interest as materials that absorb microwave radiation [14–15]. A thin film catalyst made of Co–Cu bimetallic alloy has also been developed, which allows the growth of single layer high quality graphene (SLG) [16]. Cobalt electrodes coated with SLG exhibit high magnetic anisotropy [17], remain resistant to oxidation in air and are promising as spin filtration electrodes [18]. Known methods of obtaining metal-carbon Co–Cu–C compositions: the electrodeposition method [19]; methods when carbide-forming metals are removed from metal carbides by acid etching [20] or chlorination [21], the method of thermal decomposition of the Co–Cu double salicylate complex in argon atmosphere [22], do not allow obtaining bulk samples. In this work another method of obtaining metal-carbon Co–Cu–C compositions – contact carbon doping of Co–Cu melts with copper content of 20, 40 and 60 at. % was used. For the first time temperature and time dependences of the contact angle, diameter of the wetted surface spot were measured, metallographic analysis of the obtained Co–Cu–C samples was carried out. In the future, the results of the study are useful for working out the technology of obtaining granulated Co–Cu–C compositions. Granulated Co–Cu alloys have been intensively investigated since the discovery of the effect of giant magnetoresistance in these materials [23], which determines the ability of Co–Cu–C compositions to absorb microwave radiation [14]. Co–Cu alloys are known to be paramagnetic at Co concentrations less than 25 at. % [24]. Therefore, the interaction of Co–Cu melts with Co content of 20, 40 and 60 at. % with graphite was studied in this work. Obtaining metal-carbon Co–Cu–C compositions by contact alloying is associated with a number of difficulties, since the copper-rich phase is displaced to the surface during separation [25] and prevents the melt from wetting the graphite substrate. Copper in solid and liquid states is in equilibrium with graphite [26]. Liquid copper does not wet carbon substrates [27–30], and graphite is impregnated with copper melts at high temperatures (>1200°C) and high overpressure (10–100 MPa) [31]. A slight decrease in overpressure can be achieved by alloying copper melts with surface-active elements (Ti, Mn, Cr, W, Nb, Mo, Co in the amount of 1–2 wt%) [31–33]. Co interacts eutectically with carbon $L \leftrightarrow (\sigma\text{-Co}) + (C)$ at 1319°C and 11.9 at. % C [26, 34]. Although cobalt melt wets graphite – contact angle decreases from 82 to 35° when heated from 1425 to 1495°C, Co–2.7%C melt at 1495°C does not wet the graphite surface – contact angle 130°, Cu–5%Co melt also does not wet graphite at 1300°C – contact angle 138° [28]. Measurements of the contact angle at interaction of Co–Cu melts with copper content of 20, 40 and 60 at. % with graphite have not been carried out before.

This paper presents relevant data on the kinetics of the interaction of Co–Cu melts with graphite and a description of the microstructure of crystallized samples of Co–Cu–C composites.

1. KINETICS OF INTERACTION OF Co–Cu GRAPHYTIC ARMOSTS WITH GRAPHITE

Determination of graphite wetting angles with Co–Cu melts was carried out according to the standard lying drop technique under conditions of joint heating of the sample and substrate. Samples for the experiment were preliminary alloyed from pure components in a closed muffle resistance furnace at 1530°C for 60 min. The starting materials were metals of high purity: copper grade B-3 (99.98%) and cobalt grade K1Au (99.35%). The mass of the sample was 4 g. As substrates we used polycrystalline graphite of spectral purity. The porosity of graphite (13.5%) was determined by the technique of measuring the volume of open pores [35]. Substrates from such graphite were carefully polished and ground, then calcined in vacuum (at a pressure below 1 Pa) at 1500°C for 1 h. The surface roughness of the substrate was of the order of 10 μm. Fusion of initial samples and measurement of edge angles were carried out in an atmosphere of high-purity helium. The working chamber was pre-vacuumed to 0.001 Pa. Helium was then run to a pressure of $\sim 10^5$ Pa. Wetting angles were measured in the mode of successive step heating from 1420 to 1620°C with holding at each temperature for 20 min. The sufficiency of such holding time is confirmed both by earlier studies [28, 36] and by our studies of the flow velocity of Fe–Cu melts on the graphite surface [13]. The profile of the investigated drop was recorded every minute using a digital camera. The images were recorded in computer memory and analyzed using SIAMS700 software. The wetting angle was determined with an accuracy of 0.3–0.6°. Signs of melt evaporation, drop volume reduction were not observed. The random error in determining the edge angle did not exceed 3% at a confidence level of 0.95. The method of measuring the angle of wetting of the graphite surface by metal melt (sitting drop method) and the setup for its realization have been previously described in [13, 28, 36–37].

The results of measuring the wetting angles θ of graphite with Co–Cu melts are presented in Fig. 1. Upon heating from 1390 to 1590°C, the final contact angle decreases from 125 to 95° (by 24%) in the experiment with Co80–Cu20 melt; from 138 to 110° (by 20%) in the experiment with Co60–Cu40 melt and from 110 to 100° (by 9%) in the experiment with Co40–Cu60 melt. Thus, the more Cu in the melt, the worse it wets the graphite surface. Note that the value of the contact angle depends little on time and decreases weakly with temperature: in the experiments with the Co80–Cu20 and Co40–Cu60 melts from about 110 to 100°, in the experiment with the Co60–Cu40 melt – from about 130 to 110°.

The results of measuring the diameter d of the spot diameter of the graphite surface wetted with Co–Cu melts are presented in Fig. 2. The spot diameter of the graphite surface wetted by Co–Cu melts significantly increases at the beginning of the interaction at 1390°C, and in the experiments with Co80–Cu20 (by 2%) and Co60–Cu40 (by 7%) melts – during the first 5 minutes, in the experiment with Co40–Cu60 melt (by 3%) during 15 minutes (Fig. 2). The spreading rate of Co–Cu melts at higher temperatures is weakly time dependent and does not significantly increase with temperature. The final value of the spot diameter of the graphite surface

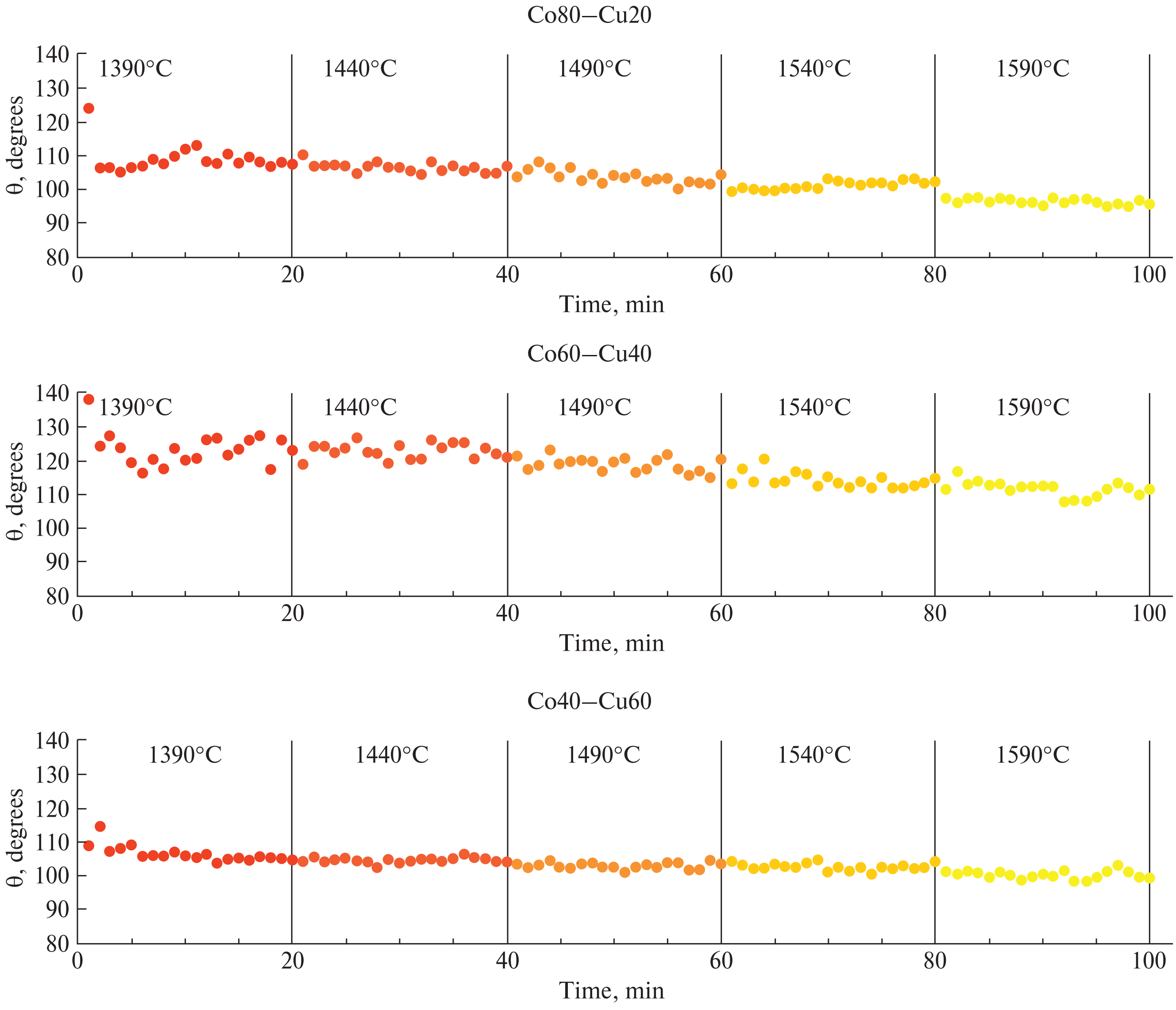

Fig. 1. Time dependences of graphite wetting angles θ with Co–Cu melts with Cu content of 20, 40 and 60 at. % at 1390, 1440, 1490, 1540 and 1590°C. The method of measuring θ is shown in Fig. 2a.

wetted by Co–Cu melts when heated from 1390 to 1590°C increases from 10.4 to 12.0 mm (by 15%) in the Co80–Cu20 melt experiment; from 11.2 to 12.4 mm (by 11%) in the Co60–Cu40 melt experiment from 11.8 to 12.4 mm (by 5%) in the Co40–Cu60 melt experiment (Fig. 2). Thus, the more copper in the melt, the worse it sinks on the graphite surface.

The results of measuring the height *h* of Co–Cu melt droplet with Cu content of 20, 40 and 60 at. % above the graphite surface are presented in Fig. 3. The change of height *h* of Co–Cu melt drop above the graphite surface reflects the change of its geometrical dimensions, including due to the formation of a depression on the graphite surface as a result of its interaction with the melt. The height of Co–Cu melt drop above the graphite surface significantly decreases at the beginning of interaction at 1390°C in the experiments with Co80–Cu20 (by 6%) and Co60–Cu40 melt (by 16%), in the experiment with Co40–Cu60 melt (by 6%) within 15 minutes (Fig. 3). The height *h* of the Co–Cu melt droplet above the graphite surface at higher temperatures is weakly time dependent and does not significantly decrease with temperature. The final value of the height *h* of the Co–Cu melt droplet above the graphite surface when heated from 1390 to 1590°C increases from 4.8 to 4.5 mm (by 7%) in the Co80–Cu20 melt experiment; from 5.9 to 5.7 mm (by 4%) in the Co60–Cu40 melt experiment and from 5.1 to 4.9 mm (by 4%) in the Co40–Cu60 melt experiment (Fig. 3). Thus, the more cobalt in the melt, the better it dissolves the graphite surface.

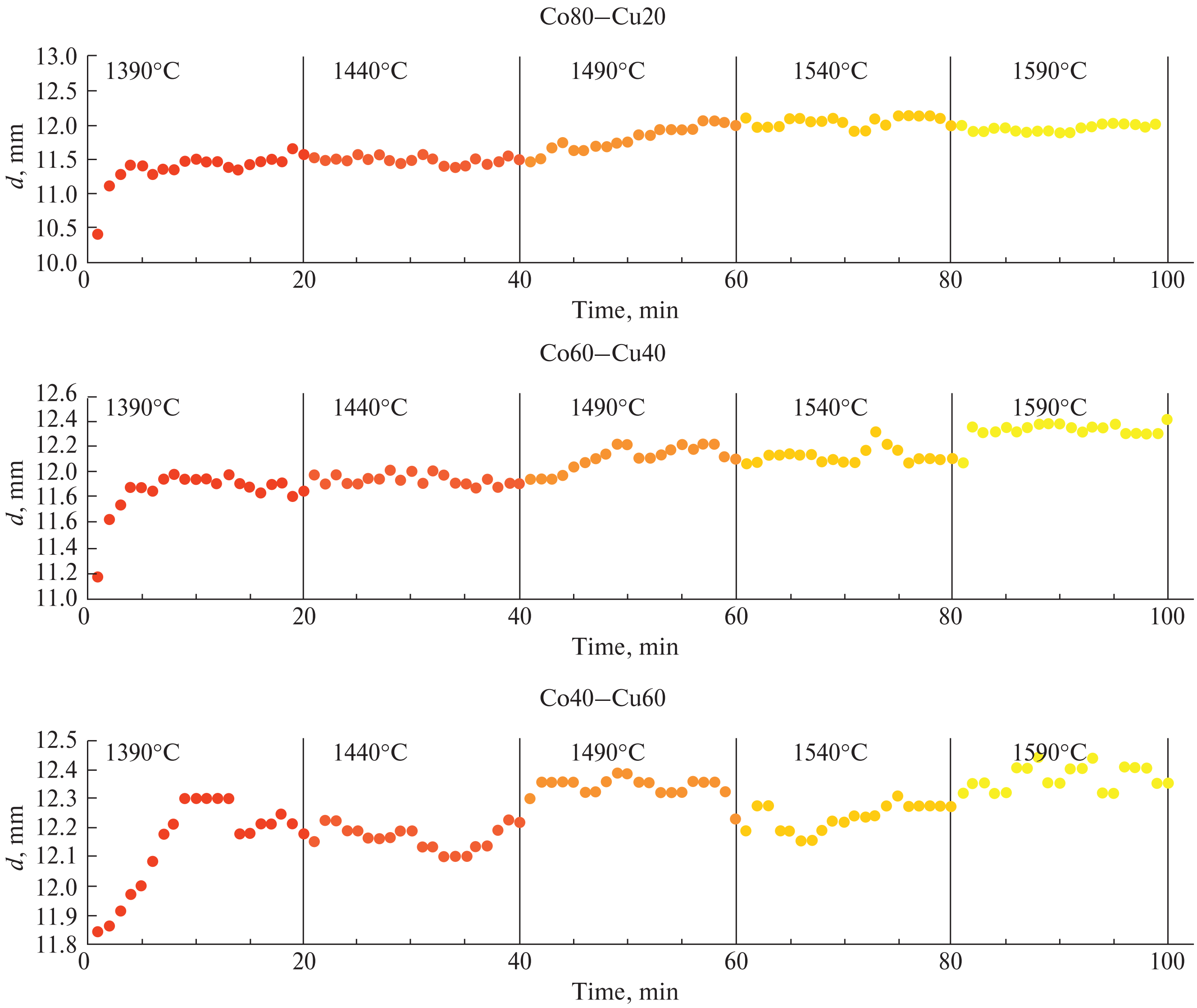

Fig. 2. Time dependences of spot diameter of the graphite surface wetted with Co–Cu melts with 20, 40 and 60 at. % Cu content at 1390, 1440, 1490, 1540 and 1590°C.

Thus, it was possible to continue studies of the kinetics of interaction of Fe–Cu melts delaminating in the liquid state with graphite [13] for the system Co–Cu with a similar type of phase diagram, the peculiarity of which is the presence of a metastable mixing zone; under sufficiently deep supercooling, the Co–Cu melt splits into two liquids: cobalt-rich and copper-rich [1]. It was found that, as for Fe–Cu [13], so for Co–Cu the contact angle and diameter of the wetted surface spot depend weakly on temperature, but there is a significant difference – wetting of graphite by Co–Cu melts with copper content of 20, 40 and 60 at. % at temperatures of 1390, 1440, 1490, 1540 and 1590°C does not occur. Earlier it was noted that pre carburized cobalt Co–2.7%C melt does not wet graphite at 1495°C, contact angle 130° in contrast to Fe–C melts [28].

2. MICROSTRUCTURES OF Co–Cu–C SAMPLES OBTAINED BY CONTACT LAGGING OF Co–Cu ALLOYS WITH HYDROCARBON

Metallographic study of macro and microstructures of Co–Cu–C samples obtained after wetting experiments at cooling rates of 1–10°C/s was performed using a Neophot-32 light microscope. Fine structure studies and local microanalysis were performed on a Tescan MIRA scanning electron microscope with an energy dispersive analysis (EDS) attachment. The samples cut out of the alloy in longitudinal section were ground on grinding paper with different grits, from P80 to P2500. Then polishing was carried out on aqueous chromium oxide solution and colloidal silicon suspension.

The general view of the samples is shown in Fig. 4. By appearance they can be divided into two groups:

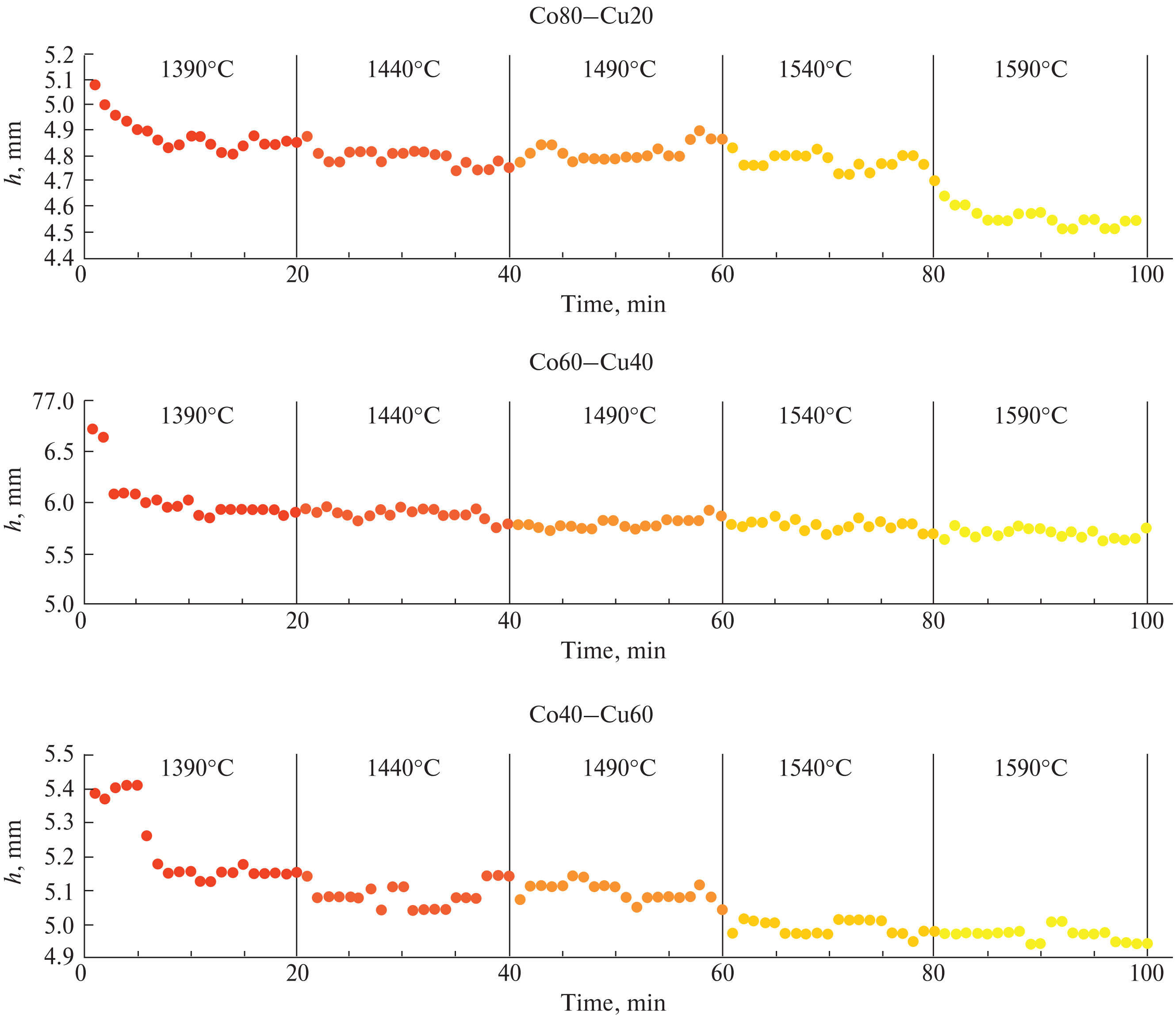

Fig. 3. Time dependences of the drop height *h* of Co–Cu melt with Cu content of 20, 40 and 60 at. % at 1390, 1440, 1490, 1490, 1540 and 1590°C relative to the graphite surface.

rich in cobalt (Co–20 at. % Cu–C and Co–40 at. % Cu–C) and copper (Co–60 at. % Cu–C). Both groups are characterized by melt stratification with displacement of the copper phase to the periphery of the sample. For samples of the first group there is isolation of the copper phase, and for samples of the second group – the phase rich in cobalt. Previously, phase reversal at the transition through equiatomic composition has been reported for Fe–Cu melts during graphite wetting [12–13]. The stratification of Co–60 at. % Cu–C sample occurs in the whole volume (Fig. 4c). The alloys Co–20 at. % Cu–C and Co–40 at. % Cu–C are characterized by a rather homogeneous structure. Earlier by the method of contact alloying of Fe–Cu melt with carbon a similar result was obtained: delamination of Fe–60%Cu–C sample occurred in the whole volume [12–13]. Consequently, obtaining bulk macro homogeneous samples of metal-carbon materials Co–Cu–C by the technology of contact alloying of Co–Cu melts with carbon at low cooling rates (1–10°C/s) is possible with excess of cobalt in the melt.

As follows from the structural analysis, the increase of copper content from 20 to 60% leads to significant changes in the morphology of structural components and phase composition of samples after wetting experiments. The interaction of carbon with cobalt and cobalt with copper according to the state diagrams, Co–C and Co–Cu [1, 26, 34], causes the formation of complex multiphase structures.

The main structural component in the metal-carbon material Co–20%Cu–C is Co–C eutectic and primary carbon crystals, i.e. in the process of carbon diffusion from the substrate into the Co phase, its concentration becomes higher than the eutectic one, and the alloy solidifies according to the hypereutectic type. Co–C eutectic structure belongs to the category of disordered eutectics of plate-needle morphology. Primary carbon crystals have the form of thin plates, the length of which reaches 100–300 μm (Fig. 5a). Rounded copper zones of rounded shape and ~10–50 μm in size are formed throughout the sample volume (to a greater extent along the periphery). Most often they are located near the carbon plates (Fig. 5a, b).

The formation of Cu phase occurs by peritectic reaction from Co-based solid solution and Cu-enriched melt. The presence of Co–C eutectic leads to the fact that the nucleation of copper phase is heterogeneous on the interfacial surface of particles of carbon and Co solid solution, which creates the effect of two-phase composite particles C/Cu. The structure of the Co–40%Cu–C metal-carbon sample, in contrast to the Co–20%Cu sample, is very heterogeneous (Fig. 6b). A ~300–350 μm thick copper layer is located near the substrate. Further up to the middle of the sample and above extends an extensive zone enriched with cobalt, within which a copper-based phase is located in the form of irregularly shaped zones (grains). Within this phase are cobalt crystals of dendritic morphology. Fig. 6a shows the boundary of Co and Cu zones and Co dendrites in the Cu zone.

The copper layer located near the substrate is also biphasic, the Co alloy dendrites in it grow perpendicular to the graphite substrate (Fig. 6b). Carbon in the form of thin needle-shaped crystals is present throughout the sample volume, however, its amount in the cobalt-based zone is much less than in the copper zone (Fig. 6a).

In the Co–60%Cu–C sample, an opposite set of structures is observed, in which the volume ratio of cobalt and copper zones changes in favor of the latter (Fig. 4c). Most of the sample has a eutectoid-type structure consisting of a copper base and cobalt dendrites (Fig. 7a).

At the substrate (Fig. 7a) and along the periphery of the sample, isolated zones of Co–C eutectic with inclusions of copper phase are formed (Fig. 7b). In these zones, the tendency of joint nucleation and growth of Cu and C phases is clearly manifested.

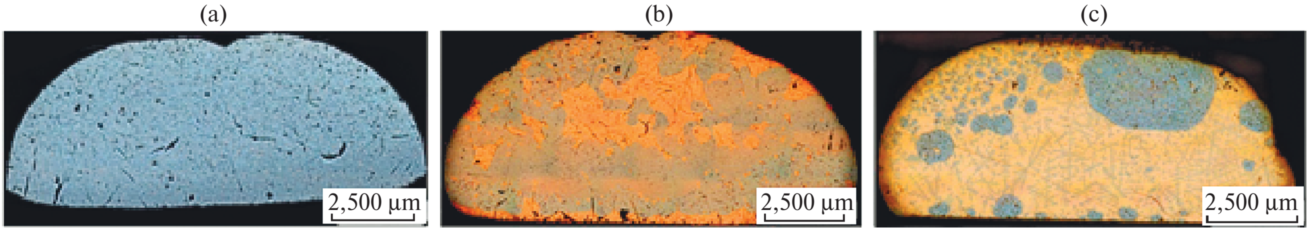

Fig. 4 General view of Co–Cu–C samples: a) Co–20%Cu–C; b) Co–40%Cu–C; c) Co–60%Cu–C.

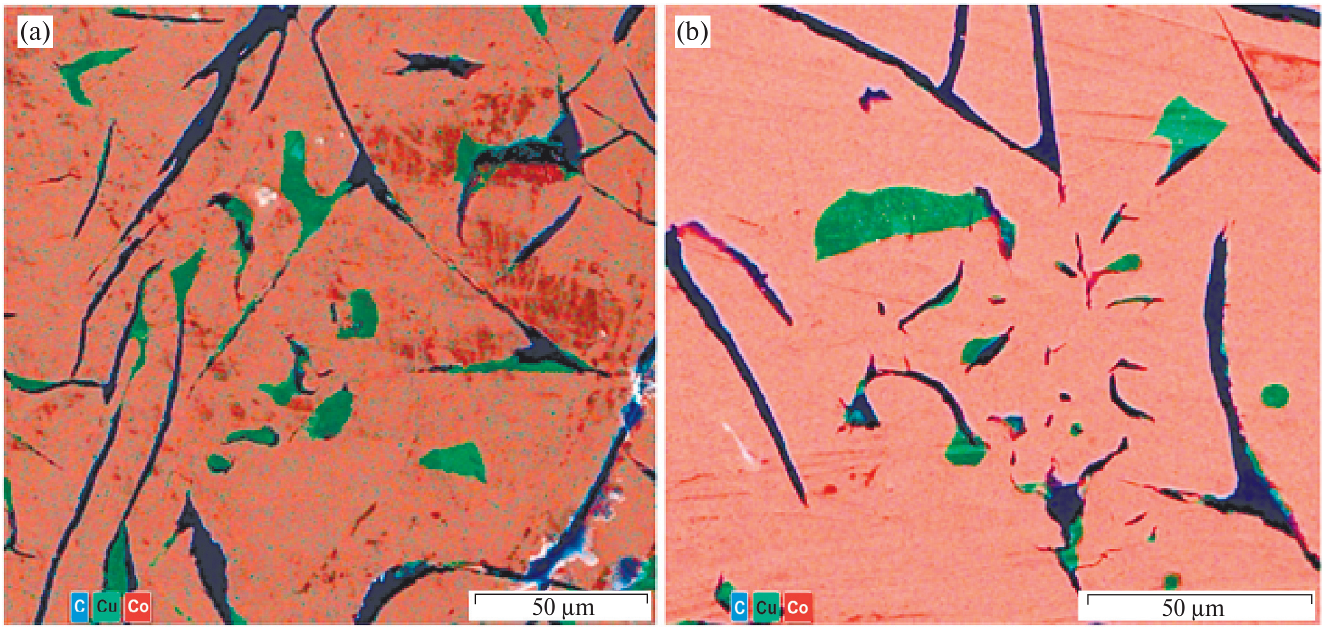

Fig. 5. Structure of Co–20%Cu–C metal-carbon material: a) Co–C eutectic; b) copper zones in Co–C eutectic and EDS map of element distribution (SEM).

Thus, on the basis of the conducted studies it is shown that at the transition through the equiatomic composition there is a change in the composition and volume fraction of isolated zones. In the samples of metal-carbon material Co–20%Cu–C and Co–40%Cu–C the isolated zones are enriched with copper, and in the sample of metal-carbon material Co–60%Cu–C – with cobalt. Previously, a similar phase reversal at the transition through the equiatomic composition was found for melts of the Fe–Cu system [12–13].

The kinetics of diffusion dissolution of carbon depends on the composition of the initial alloy. From the data [28] it is known that carbon does not diffuse through the copper phase, so in experiments on wetting the graphite substrate Co–Cu melts, its dissolution is carried out in the phase rich in cobalt. It is found

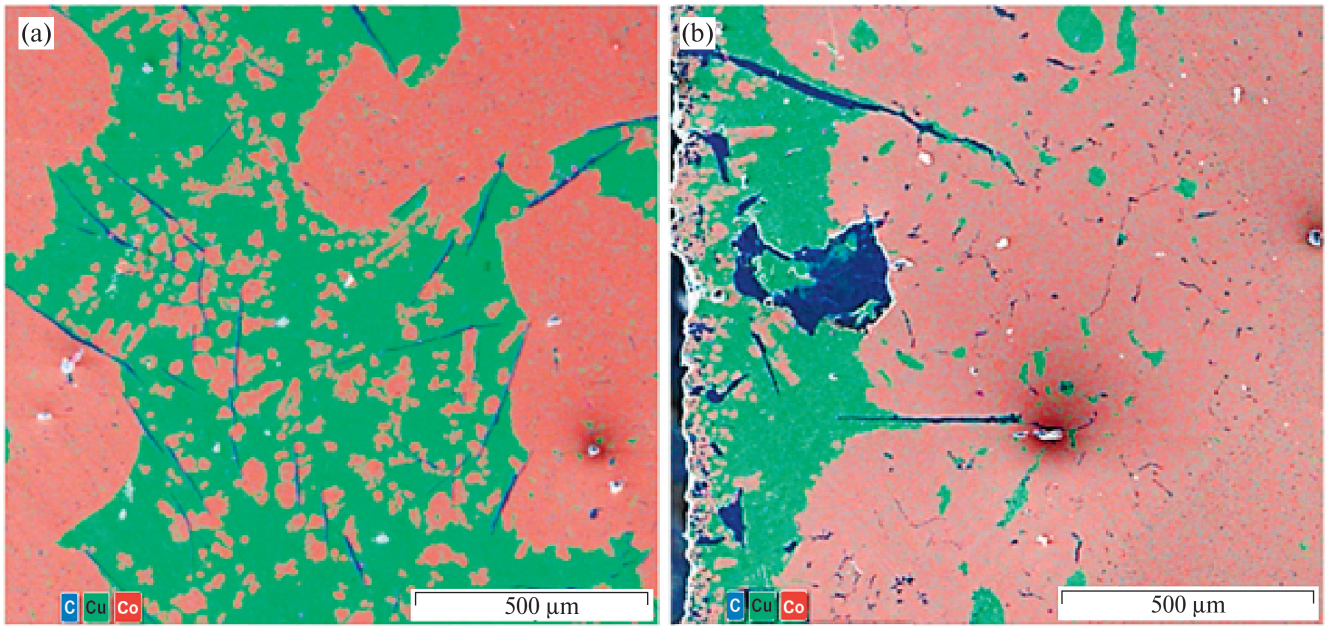

Fig. 6. Structure of metal-carbon Co–40%Cu–C material: a) boundary of Co and Cu zones and Co dendrites in Cu zone; b) area at the contact point of the sample with graphite substrate; EDS maps of element distribution (SEM).

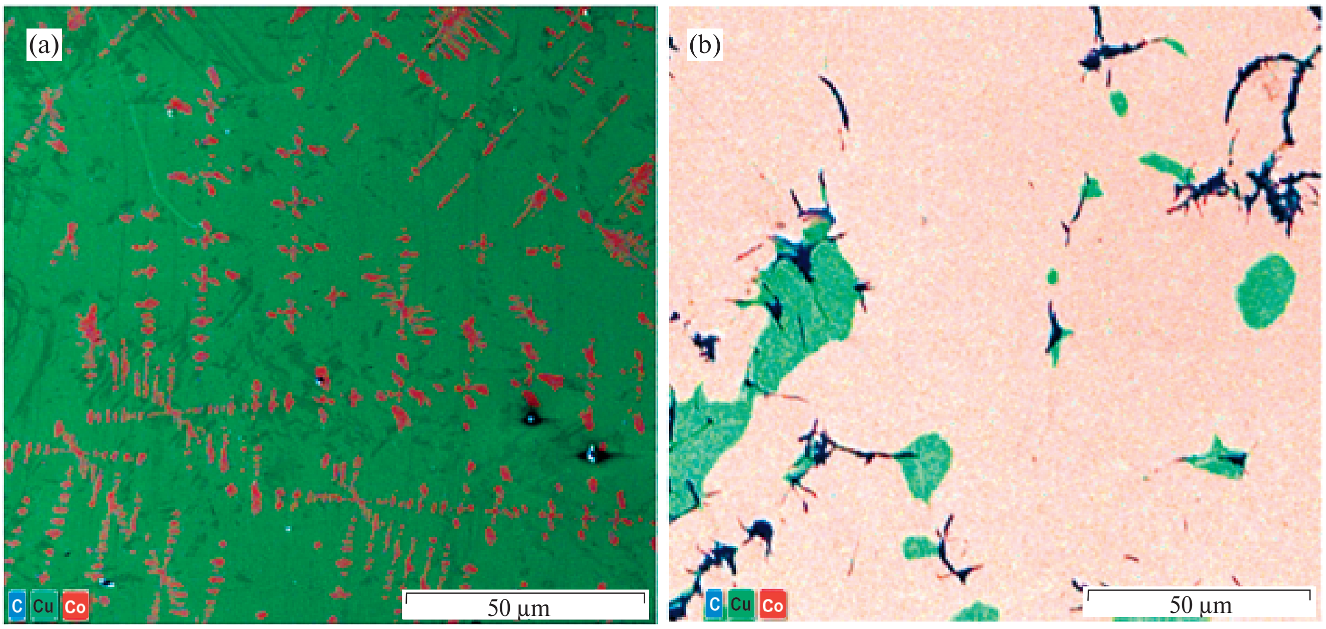

Fig. 7. Structure of Co–20%Cu–C metal-carbon material: a) Cu zone with Co dendrites; b) isolated Co–C eutectic zones with copper phase inclusions, EDS maps of element distribution (SEM).

how the carbon content of metal-carbon Co–Cu–C materials varies with the cobalt content of the initial alloy. According to EDS-analysis data, contact alloying of Co–20%Cu melts with carbon resulted in the composite material (Co–27%C–10%Cu) + + (Co–32%C–62%Cu) + C (Fig. 5a), Co–40%Cu – – (Co–19%C–15%Cu) + (Co–25%C–72%Cu) + C melt (Fig. 6a), Co–60%Cu – (Co–20%C–15%Cu) + + (Co–23%C–74%Cu) + C melt (Fig.7a).

Despite the above-mentioned differences in the structure formation of metal-carbon Co–Cu–C materials with different copper content, it is possible to note the features common to all compositions. In particular, it is a change in the geometry of the contact zone of the substrate with the melt, which is manifested in the destruction of the graphite substrate. Changes in the geometry of the contact zone of solid and liquid metal – crater formation and dispersion of graphite were found. Crater formation is a sign of intensive dissolution of carbon in the melt. Graphite dispersion accompanies the process of phase infiltration of the melt through the pores. The destruction of the graphite substrate is most pronounced for the samples rich in cobalt: Co–20%Cu–C and Co–40%Cu–C (Fig. 6b), which agrees with the data of measuring the height h of the Co–Cu melt drop with copper content of 20, 40 and 60 at. % above the graphite surface (Fig. 3). The final value of h height at heating from 1390 to 1590°C increases by 7% in the Co80–Cu20 melt experiment; by 4% in the Co60–Cu40 melt experiment and by 4% in the Co40–Cu60 melt experiment (Fig. 2). Thus, the more cobalt in the melt, the better it dissolves the graphite surface.

Thus, by methods of light optics, scanning electron microscopy and local X-ray spectral analysis the following regularities of structure formation of metal-carbon Co–Cu–C compositions obtained as a result of wetting graphite with Co–Cu melts have been established: (1) increase of copper content from 20 to 60 at. % leads to changes in morphology of structural components and phase composition of samples; (2) at transition through equiatomic composition the ratio of volume fraction of phases changes, i.e. in Co–20%Cu–C and Co–40%Cu–C samples the copper phase is isolated, and in Co–60%Cu–C sample – the cobalt-based phase; (3) due to intensive dissolution of carbon in cobalt, the cobalt-rich phase has the structure of Co–C eutectic; (4) interaction of cobalt and copper leads to the formation of a mixture of two solid solutions of eutectoid type, taking into account the weak mutual solubility of the components, it can be considered that the eutectoid consists of pure Cu and pure Co; (5) as a result of interaction of graphite substrate with Co–Cu melts, its destruction is observed.

CONCLUSION

Studies of kinetics of interaction of Co–Cu melts with copper content of 20, 40 and 60 at. % with graphite were carried out by measuring time dependences of contact angle and diameter of the wetted surface spot at temperatures of 1390, 1440, 1490, 1540 and 1590°C. Wetting of graphite by Co–Cu melts does not occur under these conditions: the final contact angle for Co80–Cu20 is 95°, Co60–Cu40 – 110°, Co40–Cu60 – 100°. The spot diameter of the wetted surface increases significantly only at the beginning of the interaction within 5–10 min. The final value of the spot diameter of the wetted surface increases for Co80–Cu20 by 15%, Co60–Cu40 by 11%, and Co40–Cu60 5% when heated from 1390 to 1590°C.

Metallographic analysis of the microstructure of Co–Cu–C composite materials obtained by contact alloying of Co–Cu melts with carbon showed the dependence of the morphology of structural components and phase composition of samples on the copper content; macrohomogeneous samples were obtained with excess of cobalt melt; as a result of interaction of graphite substrate with Co–Cu melts, its destruction is observed.

FUNDING

The study of wetting of graphite by Co–Cu melts was carried out at the Research Center for Physics of Metallic Liquids of the Institute of New Materials and Technologies of UFU within the framework of state work No. FEUZ-2023-0015.

The structure studies were carried out at the Institute of Physics and Mathematics of the Ural Branch of the Russian Academy of Sciences within the framework of the state assignment of the Ministry of Science and Technology of the Russian Federation (theme “Structure”, No. 122021000033-2). Electron-microscopic studies were carried out at the Test Center for Nanotechnologies and Advanced Materials of the IMP of the Ural Branch of the Russian Academy of Sciences.

ETHICS DECLARATION

There are no human or animal studies in this paper.

CONFLICT OF INTERESTS

The authors of this paper declare that they have no conflict of interests.

REFERENCES

1. *Nishizawa T., Ishida K.* The Co–Cu (Cobalt–Copper) system // Bull. Alloy phase diagr. 1984.Vol. 5. Pp. 161–165. https://doi.org/10.1007/BF02868953
2. *Guo F., Lu T., Qin J., Zheng H., Tian X.* Abnormal resistivity behavior of Cu–Ni and Cu–Co alloys in undercooled liquid state // Phys. B. 2012. Vol. 407. Pp. 4108–4113. https://doi.org/10.1016/j.physb.2012.06.024

3. *Yamauchi I., Ueno N., Shimaoka M., Ohnaka I.* Undercooling in Co–Cu alloys and its effect on solidification structure // J. Mater. Sci. 1998. Vol. 33. Pp. 371–378. https://doi.org/10.1023/A:1004319829612
4. *Robinson M.B., Li D., Rathz T.J., Williams G.* Undercooling, liquid separation and solidification of Cu–Co alloys // J. Mater. Sci. 1999. Vol. 34. Pp. 3747–3753. https://doi.org/10.1023/A:1004688313591
5. *Lu X.Y., Cao C.D., Kolbe M., Wei B., Herlach D.M.* Microstructure analysis of Co–Cu alloys undercooled prior to solidification // Mater. Sci. Eng. A. 2004. Vol. 375–377. Pp. 1101–1104. https://doi.org/10.1016/j.msea.2003.10.106
6. *Yang W., Chen S.H., Yu H., Li S., Liu F., Yang G.C.* Effects of liquid separation on the microstructure formation and hardness behavior of undercooled Cu–Co alloy // Appl. Phys. A. 2012. Vol. 109. Pp. 665–671. https://doi.org/10.1007/s00339-012-7090-4
7. *Munitz A., Venkert A., Landau P., Kaufman M.J., Abbaschian R.* Microstructure and phase selection in supercooled copper materials showing metastable liquid miscibility gap // J. Mater. Sci. 2012. Vol. 47. Pp. 7955–7970. https://doi.org/10.1007/s10853-012-6354-x
8. *Munitz A., Abbaschian R.* Microstructure of Cu–Co alloys solidified at various supercoolings // Metall Mater Trans A. 1996. Vol. 27. Pp. 4049–4059. https://doi.org/10.1007/BF02595654
9. *Zhao D., Gao J.* Liquid phase separation in undercooled Cu–Co alloys under the influence of static magnetic fields // Philosophical Transactions A. 2019. Vol. 377. P. 20180207. https://doi.org/10.1098/rsta.2018.0207
10. *Zhao D., Liu R., Wu D., Bo L., Wang L.* Liquid–liquid phase separation and solidification behavior of Al–Bi–Sb immiscible alloys // Results in Physics. 2017. Vol. 7. Pp. 3216–3221. https://doi.org/10.1016/j.rinp.2017.08.056
11. *Avraamov Yu.S., Koshkin V.I., Petrishchev I.M., Shlyapin A.D.* Production of alloys based on immiscible component systems by contact alloying // Mashinostr. inzhen. obrazov. 2007. No. 4. Pp. 21–30.
12. *Brodova I.G., Chikova O.A., Vityunin M.A., Yablonskikh T.I., Shirinkina I.G., Astaf'ev V.V.* The structure of Fe–Cu–C alloys obtained by contact alloying // Fiz. met. metalloved. 2009. Vol. 108. No. 6. Pp. 626–632.
13. *Chikova O.A., Vityunin M.A., Chentsov V.P., Sakun G.V.* Separation of Fe–Cu melts during graphite wetting // Colloid Journal. 2010. Vol. 72. No. 2. Pp. 251–257.
14. *Song Z., Liu X., Sun X. et al.* Alginate-templated synthesis of CoFe/carbon fiber composite and the effect of hierarchically porous structure on electromagnetic wave absorption performance // Carbon. 2019. Vol. 151. P. 36. https://doi.org/10.1016/j.carbon.2019.05.025
15. *Sugime H., D'Arsiè L., Esconjauregui S. et al.* Low temperature growth of fully covered single-layer graphene using CoCu catalyst // Nanoscale. 2017. V. 9. No. 38. Pp. 14467–14475. https://doi.org/10.1039/C7NR02553J
16. *Fan X., Mashimo T., Huang X. et al.* Magnetic properties of Co-Cu metastable solid solution alloys // Phys. Rev. B. 2004. Vol. 69. P. 094432. https://doi.org/10.1103/PhysRevB.69.094432
17. *Weatherup R.S., D'Arsié L., Cabrero-Vilatela A. et al.* Long-term passivation of strongly interacting metals with single-layer graphene // J. Am.Chem. Soc. 2015 Vol. 137. No. 45. Pp. 14358–14366. https://doi.org/10.1021/jacs.5b08729
18. *Karpan V.M., Khomyakov P.A., Starikov G. et al.* Theoretical prediction of perfect spin filtering at interfaces between close-packed surfaces of Ni or Co and graphite or graphene // Phys. Rev. B: Condens. Matter. 2008. Vol. 78. P. 195419. https://doi.org/10.1103/PhysRevB.78.195419
19. *Wan Y., Xiao J., Li Ch. et al.* Microwave absorption properties of FeCo-coated carbon fibers with varying morphologies // J. Magn.Magn. Mater. 2016. Vol. 399. Pp. 252–259. https://doi.org/10.1016/j.jmmm.2015.10.006
20. *Kyutt R.N., Danishevskiy A.M., Smorgonskaya E.A. et al.* X-ray diffraction study of the structure of nanoporous carbon obtained from carbide materials // Fiz. tekh. poluprovodnikov. 2003. Vol. 37. No. 7. Pp. 811–815.
21. *Dzidziguri E.L., Sidorova E.N., Bagdasarova K.A., Zemtsov L.M., Karpacheva G.P.* Formation of Co nanoparticles in metal-carbon composites // Kristallografiya. 2008. Vol. 53. No. 2. Pp. 342–345.
22. *Domonova D.P., Pechenyuka S.I., Semushina Yu.P.* Thermal decomposition of a double Co–Cu salicylate complex in an argon atmosphere to produce metal-carbon compositions // Zh. neorg. khimii. 2022. Vol. 67. No. 4. Pp. 540–544. https://doi.org/10.31857/S0044457X22040043
23. *Fan X., Mashimo T., Huang X. et al.* Magnetic properties of Co–Cu metastable solid solution alloys // Phys. Rev. B. 2004. Vol. 69. P. 094432. https://doi.org/10.1103/PhysRevB.69.094432
24. *Childress J.R., Chien C.L.* Reentrant magnetic behavior in FCC Co–Cu alloys // Phys. Rev. B. 1991. Vol. 43. P. 8089. https://doi.org/10.1103/PhysRevB.43.8089
25. *Jegede O.E., Cochrane R.F., Mullis A.M.* Metastable monotectic phase separation in Co–Cu alloys // J. Mater. Sci. 2018. Vol. 53. No. 16. Pp. 11749–11764. https://doi.org/10.1007/s10853-018-2417-y
26. Diagrams of the state of double metal systems: guide: in 3 vols. / N.P. Lyakishev (ed.). M.: Mashinostroenie, 1996. Vol. 1. 1996. 991 p.
27. *Tuchinskiy L.I.* Composite materials obtained by impregnation. M.: Metallurgiya. 1986. 206 p.

28. *Naydich Yu.V., Kolesnichenko G.A.* Interaction of metal melts with the surface of diamond and graphite. Kiev: Naukova dumka. 1967. 89 p.

29. *Nikonova R.M., Lad'yanov V.V.* Contact interaction of metal melts with fullerite and graphite // J. Mater. Res. Technol. 2020. Vol. 9. No. 6. Pp. 12559–12567. https://doi.org/10.1016/j.jmrt.2020.09.001

30. *Tamai Y., Aratani K.* Experimental study of the relation between contact angle and surface roughness // J. Phys. Chem. 1972. Vol. 76. No. 22. Pp. 3267–3271. https://doi.org/10.1021/j100666a026

31. *Mortimer D.A., Nicholas M.* The wetting of carbon by copper and copper alloys // J. Mater Sci. 1970. Vol. 5. Pp. 149–155. https://doi.org/10.1007/BF00554633

32. *Gulevskii V.A., Antipov V.I., Kolmakov A.G. et al.* Designing of copper-based alloys for the impregnation of carbon-graphite materials // Russ. Metall. (Metally). 2012. No. 3. Pp. 258–261. https://doi.org/10.1134/S0036029512030081

33. *Gulevskii V.A., Antipov V.I., Vinogradov L.V. et al.* Effect of alloying elements on the wetting of graphitized carbon with copper alloys // Russ. Metall. 2019. No. 1. Pp. 72–76. https://doi.org/10.1134/S0036029519010051

34. *Ishida K., Nishizawa T.* The C–Co (Carbon–Cobalt) system // JPE. 1991. Vol. 12. Pp. 417–424. https://doi.org/10.1007/BF02645959

35. *Gluzman L.D., Edel'man I.I.* Laboratory control of coke chemical production. Khar'kov: Gos. Nauchno-tekhn. Izd-vo literatury po chernoy i tsvetnoy metallurgii. 1957. 635 p.

36. *Eremenko V.N., Ivanov M.I., Lukashenko G.M. et al.* Physical chemistry of inorganic materials. Vol. 2. Surface tension and thermodynamics of metal melts. Kiev: Naukova dumka, 1988. 192 p.

37. *Popel' S.I.* Surface phenomena in melts. M.: Metallurgiya, 1994. 432 p.